Imperial College London

QUANTUM PROPERTIES OF PLASMONIC WAVEGUIDES

FREDERIK DIELEMAN

Supervisors:
Prof. Stefan Maier
Prof. Myungshik Kim

Imperial College London
Department of Physics

Thesis submitted in partial fulfilment of the requirements for the degree of Doctor of Philosophy and Diploma of Imperial College London.

January 2017

ABSTRACT

This thesis investigates properties of quantum states of light while travelling as surface plasmon polaritons in plasmonic waveguides and structures. The bosonic nature of SPPs has been shown in previous work by performing a Hong-Ou-Mandel interference experiment with a plasmonic scattering-based beam splitter [1]. Here, we show the same interference with a higher statistical power thanks to an improved set-up. A visibility of 59 ± 1 % is obtained in the two-photon interference, clearly breaking the classical limit of 50 %. The importance of the phase-relations between the different modes in the beam splitter is experimentally probed. The output state of the interference is then further analyzed by a quantum state tomography set-up. This makes it possible to quantify the entanglement generated in the interference. As the interference happens in the plasmonic beam splitter, this shows, to our knowledge for the first time, entanglement generated in a plasmonic structure. Together with the recent results in terms of entanglement and coherence preservation of SPPs [2], this clearly shows the potential of quantum plasmonic devices. To move into the realm of applications, we also investigate theoretically the enhancements in sensitivity quantum states of light can deliver for plasmonic sensing. It is shown that despite the losses, quantum metrology techniques can be useful in an interferometer with plasmonic waveguides [3]. Considering the strengths and successes of plasmonic sensing techniques in a wide range of fields [4], we envision that entangled and squeezed states of light will become a new route to push the limits in sensitivity.

LIST OF PUBLICATIONS

Parts of this thesis have or will appear in the following publications:

Di Martino G., Sonnefraud Y., Tame M. S., Kéna-Cohen S., Dieleman F., Ozdemir K., Kim M. S. and Maier, S. A.. “Observation of quantum interference in the plasmonic Hong-Ou-Mandel effect.” In: Physical Review Applied 1.3 (2014), pp. 1–6. doi: 10.1103/PhysRevApplied.1.034004.

Lee C., Dieleman F., Lee J., Rockstuhl C., Maier S. A., Tame M. S.. “Quantum plasmonic sensing: beyond the shotnoise and diffraction limit.” In: ACS Photonics 3 (2016), pp. 992–999. doi: 10.1021/acsphotonics.6b00082.

Dieleman F., Tame M. S., Sonnefraud Y., Kim M. S., Maier S. A.. "Experimental verification of entanglement generated in a plasmonic system." Submitted.

DECLARATION OF ORIGINALITY

I, Frederik B. C. Dieleman, declare that everything in this thesis is my own original work, unless mentioned differently. In this case appropriate citations will be provided.

COPYRIGHT DECLARATION

'The copyright of this thesis rests with the author and is made available under a Creative Commons Attribution Non-Commercial No Derivatives licence. Researchers are free to copy, distribute or transmit the thesis on the condition that they attribute it, that they do not use it for commercial purposes and that they do not alter, transform or build upon it. For any reuse or redistribution, researchers must make clear to others the licence terms of this work'

Okay, so you're a rocket scientist?
That don't impress me much.
So you got the brain but have you got the touch?

— Shania Twain

ACKNOWLEDGMENTS

Plenty of people to thank, little motivation to add yet another page to this ever-expanding document, so I'll keep it short! Most important are of course my parents and my sister, who always supported me in all my choices, this year and all the years before.

I would like to thank Yannick Sonnefraud who got me into this project and showed me the pleasures of experimental plasmonic research. Mark Tame for the enduring involvement in the project and the theoretical help. My supervisors Stefan Maier and Myungshik Kim for the fruitful discussions and the resources to take on these challenges.

Of course I am also very grateful to have had all these great colleagues and friends and flatmates and people covering several of these categories. People who both helped me on the project and made these years in London an amazing time. In alphabetical order: J. Cambiasso *et al.*.

CONTENTS

INTRODUCTION 1

1 SURFACE PLASMON POLARITONS 5
- 1.1 Metal-dielectric Interfaces 5
  - 1.1.1 Drude model 5
  - 1.1.2 Metal-dielectric interface 6
  - 1.1.3 Thin film 11
- 1.2 Excitation of SPPs 15
  - 1.2.1 Prism coupling 15
  - 1.2.2 Grating coupling 16
  - 1.2.3 Waveguide coupling 21
- 1.3 Waveguides and applications 23

2 QUANTUM OPTICS AND PLASMONICS 26
- 2.1 Quantum Optics 26
  - 2.1.1 Field quantization 26
  - 2.1.2 Optical detection and coherence 30
  - 2.1.3 Quantum interference 33
  - 2.1.4 Density operator 36
  - 2.1.5 Entanglement 38
- 2.2 Quantum Plasmonics 40
  - 2.2.1 Fundamental studies 40
  - 2.2.2 Light-matter interactions 42

3 QUANTUM METROLOGY WITH SPPS 49
- 3.1 Introduction 49
- 3.2 Sensitivity 50
- 3.3 Waveguide structures 53
  - 3.3.1 Dielectric nanowire 53
  - 3.3.2 Silver nanowire 54
  - 3.3.3 Wedge waveguide 55
- 3.4 Quantum Metrology 56
- 3.5 Results 61
- 3.6 Outlook 63

4 QUANTUM INTERFERENCE 66
- 4.1 Sample 66
  - 4.1.1 Fabrication 67
  - 4.1.2 Stripe waveguides 68

4.1.3 Grating couplers 70
4.1.4 Bragg reflectors 72
4.2 Experimental Set-up 76
4.2.1 Spontaneous parametric down-conversion 76
4.2.2 Microscope set-up 80
4.3 Results 82
4.3.1 Photonic result 82
4.3.2 Plasmonic result 83
5 QUANTUM STATE TOMOGRAPHY 87
5.1 Entanglement of Formation 87
5.2 Quantum Tomography set-up 89
5.2.1 Polarization optics 89
5.2.2 Polarization-based Quantum State Tomography 90
5.3 Results 95
5.3.1 Photonic results 95
5.3.2 Plasmonic results 102
CONCLUSION 108

LIST OF FIGURES

Figure 1.1 Schematic depiction of Surface Plasmon Polaritons. 6

Figure 1.2 Wavelength-dependent characteristics of SPPs at flat silver interface. 12

Figure 1.3 Surface Plasmon Polaritons at thin silver film. 14

Figure 1.4 Kretschmann configuration SPP excitation set-up. 16

Figure 1.5 Excitation of SPPs on a metal surface with sinusoidal and rectangular modulations. 18

Figure 1.6 Excitation of SPPs on large rectangular ridges. 20

Figure 1.7 Magnetic field of scattered light from a thin slit in a gold substrate. 21

Figure 1.8 Overview of stripe waveguide, nanoparticle chain and channel waveguide. 25

Figure 2.1 **(a)**, Hanbury Brown and Twiss set-up. **(b)**, Hong-Ou-Mandel experiment. **(c)**, Mach-Zehnder interferometer. **(d)**, Young's double slit experiment. 32

Figure 2.2 The four combinations of two identical photons leaving a balanced beam splitter. 34

Figure 2.3 Plasmonic Hong-Ou-Mandel interference with a scattering-based plasmonic beam splitter [1]. Reprinted with permission from APS Physics. 43

Figure 2.4 Overview of recently published results in quantum plasmonics. 46

Figure 2.5 Overview of two different near-field SPP detection schemes. 48

Figure 3.1 Schematic depiction of a general two-mode interferometer, one arm travels through a nano-waveguide, which transduces the changes of the surrounding refractive index onto the optical mode by a phase shift $\Delta\phi$. 51

Figure 3.2 , Electric field norm $|\mathbf{E}|$ of the only optical mode for a thin dielectric wire (diameter = 100 nm). 54
Figure 3.3 Electric field norm $|E|$ and total transmission in function of the surrounding refractive index for the TM_0 mode of a thin silver nanowire. 55
Figure 3.4 Propagation constant of silver and dielectric nanowire in function of the refractive index of the surrounding medium n_{bio}. 55
Figure 3.5 Electric field norm $|E|$ and total transmission in function of the surrounding refractive index for the TM mode of a silver wedge waveguide. 56
Figure 3.6 Comparison of the quantum and classical metrology approaches for dielectric and plasmonic waveguides, both in the lossless approximation. 59
Figure 3.7 The minimum resolution calculated with the Cramer-Rao bound for the NOON state and the optimal state for calculated transmissivities η ($l = 4\mu m$) for the silver nanowire and wedge waveguide. 62
Figure 3.8 The coefficients $\{x_n\}$ of the optimal states for the silver nanowire and wedge waveguide. 63
Figure 3.9 Schematic depiction of a Mach-Zehnder based phase-sensitive surface plasmon resonance sensor. 65
Figure 4.1 3D sketch and optical picture, taken with set-up depicted in figure 4.2 (a), of a beam splitter sample. 67
Figure 4.2 Measured propagation lengths of the waveguide structures and schemataic drawing of the optical set-up used. 69
Figure 4.3 The top image shows the leaky mode at the gold-air interface, obtained with COMSOL 2D mode solver. Bottom three images are the bound modes at the gold-glass interface. 70
Figure 4.4 Spectra of the light measured at the output grating, with both in- and output grating have a periodicity of 540, 580, 620, 660 or 700 nm. 71

Figure 4.5 Spectrum obtained from illuminating gratings of 540, 580, 620 nm periodicity. The input angle was optimized for the 580 nm grating and has a resonance peak around 800 nm as expected. 72
Figure 4.6 Excitation of the beam splitter structure with laser light with **(a)** TM and **(b)** TE polarization. 74
Figure 4.7 Phase difference between R and T of the plasmonic beam splitter, measured with shown Mach-Zehnder set-up. 76
Figure 4.8 Schematic drawing of the Type I SPDC set-up. 79
Figure 4.9 Spectrum and coincidence measures of the SPDC set-up. 79
Figure 4.10 Schematic drawing of the Hong-Ou-Mandel interferenc experimental set-up. 81
Figure 4.11 Hong-Ou-Mandel interference result on a 50-50 cube beam splitter. 83
Figure 4.12 Mach-Zehnder interference. 84
Figure 4.13 Hong-Ou-Mandel interference at the plasmonic beam splitter. The grey line shows a fit of function 4.13 with the visibility, spectral width and the baseline taken as free parameters. 86
Figure 5.1 Quantum state tomography set-up. 91
Figure 5.2 Schematic drawing of the photonic QST set-up. QWP1, QWP2 and HWP1 are placed in motorized rotators. 97
Figure 5.3 Interference results for the temporal alignment of the QST set-up. 98
Figure 5.4 Photonic quantum state tomography results. 101
Figure 5.5 Schematic drawing of the QST set-up for the plasmonic beam splitter. 103
Figure 5.6 Interference fringes in and stability of the QST set-up with plasmonic beam splitter. 106
Figure 5.7 Results of the quantum state tomography measurements with the plasmonic beam splitter. 107

LIST OF TABLES

Table 1 Splitting ratios of the different structures, normalized by dividing by (R + T) 74

Table 2 The 9 different combinations of abstract angles (θ,ϕ) and experimental angles (α_{QWP1}, α_{QWP2}, α_{HWP}) 93

INTRODUCTION

Richard Feynman described quantum mechanics as "the description of the behaviour of matter and light in all its details and, in particular, of the happenings on an atomic scale" [5]. After the tremendous achievement of providing a consistent description of the behaviour of matter on the atomic scale, the theory started unveiling puzzling implications for the understanding of reality, especially in terms of its non-local nature. Two manifestations of this inherit non-locality of quantum mechanics are central in this work: entanglement and the role of indistinguishability in interference [6]. Schrödinger introduced the term entanglement to describe the possible correlations between two distant particles and called it "*the* characteristic trait of quantum mechanics" [7]. The consequences of these non-local correlations sparked fierce debates on the interpretation of quantum mechanics, most notably led by Einstein [8] and pushed towards experimentally testable assertions by Bell [9]. Feynman on the other hand considered quantum superposition, in the context of Young's famous double slit experiment, the only mystery of quantum mechanics [5]. If an event can be realized in two or more ways, the state of the system is a superposition of each way simultaneously. The interference of the probability amplitudes of these different ways crucially depends on their indistinguishability. This leads to the well known wave-particle duality of light or electrons in the double slit experiment. Even though many fundamental debates are still not settled, the possibility of using quantum effects for technological applications has been realized for a while.

Quantum technology can be defined as the discipline that aims to engineer devices that actively create, manipulate and probe quantum states with the goal of harnessing the distinct quantum effects for practical applications [10]. Quantum computing, cryptography and metrology are prime examples and research has shown steady progress in these fields. The first realizations that quantum devices could perform better than classical ones came at the beginning of the '80s. Feynman pointed out that some problems in quantum mechanics

are exponentially hard to solve on classical computers, but could be done efficiently with a computer that uses quantum states [11]. The theoretical foundations of a universal quantum computer were laid soon after and the field of quantum computation was born [12]. In the same period Caves showed that quantum states of light could be used to obtain remarkable improvements on the sensitivity of interferometers, the start of quantum metrology research [13]. The whole field took off the next decade. Schor showed that quantum computers are capable of efficient prime factorization [14] and the first experimental proof of concepts of both quantum computation [15] and long-range quantum key distribution (QKD) were performed [16].

Optics and quantum optics have had a crucial role in both fundamental research and the progress of quantum technologies. The nonlinear optical effect of parametric down-conversion allows to efficiently generate highly entangled photons, which has been used in most of experimental tests of Bell's inequalities [17, 18]. Furthermore, lasers are ubiquitous to manipulate and read quantum states, or qubits, in many other platforms, such as in ion and atom traps [19, 20]. The idea of using photons as the information carriers, i.e. photonic qubits, became even more popular when Knill *et al.* proposed a universal quantum computation scheme purely based on linear optics and single photons, called linear optical quantum computing (LOQC) [21]. Due to this and other advancements, integrated photonics and nanotechnology started to take a central place in quantum optics research. Many important components needed for LOQC and QKD have already been already been fabricated on platforms like silicon-on-insulator chips [22]. The coupling of quantum emitters, such as quantum dots or vacancy centres in diamond, with nanophotonic structures to control their spontaneous emission has also shown great progress in the past decade [23–26]. This is both interesting for the creation of efficient single-photon sources for the aforementioned applications and for research into light-matter interactions. In this context the potential of using plasmonic nanostructures in quantum optics became clear.

Plasmonics is the research field that studies the coupling of light with the collective oscillations of free electrons in metallic nanostructures, resulting in two distinct effects: surface plasmon polaritons (SPP) and

localized surface plasmon resonances (LSPR) [27]. SPPs are travelling electromagnetic waves confined at a metal-dielectric interface [28]. The confinement at this interface is created by the coupling of the light to the coherent oscillations of the free electron gas relative to the lattice of the ions close to the metal surface [29–31]. These collective excitations or quasi-particles arise from the long-range nature of Coulomb interactions [32]. SPPs are thus hybrid in nature, with both an electromagnetic and electronic component. Even though involving large amounts of electrons the quantum of the electronic component, Plasmon or Surface Plasmon, is also bosonic [32]. Considering the bosonic nature of photons for the electromagnetic component of the excitation, SPPs were thus expected to be bosons, but this was only proven directly recently by performing the seminal Hong-Ou-Mandel interference with SPPs [1, 33–36]. The Hong-Ou-Mandel interference was an interference effect first conducted with two photons and can only be explained in the quantized bosonic description of electromagnetic radiation [37]. The different expected outcome of the interference for two fermionic particles compared to bosonic particles made it a useful tool to probe the nature of SPPs [38]. At higher intensities SPPs can also be described accurately with classical electromagnetism by a combination of Maxwell's equations with a macroscopic model for the dielectric constant ϵ of the metal involved. A damping term in the description of ϵ is used to include microscopic interactions such as electron-electron and electron-photon interactions [28]. Microscopic interactions could still be important though, as they could introduce decoherence in quantum correlations of SPPs. Unlike photons, electronic systems tend to interact strongly with their environment, making them prone to decoherence. The first demonstration of the lack of visible decoherence on a system of two entangled SPPs thus sparked the interest of both the plasmonics and the quantum optics community [39]. Next to the probing of the bosonic nature of SPPs, a range of experiments and applications have been suggested and shown with SPPs at the single quantum level [2]. This thesis will go further in both fundamental research of the quantum behaviour of SPPs and also show a potential application of the merging of quantum optics and plasmonics.

Chapter 1 of this thesis will start by introducing SPPs. The main properties of the confined surface wave will be illustrated in a general

geometry and some specific concepts used later on will be treated in-depth. In the subsequent chapter some fundamental concepts of quantum optics and quantum information theory will be introduced, most importantly quantum interference and entanglement. We will also go through the quantization of SPP modes starting from the macroscopic description of the metal. The research so far conducted in quantum plasmonics is reviewed at the end, showing the wide range of potential applications and advantages plasmonic structures can offer for quantum optics. In chapter 3 new results on the combination of quantum metrology with plasmonic waveguides are presented. We theoretically show the quantum enhancements in sensitivity quantum states of light can deliver for plasmonic sensing devices. The experimental work conducted during this PhD is divided over two chapters. Chapter 4 shows the results obtained on the Hong-Ou-Mandel interference with a plasmonic beam splitter. The work is a continuation of the results presented in the thesis of Giuliana DiMartino [40]. We improved the set-up and gained more understanding in the plasmonic structure, which allowed us to obtain results with a higher statistical power. This allows us to elaborate more on the influence specific characteristics of the structure have on the quality of the measured interference. By combining this set-up with a quantum tomography set-up, we were able to probe the entanglement generated in the interference. This tomography technique and the results are described in chapter 5. The generation of entanglement in a plasmonic structure has not been shown before to our knowledge and can be considered the next step after showing the preservation of entanglement in plasmonic structures.

1

SURFACE PLASMON POLARITONS

Several fundamental properties of SPPs can be shown with the most simple geometries, an extended flat metal surface and thin metal film between two dielectric materials. These will be analysed in the first section 1.1, together with the basic model for the optical behaviour of the free electrons in a metal. This will give some insight in the new research of the later chapters. With only a few calculations with the Maxwell equations, the dependency of SPP behaviour on the shape of the metallic structure and surrounding material can be pointed out. The first allows real sub-wavelength light guiding by proper design of waveguides, both the reason they are interesting for quantum applications as the driving force behind the spur of interest in plasmonics in the past decade. The strong influence of the (refractive index of the) surrounding medium on the SPP wave-vector gives a fundamental argument for plasmonic sensing applications, including our quantum metrology research in chapter 3. Section 1.2 introduces the most used ways of exciting SPPs, an important roadblock in many plamsonic experiments. This is also the case for our experimental work in chapter 4 and chapter 5, for which we designed and tested excitation gratings. The basic theory behind this technique is explained in-depth here. In section 1.3 an overview of some often used and promising waveguide structures and applications will be given.

1.1 METAL-DIELECTRIC INTERFACES

1.1.1 *Drude model*

The interaction of the electromagnetic field at optical and near-infrared frequencies with metallic structures is mainly defined by the free electrons of the metal. These electrons oscillate approximately 180° out of phase of the driving optical fields, resulting in a negative dielectric constant. The Drude model describes the free electrons as a plasma -a gas of charged particles- against the background of positive ion cores.

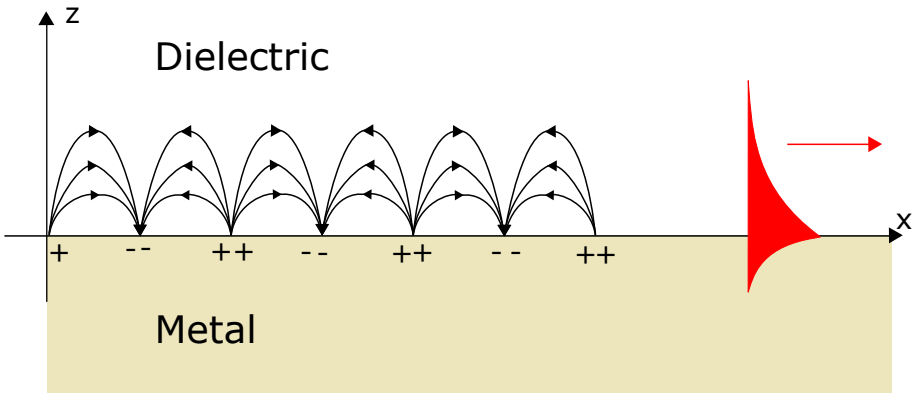


Figure 1.1: Schematic depiction of Surface Plasmon Polaritons on a metal-dielectric interface.

This results in the following dielectric constant as a function of the radial frequency ω [28, 41]:

$$\epsilon(\omega) = 1 - \frac{\omega_p^2}{\omega^2 + i\gamma\omega}, \tag{1.1}$$

with ω_p the plasma frequency and γ the collision frequency, which is a damping term. Both are material-dependent parameters and have been measured for a range of (noble) metals [42]. Gold and silver are most frequently used metals in plasmonics, their high plasma frequency ($\omega_{p,silver} = 1.37 \times 10^{16}$ rad/s and $\omega_{p,gold} = 1.37 \times 10^{16}$ rad/s) and relatively low collision frequency ($\gamma_{silver} = 2.73 \times 10^{13}$ rad/s and $\gamma_{gold} = 4.05 \times 10^{13}$ rad/s) create desirable optical properties in terms of the real and imaginary part of $\epsilon(\omega)$. Interband transitions of the bound electrons of the material can limit the accuracy of the Drude model at the higher frequency end of the optical spectrum, for gold the imaginary part of $\epsilon(\omega)$ starts to become considerably bigger at wavelengths below 600 nm, while silver remains accurately described by the model up to a wavelength of 400 nm [28, 41]. For this reason we will use silver in the following derivations.

1.1.2 *Metal-dielectric interface*

SPPs are the result of the coupling of the electromagnetic field with plasmons, the quanta of the plasma oscillations of the free electrons in the metal. Their existence as confined electromagnetic surface waves can be shown purely with Maxwell's equations and the appropriate material parameters ($\epsilon(\omega)$) and boundary conditions. This is most

easily done for an infinite interface between two materials, as depicted in figure 1.1. During the derivation we will see the necessary condition for two materials of having opposite signs of the real part of the dielectric constant. This explains the use of metals at optical frequencies. The wave equations for the electric and magnetic field of a travelling electromagnetic wave,

$$\nabla^2\mathbf{E} - \frac{\epsilon}{c^2}\frac{\partial^2\mathbf{E}}{\partial t^2} = 0 \tag{1.2}$$

$$\nabla^2\mathbf{H} - \frac{\epsilon}{c^2}\frac{\partial^2\mathbf{H}}{\partial t^2} = 0 \tag{1.3}$$

are valid as long as the material profile varies more slowly than the wavelength of the wave. The relative magnetic permeability is set to 1, both silver and gold are up to a very good approximation non-magnetic. These equations can be applied in the two separate areas, with $\epsilon_m(\omega)$ for $z < 0$ and ϵ_d for $z > 0$, after which both solutions will be connected by the boundary conditions imposed by the interface. First they are transformed to the Helmholtz equation by using the harmonic time dependence of the wave ($\mathbf{E}(\mathbf{r}, t) = \mathbf{E}(\mathbf{r})e^{-i\omega t}$):

$$\nabla^2\mathbf{E} + k_0^2\epsilon\mathbf{E} = 0, \tag{1.4}$$

with k_0 the wave vector of the wave in vacuum and the same transformation for the wave equation of the magnetic field. As in figure 1.1, we assume propagation in the x-direction and uniformity in the y-direction, so the Helmholtz equations become:

$$\frac{\partial^2\mathbf{E}(z)}{\partial z^2} + (k_0^2\epsilon - k^2)\mathbf{E} = 0 \tag{1.5}$$

$$\frac{\partial^2\mathbf{H}(z)}{\partial z^2} + (k_0^2\epsilon - k^2)\mathbf{H} = 0, \tag{1.6}$$

To find the field profiles of all the components of the wave, we need to use Maxwell's curl equations: $\nabla \times \mathbf{E} = -\mu_0\frac{\partial\mathbf{H}}{\partial t}$ and $\nabla \times \mathbf{H} = \frac{\partial\mathbf{D}}{\partial t}$. Harmonic time dependence ($\frac{\partial}{\partial t} = -i\omega$), propagation along x-direction ($\frac{\partial}{\partial x} = ik$) and invariance in the y-direction ($\frac{\partial}{\partial y} = 0$) are still assumed, resulting in two uncoupled sets of equations. The transverse magnetic (TM) equations:

$$E_x = -i\frac{1}{\omega\epsilon_0\epsilon}\frac{\partial H_y}{\partial z},$$

$$E_z = -\frac{k}{\omega\epsilon_0\epsilon}H_y, \tag{1.7}$$

$$\frac{\partial^2 H_y}{\partial z^2} + (k_0^2\epsilon - k^2)H_y = 0, \tag{1.8}$$

where the last equation is the wave equation. In similar fashion the transverse electric (TE) equations are given by

$$H_x = i\frac{1}{\omega\mu_0}\frac{\partial E_y}{\partial z},$$
$$H_z = \frac{k}{\omega\mu_0}E_y, \tag{1.9}$$
$$\frac{\partial^2 E_y}{\partial z^2} + (k_0^2\epsilon - k^2)E_y = 0. \tag{1.10}$$

We start by analysing the TE equations. Considering the two different media for $z < 0$ and $z > 0$, we can construct solutions for the wave-equation for both half-spaces: $E_y(z) = A_m e^{ikx}e^{k_m z}$ and $E_y(z) = A_d e^{ikx}e^{-k_d z}$ for $z < 0$ and $z > 0$ respectively. The boundary conditions for the magnetic ($(\mathbf{B}_m - \mathbf{B}_d).\mathbf{n} = 0$) and electric displacement field ($(\mathbf{D}_m - \mathbf{D}_d).\mathbf{n} = \rho_{surface} = 0$) impose continuity of E_y and H_x at the interface. This means that $A_m = A_d$ and $A_m k_m = A_d k_d$. The only confined solution ($Re[k_m] > 0$ and $Re[k_d] > 0$) for these two equations is $A_m = A_d = 0$, there are thus no confined transverse electric surface waves at a metal-dielectric interface.

With the same approach we can construct a general solution for the TM wave-equation for both half-spaces: $H_y(z) = A_m e^{ikx}e^{k_m z}$ and $H_y(z) = A_d e^{ikx}e^{-k_d z}$ for $z < 0$ and $z > 0$ respectively. The same boundary conditions on the magnetic field and electric displacement field now impose continuity for H_y and $\epsilon_i E_z$, so $A_m = A_d$ and:

$$\frac{k_d}{k_m} = -\frac{\epsilon_d}{\epsilon_m}. \tag{1.11}$$

This is solvable with both $Re[k_m] > 0$ and $Re[k_d] > 0$ thanks to the negative real part of the dielectric permittivity of the metal. From the wave equation, k_m and k_d can be written as a function of the wave vector of the surface wave k and k_0:

$$k_m^2 = k^2 - k_0^2\epsilon_m, \tag{1.12}$$
$$k_d^2 = k^2 - k_0^2\epsilon_d. \tag{1.13}$$

Together with equation 1.11, this delivers the dispersion relation of the surface waves, SPPs, at the interface between a dielectric with permittivity ϵ_d and a metal with permittivity $\epsilon_m(\omega)$:

$$k = k_0\sqrt{\frac{\epsilon_m\epsilon_d}{\epsilon_m + \epsilon_d}}. \tag{1.14}$$

Putting equation 1.1 for ϵ_m in this dispersion relation gives some interesting first insights. First of all, ϵ_m is complex, consequently k will also have a real and imaginary part: $k = \beta + i\alpha$. The real part of k, β, is the propagation constant, while the imaginary part, α, defines the propagation loss. The real part of the dispersion curve is shown in figure 1.2 (a) for a silver-air interface with $\omega_p = 13.7 \times 10^{15} rad/s$ and thus $\epsilon_d = 1$. The SPP-line starts to deviate strongly from the light line in a vacuum and β goes to infinity for $\omega \to \frac{\omega_p}{1+\epsilon_d}$. The SPP becomes less and less light-like and more confined at the surface, the group velocity also slows down and eventually goes to 0, the mode becomes electrostatic. This extreme situation does not happen with realistic metals, due to the aforementioned breakdown of the Drude model, the SPP curve turns around at a maximum propagation constant (for vacuum-silver around 3×10^7) and continuously evolves into the higher energy branch. This branch is called the Brewster mode and represents radiation in the metal instead of surface waves, which is thus of little importance for this thesis. Although at wavelengths around 800 nm, the region we are interested in in this thesis, the propagation constant of the SPP at a vacuum-silver or vacuum-gold interface lies close to the light-line, it will always be to the right of it. This means a SPP has a higher momentum than the free space photon with the same frequency, and to excite SPPs phase-matching techniques are necessary, as explained in the next section.

From differential equations 1.7, the electric fields in the dielectric are given by:

$$\begin{aligned} E_x(z) &= \frac{ik_d}{\omega\epsilon_0\epsilon_d} k_d e^{ikx} e^{-k_d z}, \\ E_z(z) &= \frac{-k}{\omega\epsilon_0\epsilon_d} e^{ikx} e^{-k_d z}., \end{aligned} \tag{1.15}$$

and in the metal by:

$$\begin{aligned} E_x(z) &= \frac{-ik_m}{\omega\epsilon_0\epsilon_m} k_d e^{ikx} e^{k_m z}, \\ E_z(z) &= \frac{-k}{\omega\epsilon_0\epsilon_m} e^{ikx} e^{k_m z}. \end{aligned} \tag{1.16}$$

Equations 1.15 show that the transverse electric field in the dielectric is considerably bigger than the longitudinal field at lower energies as $k >> k_d$, the mode can not exist without the longitudinal component, but SPPs are by approximation TEM modes. It is interesting to

check how confined SPPs are: from equations 1.15 and 1.16 one can see that the decay length of the fields into the dielectric and metal are given by $z_d = \frac{1}{Re[k_d]}$ and $z_m = \frac{1}{Re[k_m]}$ respectively. These can be calculated with equations 1.12 and 1.13, which is done over a free-space wavelength λ_0 range of 400 ($\beta = 1.7 \times 10^7 m^{-1}$) to 1500 nm ($\beta = 4.2 \times 10^6 m^{-1}$) in figure 1.2 (b). While the penetration into the metal stays quite constant around 22 nm over the whole range, the confinement at the dielectric side is highly wavelength dependent and becomes sub-wavelength only at the very short wavelengths. To obtain real sub-wavelength confinement more complicated waveguide structures than a flat interface have to be used, like stripe, wedge and nanowire waveguides presented later in this thesis. These not only provide confinement in the lateral dimension, the electromagnetic wave is also more densely squeezed towards the metal surface.

With the full description of the field profiles of the SPPs, it is also possible to calculate how much of the electromagnetic energy is localized in the metal. The energy density in in the metal can be approximated by $u_m = \frac{\epsilon_0}{4}\left(Re[\epsilon_m(\omega)] + \frac{2\omega Im[\epsilon_m(\omega)]}{\gamma}\right)|\mathbf{E}|^2$, while the density in the dielectric is given by $u_d = \frac{1}{2}\left[\epsilon_0\epsilon_d|\mathbf{E}|^2 + \mu_0|\mathbf{H}|^2\right]$ [28]. By plugging in the field components and integrating over z, we can calculate the fraction of the total energy U that is localized in the metal, shown as a function of the wavelength in figure 1.2 (c). At 1500 nm, only a very small fraction, 0.5 % is located in the metal, at 400 nm it is around 3 %, this is not unexpected as at 1500 nm the propagation constant only deviates 0.5 % for the light line, at 400 nm already 7.5 %. The influence of ohmic losses thus strongly increases at lower wavelengths, which influences the propagation length of the SPPs, the length over which the intensity of the mode falls down to a factor $\frac{1}{e}$ of the original intensity, given by

$$L_{prop} = \frac{1}{2Im[k(\omega)]} = \frac{1}{2\alpha(\omega)}. \tag{1.17}$$

With the theoretical values of $\epsilon_m(\omega)$ the propagation length is over 1 mm at $\lambda_0 = 1500$ nm, while at 400 nm it has decreased to a mere 58 μm. At 800 nm it is still 330 μm, but we will see in later chapters that the higher confinement offered by waveguide structures comes with a strong increase in propagation loss. It has to be noted that the propagation length also strongly depends on the deposition techniques of the metallic surface, ohmic loss is not the only loss factor, surface

smoothness and grain boundaries have a considerable influence and can be optimized with the right techniques [43]. Even on this seemingly established and fundamental level, progress is still being made for plasmonics applications.

The fact that most of the energy of SPPs is located outside of the guiding medium (the metal) is one of the crucial advantages of SPP waveguides. It allows to tailor the optical behaviour by choosing the surrounding medium, for example with nonlinear dielectrics for active devices. This is considerably less efficient in fibre optics and silicon photonics, often resulting in the need of long interaction lengths to obtain the same effect [44]. This also makes plasmonics a popular platform for sensing applications, the wave vector of SPPs is highly dependent on the surrounding material. Figure 1.2 (d) shows that for an increasing value of the refractive index of the dielectric, an increasing fraction of the light is pushed into the metal, the optical mode becomes smaller. The result on the propagation constant and length is shown in 1.2 (e), SPPs are more sensitive to the refractive index than free-space photons, in clear contrast to most dielectric waveguides. The propagation length, as expected and generally undesirably, also drops strongly with increasing n_d, as shown in figure 1.2 (e). The high confinement of SPPs also means that the sensitivity to the surrounding material is highly local, allowing to design sensing applications with a high spatial resolution [4].

1.1.3 *Thin film*

It is interesting to look at the first step towards more complicated structures than a single interface, a thin film of metal surrounded by two dielectric materials. Some new concepts arise from this structure that help to understand waveguides, like the wedge waveguide in chapter 3 and the stripe waveguide in chapter 4. The solutions to this problem are obtained in the same way as the single interface, by imposing the right boundary conditions on general solutions of the wave and curl equations in the respective regions. Due to the larger set of linear coupled equations, more physically distinct solutions arise, depicted in figure 1.3 (a). Based on the behaviour of the transverse electric field in the metal, the solutions can be classified in anti-symmetric modes, where the transverse electric field goes to

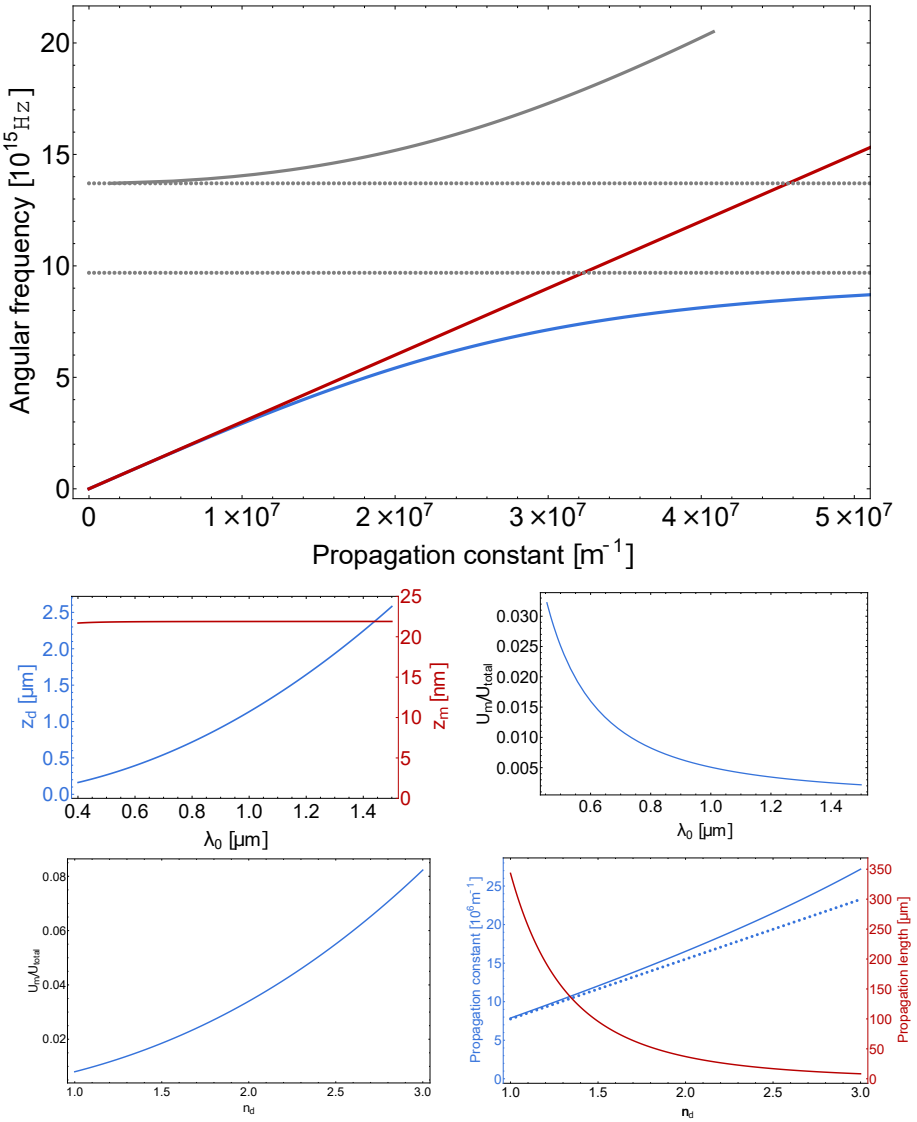


Figure 1.2: **(a)**, Dispersion curve for SPPs at silver-air interface, $\epsilon_m(\omega)$ taken from the Drude model, $\omega_p = 1.37 \times 10^{16}$ rad/s. Red line is the light line ($\omega = kc$), dotted grey lines at ω_p and $\omega_p/\sqrt{2}$. **(b)**, Decay length into the dielectric (z_d) and metal (z_m) as a function of the free-space wavelength λ_0. **(c)**, Fraction of the energy of the mode localized in the metal, as a function of λ_0 . **(d)**, Fraction of the energy of the mode localized in the metal, as a function of n_d. **(e)**, Propagation constant and propagation length as a function of n_d. Blue dotted line is the propagation constant for the free-space light.

zero in the metal, and symmetric modes, where it does not. Depending on the material parameters, both of these types can exist as bound modes and/or leaky modes. Bound modes are modes where the SPP is spatially confined at both interfaces, where for leaky modes the SPP is bounded at one of the two interfaces, but radiates into free space at the other side of the metal film. Leaky modes are important in the asymmetric geometry $n_1 \neq n_3$, where the symmetric mode is positioned at the lowest refractive index side and radiates into the higher index material. Inversely, it allows to couple from free space to this mode through the high refractive index material, the basis for the Kretschmann configuration to excite SPPs. Except for the radiation loss, this mode largely has the same properties as SPPs at the single interface. Crucial parameters for the existence and behaviour of the 4 different modes are the thickness of the film and the values of n_1 and n_3 relative to each other; excellent overviews are given by Burke *et al.* [45] and Prade *et al.* [46].

For the symmetric case $n_1 = n_2$ with a lossless metal, only the bound modes exist, dispersion curves are shown in figure 1.3 (b) for thicknesses of 40 and 80 nm and $n_i = 1$. The symmetric and asymmetric mode clearly decouple strongly when the film becomes comparable to the penetration depth of the single-interface SPP. For the limiting case of a very thick film, the two modes become degenerate, they are just single-interface SPPs at both sides of the film. Compared to the single-interface dispersion curve, the symmetric curve lays closer to the light-line, the mode is more light-like. The thinner the film, the more the mode penetrates into the dielectrics and it becomes a regular plane wave for $h \to 0$. Very long propagation lengths are possible with thin films due to this, making them often referred to as long-range SPPs. The asymmetric mode on the other hand, becomes more confined for thinner films, resulting in a propagation constant that strongly deviates from k_0 (shown in figure 1.3 (c)) and a small mode volume, but also (very) short propagation lengths. This clearly shows the strong influence the geometric parameters have on the optical behaviour, useful to tailor modes.

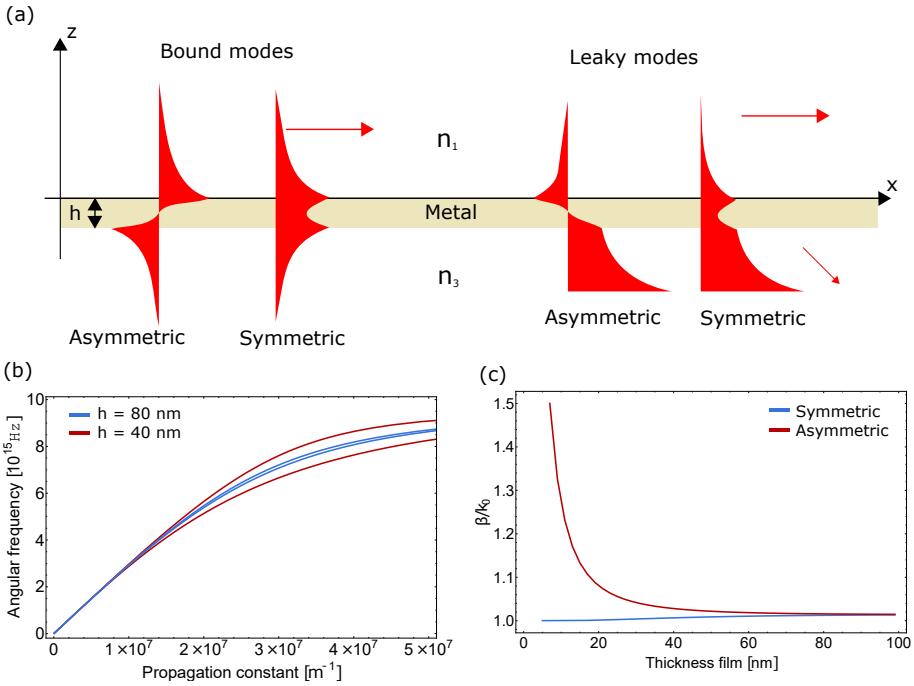


Figure 1.3: **(a)**, Thin film geometry with depiction of the transverse electric fields of the different modes. **(b)**, Dispersion curve of the bound modes for a theoretical lossless silver film of 40 and 80 nm. **(c)**, Dependence of the propagation constant on the silver film thickness for the symmetric and asymmetric mode.

1.2 EXCITATION OF SPPS

In the corpuscular description of radiation, the momentum of a SPP is larger than that of a free-space photon of the same frequency: $\hbar\beta > \hbar k_0$ [47], following the relation between β and k_0 shown in the previous section. Considering all the momentum of SPPs is in-plane along the flat metal-dielectric interface, it explains why SPPs are confined at the surface, the in-plane momentum of the SPPs will always be bigger than the momentum of the photon radiated into the dielectric, regardless of the angle it radiates away from the surface with; $k_{0,x} = \sin(\theta)k_0$ will always be smaller than $\beta_x = \beta$. It also means that it is not possible to couple photons to the SPP-mode by just shining light on the surface, regardless of the angle it impinges it with. Several techniques have been developed to alleviate this problem. Excitation by the electromagnetic field of high-energy electrons travelling through the metal surface is a possibility, but most techniques involve the direct coupling of photons to SPPs by matching their momentum [28]. Prism coupling, grating coupling and waveguide coupling will be discussed here. Grating coupling is the technique used in our experimental work in the last chapters, prism coupling is important in plasmonic sensing and the progress in research of efficient coupling between dielectric waveguides and plasmonic modes is exciting for the potential merging of integrated (quantum-)photonics with plasmonics.

1.2.1 *Prism coupling*

A first possible solution is the use of a three-layer system, as shown in figure 1.4. The metal film is sandwiched between two dielectrics with different dielectric constants, so $n_{sub} > n_{sup}$. The symmetric leaky mode, that is mainly positioned at the superstrate-metal interface, has a propagation constant that is smaller than the wave vector of the free space photons in the substrate: $\beta_{sym,leaky} < k_0 n_{sub}$, resulting in radiation leakage. By impinging the metal with the right angle θ, the in-plane part of the wave vector $k_x = k_0 n_{sub} \sin(\theta)$ can thus match β. This method of exciting SPPs is called the Kretschmann configuration and typically achieved by evaporating the thin layer of metal on the prism face. Another method is the Otto configuration in which a prism, without metal layer, is brought close to the metal sur-

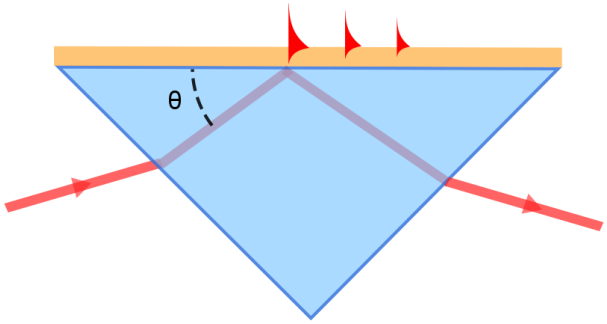


Figure 1.4: Kretschmann configuration SPP excitation set-up.

face in a controllable fashion, the evanescent waves created by total internal reflection at the prism-air interface have an in plane momentum high enough to excite SPPs at the metal-air interface. Due to the need of accurate control of the prism-metal distance with the Otto technique, the Kretschmann configuration is preferred for most applications. The excitation of SPPs can be monitored by measuring the reflected light, efficient excitation means high losses due to SPP propagation and low reflected intensity. As we've seen before, the propagation constant of SPPs depends strongly on the refractive index of the dielectric at the surface. In these set-ups, the excitation angle can thus with high sensitivity be related to the refractive index , which is the idea behind the well-established Surface Plasmon Resonance sensors. Different approaches have been developed, monochromatic light with a range of excitation angles (by a non-collimated source) can be used, where the angle with the lowest reflectivity is related to the refractive index. Another approach uses collimated light with a wide spectrum, the excitation wavelength can then be used to calculate the refractive index [4].

1.2.2 *Grating coupling*

Prism coupling is well-established and easy to use for many applications, but excites over large areas - depending on the laser spot size - and is thus not really suitable for integrated plasmonics. Grating couplers are a potential solution for this, as the structures can be fabricated highly locally with techniques like Electron Beam Lithography and tailored for specific waveguide structures. The diffraction equation for a grating, which calculates at which angles constructive interference from the scattered plane waves results in the diffraction

peaks, can be expressed in terms of the in-plane momentum of the incoming light and of the scattered light of the diffraction peaks: $k_{s,x} = k_{i,x} + m\frac{2\pi}{L}$, with L the period of the grating and m the diffraction order, so $m \in \mathbb{Z}$ [48]. To use a diffraction peak to excite SPPs, the in-plane momentum of the diffracted photons has to match the momentum of the SPPs on the surface [49]:

$$k_{SPP} = \pm k_0 \sin(\theta) \pm m\frac{2\pi}{L}. \tag{1.18}$$

The easiest case to analyse is for small sinusoidal modulations of the surface, shown in figure 1.5 (a), as only the first order diffraction will have a meaningful efficiency. Barnes *et al.* [49, 50] made an in-depth study of these metal gratings by calculating the total reflectivity as a function of the angle and wavelength of the incident light, a result is shown in figure 1.5 (c). At a fixed angle of incidence, there are two wavelengths of the incoming light that excite SPPs, the shortest wavelength creates forward scattering of SPPs, while the longer wavelength creates backwards scattering, both relative to the direction of the incoming light. At normal incidence these two energies become degenerate, the branches in (c) cross and both directions are excited at the frequency of the light for which the wavelength of the SPPs matches the period of the grating.

Different shapes, like square ridges shown in (b), can be considered as the summation of many sinusoidal gratings due to the Fourier components. When taking into account only the first two Fourier components of a random (small) modulation, the surface can be expressed as:

$$s(x) = d_1 \sin(Kx) + d_2 \sin(2Kx + \phi_2), \tag{1.19}$$

with d_1 and d_2 the modulation depth of the two components and ϕ_2 the relative phase between the two. The reflection of this surface with d_1 = 5 nm, d_2 = 2 nm and $\phi_2 = 0^o$ is shown in figure 1.5 (d). An important difference is the appearance of an energy gap at normal incidence, the two branches do not become degenerate. The added 2K component provides an interaction between the forward and backwards travelling SPP modes, resulting in 2 standing waves with different energies, which creates a bandgap between these energies. This is similar to the photonic band gap behaviour of a quarter wave dielectric stack. This effect is used to create a (semi-transparent)

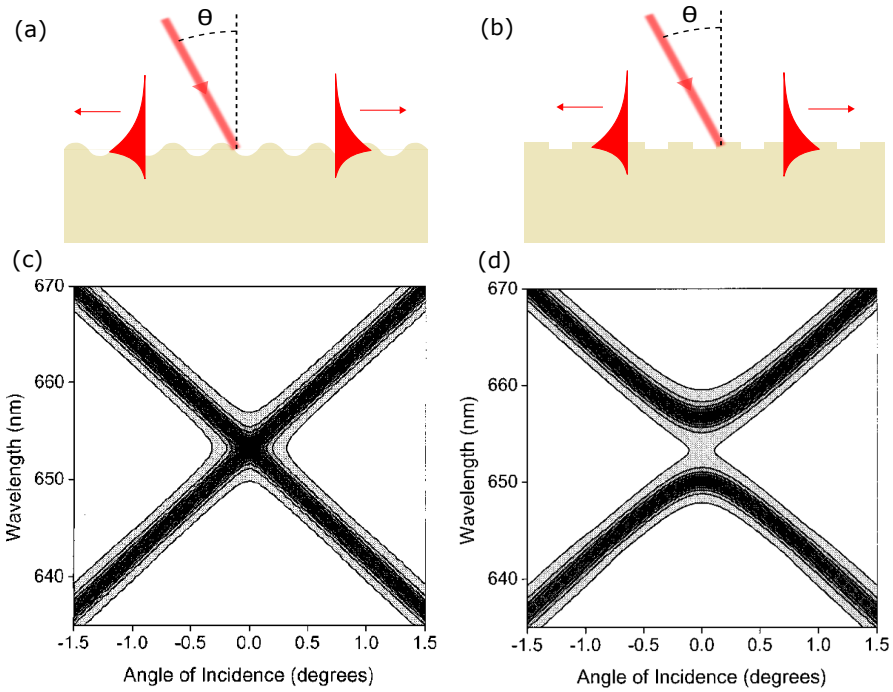


Figure 1.5: Excitation of SPPs on a metal surface with sinusoidal modulations in **(a)** and rectangular ridges in **(b)**. Numerically modelled total reflectivity of a silver surface with small sinusoidal modulations as a function of the angle of incidence and the wavelength of the illuminating plane waves, with grating pitch 634 nm, amplitude $d_1 = 5$ nm. **(d)**, Same as (c), but with and extra modulation component with $d_1 = 2$ nm and $\phi_2 = 0^o$. Images (c) and (d) are taken from Barnes *et al.* [49], reprinted with permission from APS Physics.

Bragg reflector in chapter 4. The importance for grating coupling is the fact that k_{SPP} is not just the wave vector of the SPPs on a metal-dielectric interface. For the parameters we will use for our rectangular ridges in chapter 4, this deviation turns out to be large, and even for normal incidence the incident wavelength does not lie close to the period of the optimal grating, as one would expect from the first order approximation.

Although the set-up of plane waves illuminating an infinite grating with small modulations shows both the possibility of grating coupling and the influence gratings have on the dispersion curve of the travelling SPPs, experimentally used gratings have strongly different geometric parameters. The excitation needs to be local, so the grating often only consists of a small amount of periods, typically ten or

less, and the excitation beam is generally, also in our experiments, a Gaussian beam focused down with a microscope objective. For this limited amount of elements, it was shown that bigger modulations of the surface resulted in more efficient excitation [51]. With rectangular gold ridges of 60 nm high and 200 nm wide on a gold film, Ditlbacher *et al.* showed experimentally the importance of the period of the grating, even with only 3 ridges the excitation efficiency was drastically improved when the period matched the the expected wavelength of the SPPs for the used excitation wavelength [51]. This clearly points towards constructive interference from the SPPs excited by scattering on the seperate ridges. Optimizing the scattering properties of a single ridge or indentation and then optimizing the grating parameters is an approach that was followed by several groups. A single subwavelength ridge on the surface can be approximated as a Rayleigh dipole scatterer [52], considering the squared dependence of the scattered efficiency to the volume of the scatterer [53], it indeed seems a good idea to create large modulations of the surface, so moving away from the first order investigations of Barnes *et al.* [49]. The excitation of SPPs on a gold metal film with a finite grating of rectangular ridges was experimentally studied in the near-infrared by Radko *et al.*, corroborated by numerical simulations [52]. The experimental measurements of excitation efficiency were performed by collecting the radiation of the leaky mode into the substrate. Simulations to find the optimal ridge width and height for an excitation wavelength of 800 nm are shown in 1.6 (a), high ridges are clearly favoured and ideal widths are close to half the wavelength. The same conclusion was made by Leveque *et al.*, who showed that the ridge width is ideally around half the grating period [54]. Experimentally measured excitation efficiencies are shown in figure 1.6 (b) as a function of the number of ridges, illuminated with a 5 µm wide Gaussian beam. When the wavelength is correctly tuned for the grating period of 800 nm, adding more ridges clearly helps the efficiency, even though 10-15 ridges cover an area larger than the incoming spot. Interestingly, they still found a resonant wavelength very close to the 800 nm period of the grating, unlike our experimental results shown in chapter 4. This seems to indicate that while 50 nm high ridges do not influence the dispersion curve of the SPPs considerably , heights of 90 nm do create a strong deviation of the SPP wavelength from the wavelength on a flat surface.

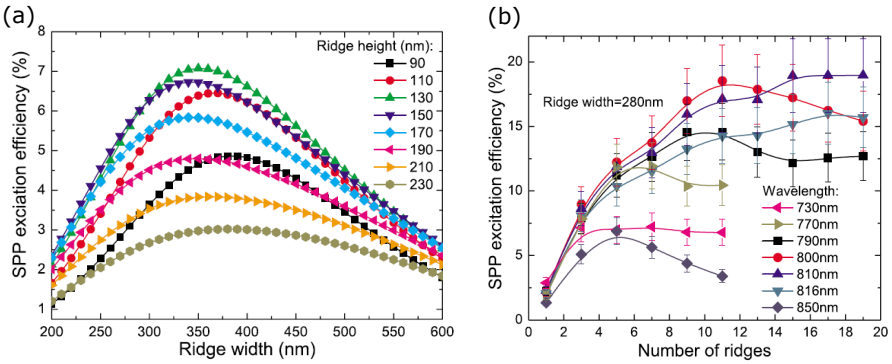


Figure 1.6: **(a)**, Numerical predictions of the excitation efficiency of one ridge with a 800 nm laser as a function of the ridge width and height. **(b)**, Experimentally measured efficiencies for gratings with a period of 800 nm, ridge height of 50 and width of 280 nm. Both pictures taken from Radko *et al.* [52], reprinted with permission from APS Physics.

Recent research showed that single scatterers like a ridge or groove on a metal surface create hybrid waves of SPPs and quasi-cylindrical waves (CWs) [55–57]. An example of these hybrid waves obtained by full-vectorial simulations is shown in figure 1.7, taken from Lalanne *et al.* [55]. The magnetic fields on the right-hand side clearly show that the total field can be decomposed in SPPs and CWs. Fortunately at the metal surface, the field of the CW rapidly decays. At a distance of several wavelengths the total wave mainly consists of SPPs, which is important for our experimental work. The CWs are expected to influence the working of the grating, the ones generated at one ride or groove can scatter into SPPs on the next and attribute to the total behaviour of the grating. It is clear that the problem of a finite-sized grating with large modulations of the surface is complicated and necessitates experimental measurements or complete numerical simulations to optimize the parameters used. In section 4.1.3 spectral measurements on fabricated gratings with 11 ridges with a range of periods are shown and used to chose the best choice for the quantum interference experiments. The parameter range was decided on the basis of basic numerical simulations and results reported in the publications mentioned here, more information can also be found in the thesis by Giuliana DiMartino [40].

More complex grating structures have been proposed and fabricated

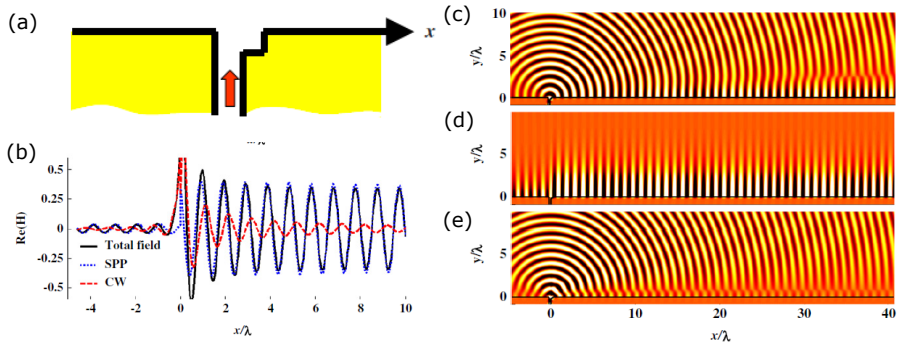


Figure 1.7: **(a)**, Slit in gold substrate with width = 200 nm, second indentation is square with of a 150 nm, creating a asymmetric scattering pattern of the incoming light with $\lambda_0 = 800$ nm. **(b)**, Real part of the scattered magnetic field on the surface, subdivided in SPP and CW contribution. **(c)**, Total magnetic field scattered in air. **(d)**, Magnetic field from the SPP component. **(e)**, Difference between total and SPP magnetic field, the contribution of the quasi-cylindrical wave. All images taken from Lalanne *et al.* [55], reprinted with permission from Elsevier.

in recent years. Baron *et al.* showed that it was possible to efficiently excite SPPs unidirectionally on a gold film with normal incidence of the exciting laser beam by optimizing the width and depth of each the 11 sub-wavelength grooves separately [58]. By illumination with a Gaussian beam, this structure with a total size of less than 8 µm excited SPPs with an absolute efficiency of more than 50 % and the extinction ratio between the two directions perpendicular to the grating was 47. Similar results have been shown for a different grating structure [59] and expanded towards the control of the direction of excitation by the polarization of the incoming light, done by creating a 2-dimensional grating of rectangular scatterers [60, 61]. To improve the potential applications of these plasmonic structures in quantum technologies, even higher efficiencies and the combination with (highly confined) waveguides should be achieved.

1.2.3 *Waveguide coupling*

The direct coupling from a dielectric waveguide to a plasmonic one is a highly promising approach to excite SPPs. It allows the integration of plasmonic structures with other versatile dielectric platforms, where propagation losses are a less stringent parameter. One could

easily imagine the use of plasmonic waveguides for short lengths, when there is a need for high light-matter interaction e.g., after which the light is coupled back to dielectric structures to minimize propagation losses [62]. The efficiency of the coupling depends on the overlap between the dielectric and the plasmonic mode, which immediately creates the biggest challenge: overcoming the typical size-mismatch between the two [63]. Experimental progress has been achieved in the past decade, mainly with silicon waveguides; the high refractive index of silicon provides small mode volumes for dielectric standards and silicon is a highly popular platform for integrated photonics on itself. Chen *et al.* showed that covering a tapered area of a silicon-on-silica rectangular waveguide with gold creates a highly confined waveguide at telecom wavelengths. The coupling between the dielectric mode in the silicon waveguide and the plasmonic mode in the gold-covered area can in principle be made highly efficient with the right tapering length, up to almost 90 % theoretically, experimentally values of 55 % were reached [64]. More efficient coupling, with experimental values up to 80 %, has been reported between silicon waveguides and dielectric-loaded plasmonic waveguides made of PMMA [65]. Dielectric-loaded plasmonic waveguides are structures where SPPs vertically confined to a metal surface are laterally confined with the help of a dielectric rectangular waveguide. The confinement of the light inside the silicon or a fixed dielectric of course limits the use of the waveguide for sensing or active plasmonics applications. Tian *et al.* followed an altered approach, where a tapered ending of a silicon waveguide was coupled into a plasmonic gap waveguide [66]. Theoretical calculations of 88 % and an experimental demonstration of 35 % shows that it is possible to efficiently couple light into a metal-air plasmonic waveguide with high confinement. This approach has recently been improved by Ono *et al.*, who managed to couple light from the silicon waveguide into a gap waveguide with a mode volume of only 50 by 20 nm with an efficiency of over 65 % [67]. Slightly less efficient coupling, but still highly promising due to the popularity of groove waveguides, has also been shown for a silicon waveguide to a gold groove waveguide, with experimental coupling efficiencies of around 22 % [68]. All these works have been performed at telecom wavelengths and next to bridging the gap between theoretical and experimental coupling efficiencies, finding similarly efficient

SPP excitation structures in the visible range is thus an outstanding challenge.

1.3 WAVEGUIDES AND APPLICATIONS

With the first observation of SPPs at the start of the previous century [69] -although unknowingly-, the introduction of the concept of Plasmons in 1956 [70] and the term Surface Plasmon Polariton [71] in 1974, SPPs already have a long history in fundamental research [72]. First potential applications were realized for sensing and this created a strong growth in the field of plasmonics. Fleischmann *et al.* noticed the substantial influence the vicinity of a rough metal surface has on Raman spectra of molecules [73], with intensity enhancements up to 10^5. After the link with plasmon resonances on the metal surface roughnesses was established [74], the engineering of specific structures started, ultimately leading to single molecule sensitivity 20 years ago [75]. The technique of Surface Enhanced Raman Spectroscopy (SERS) has since then continued to expand, with new capabilities and applications in a range (bio-)chemistry research. Around the same time the currently most used commercially available plasmonic application was invented and developed: the Surface Plasmon Resonance sensor (SPR) [4, 76]. Liedberg *et al.* realized that the sensitivity of the excitation angle of SPPs in Kretschmann-like configurations on the refractive index at the opposite side of the metallic film could be used to sense gas concentrations in 1983 [77].

A second wave of increased research in SPPs came with new fabrication techniques and the full realization of the possibilities of sub-diffraction waveguiding. In 1997, Takahara *et al.* showed theoretically that silver nanowires could be used to guide light in an optical mode that is strongly sub-wavelength in all dimensions, unlike SPPs along single interfaces or metal films [78]. At the same time, the concept of nano-focusing with tapered plasmonic waveguides was proposed; Nerkararyan showed that SPPs travelling into a wedge become gradually more and more confined, resulting in extremely high electric field enhancements at the end [79]. Experimental results of confined plasmonic waveguiding was first shown with metal stripes, figure 3.3 (a) [80]. Silver stripes of 60 nm thick and widths down to 1 μm deposited on a glass substrate were proven to guide SPPs with a free-

space wavelength of 633 nm. Unfortunately the propagation length was decreased to several micrometers and while the lateral confinement of 1 μm was promising, it is clearly not below the wavelength. Energy transfer along a chain of 90 nm long silver rods was shown shortly after, figure 3.3 (b). Strictly not a SPP waveguide as it uses the hopping of LSPRs from one rod to the other, it did show the possibility of true sub-diffraction light propagation [81]. Unfortunately, propagation losses were even higher, severely limiting the potential use of these structures. Waveguides providing both reasonable propagation lengths and strong confinement in all dimensions were developed shortly after in the past decade. Bozhevolnyi *et al.* demonstrated that V-shaped grooves milled in a gold substrate support modes bound to the bottom of the groove with propagation lengths around a 100 μm for telecom wavelengths [82]. Combined with the efficient guiding of the light around sharp bends, it proved the potential of plasmonic waveguides for densely integrated planar photonics, illustrated by Mach-Zehnder interferometers and ring resonators, shown in figure 3.3 (c) [83]. The inverse, a metal wedge instead of groove, can also exhibit strongly confined single mode behaviour, as reported in 2005 at visible wavelengths, albeit with limited propagation lengths [84]. Improved fabrication techniques have recently delivered groove [85] and wedge structures [86] with more favourable optical properties. Although these publications showed that improvements are still to be made, a consensus has emerged that any plasmonic waveguide design will always have a trade-off between confinement and propagation loss [87]. This clearly strongly compromises the original vision of using plasmonic waveguides for large integrated photonics networks. It has been shown possible to create a limited number of passive elements in a network, but the real strength of structures based on plasmonic waveguides lays in the integration with dielectric photonics and active devices.

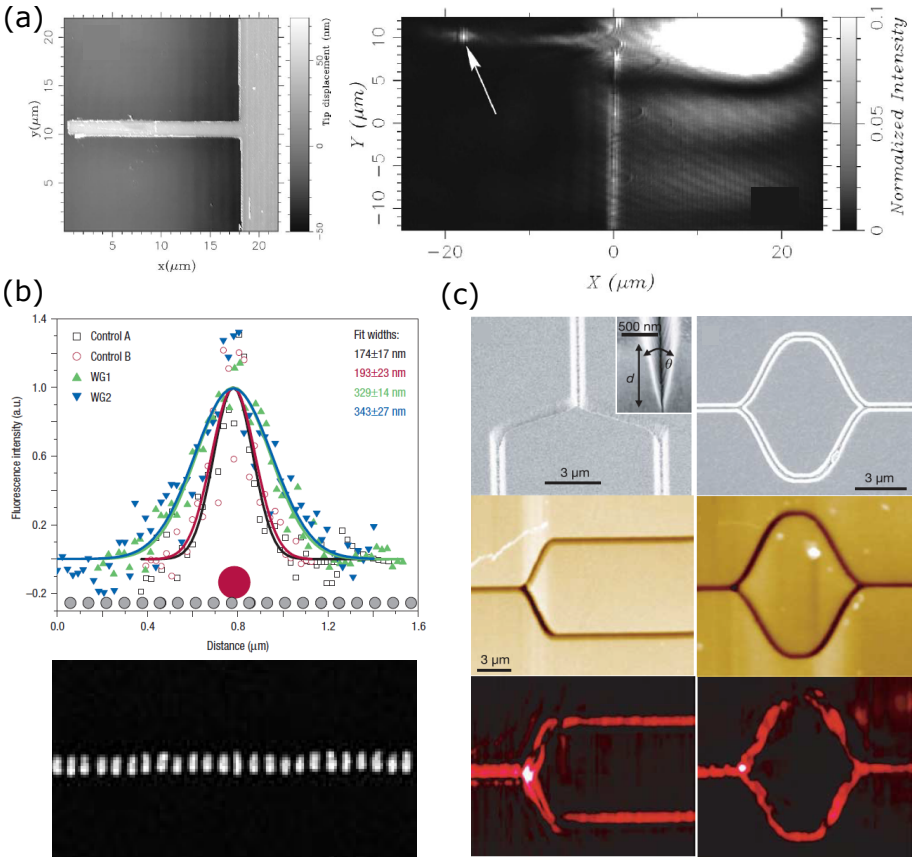


Figure 1.8: **(a)**, Micro-stripe silver waveguides on a glass substrate. The waveguide is coupled to a large thin film area, used to couple photons to SPPs with the Kretschmann technique [80], reprinted with permission from APS Physics. **(b)**, True sub-diffraction light propagation by the hopping of LSPRs from silver rod to rod, SEM of the chain shown below. The energy transfer is detected by a widened spread of the light intensity of fluorescent nano-spheres, shown at the top [81]. Reprinted with permission from NPG. **(c)**,SEM image, topographical and near-field optical SNOM images of highly miniaturized Y-splitters (left) and interferometers (right) [83]. Reprinted with permission from NPG.

2

QUANTUM OPTICS AND PLASMONICS

2.1 QUANTUM OPTICS

2.1.1 *Field quantization*

The semi-classical model for light-matter interaction, in which quantum-mechanics is used to describe the atoms but the electromagnetic field is considered classical, has been successful in describing many processes including absorption and stimulated emission. A notable exception is spontaneous emission, an isolated atom (or any level-system) in an excited state will stay in this state according to quantum-mechanics, as it is in a eigenstate of the Hamiltonian. It is the coupling with the vacuum fields of the electromagnetic modes that make the atom decay in the seeming absence of electromagnetic fields. Later plenty of effects were shown where quantization of the electromagnetic field was even necessary far away from any atomic system to make correct predictions. This showed the limitations of the semi-classical approach. Single-photon anti-bunching, photon entanglement and quantum interference effects are examples of this that have, since their discovery as fundamental effects, moved to the core of quantum optics and quantum technology research. The quantization procedure for free electromagnetic radiation in a vacuum has thus been treated in-depth in many textbooks [88, 89].

Quantization of the electromagnetic field in a general lossy and dispersive material is theoretically a more challenging problem than the vacuum case, but a range of solutions have been proven in the recent years [90]. For SPPs propagating along a metal surface or plasmonic waveguide, an approximate approach largely equivalent to the free space problem is possible [91, 92]. The simplest case of an extended flat metal-vacuum interface (along Cartesian coordinates x and y) is defined by the permittivity of the metal $\epsilon(\omega)$ for coordinate $z < 0$ and

$\epsilon = 1$ for $z > 0$. We start with the expression for the vector potential of the Maxwell equations $\mathbf{A}(\mathbf{r}, t)$ in the Coulomb gauge ($\nabla.\mathbf{A}(\mathbf{r}, t) = 0$):

$$\mathbf{A}(\mathbf{r}, t) = \int \frac{d^2\mathbf{K}}{(2\pi)^2} \alpha_{\mathbf{K}} \mathbf{u}_{\mathbf{K}}(z) exp(i\mathbf{K}.\mathbf{r}) exp(-i\omega_{spp} t) + c.c., \quad (2.1)$$

$\mathbf{K}$ is real wave vector parallel to the interface, ω_{spp} is a solution of $K = \frac{\omega_{spp}}{c}\sqrt{\frac{\epsilon(\omega_{spp})}{\epsilon(\omega_{spp})+1}}$ and α_K is an amplitude associated with $\mathbf{K}$ in the decomposition. $\mathbf{u}_{\mathbf{K}}(z)$ is a mode function, representing the modal shape of the SPP. This can be taken from waveguide structures like wedges or nanowires, but here the derivation is done for the case of an extended flat metal surface:

$$\mathbf{u}_K(z) = \frac{1}{\sqrt{L(\omega_{spp})}} exp(-i\kappa_j z) \left(\check{\mathbf{K}} - i\frac{K}{\kappa_j} \check{\mathbf{z}} \right), \quad (2.2)$$

$L(\omega_{spp})$ is a normalization constant, κ_j the projection of the wave vector to the axis perpendicular to the surface (along the unit vector $\check{\mathbf{z}}$), given by $\kappa_j = \frac{\epsilon_j(\omega_{spp})\omega_{spp}^2}{c^2} - K^2$ ($\kappa_{1,2}$ are the solutions chosen for $\pm$ z), and thus gives the decay length of the field perpendicular to the surface. $\check{\mathbf{K}}$ is the unit vector along $\mathbf{K}$. The vector potential can be expressed in a discrete sum of spatial Fourier components by assuming the field of interest is enclosed in a finite volume, for the free space vacuum derivation typically a virtual cube with sides L, but now due to the two-dimensionality of the structure a surface S with sides L_x and L_y. The wave vector can now only take quantized values ($K_x = \frac{n_x 2\pi}{L_x}$ and $K_y = \frac{n_y 2\pi}{L_y}$); the integration over $\mathbf{K}$ ($\int \frac{d^2\mathbf{K}}{(2\pi)^2}$) and the amplitude α_K in equation 2.1 can be replaced by the discrete sum $\frac{1}{S}\sum_{\mathbf{K}}$ and $SA_{\mathbf{K}}$ respectively:

$$\mathbf{A}(\mathbf{r}, t) = \sum_{\mathbf{K}} A_{\mathbf{K}} \mathbf{u}_{\mathbf{K}}(z) exp(i\mathbf{K}.\mathbf{r}) exp(-i\omega_{spp} t) + c.c.. \quad (2.3)$$

While the electromagnetic energy density in a vacuum is easily defined as $u = \frac{\epsilon_0}{2}\mathbf{E}^2(\mathbf{r}, t) + \frac{1}{2\mu_0}\mathbf{B}^2(\mathbf{r}, t)$, it is a more subtle problem problem in general lossy dispersive materials. Fortunately, for SPPs at flat surfaces or standard waveguides the influence of loss on the dispersion relationship is rather small and can be set o in a first approximation. Calculating the total energy of the electromagnetic field can thus be done with u ($U = \int dt \int u d\mathbf{r}$). Using the discrete modes in the virtual square the result is:

$$U = \sum_{\mathbf{K}} \epsilon_0 \omega_{spp}^2 S \left[A_{\mathbf{K}} A_{\mathbf{K}}^* + A_{\mathbf{K}}^* A_{\mathbf{K}} \right]. \quad (2.4)$$

Thanks to the lossless approximation, U is real and we can try to find an equivalent Hermitian operator for the quantum-mechanical model. The energy of each mode **K** has the structure of an uncoupled harmonic oscillator. By correspondence each can be replaced by the quantum-mechanical description of the harmonic oscillator:

$$\hat{H} = \sum_{\mathbf{K}} \frac{\hbar\omega_{spp}}{2}\left[\hat{a}_{\mathbf{K}}\hat{a}_{\mathbf{K}}^{\dagger} + \hat{a}_{\mathbf{K}}^{\dagger}\hat{a}_{\mathbf{K}}\right] = \sum_{\mathbf{K}} \hbar\omega_{spp}\left[\hat{n}_{\mathbf{K}} + \frac{1}{2}\right], \quad (2.5)$$

with :

$$A_{\mathbf{K}} \to \sqrt{\frac{\hbar}{2\epsilon_0\omega_{spp}S}}\hat{a}_{\mathbf{K}} \text{ and } A_{\mathbf{K}}^{*} \to \sqrt{\frac{\hbar}{2\epsilon_0\omega_{spp}S}}\hat{a}_{\mathbf{K}}^{\dagger}. \quad (2.6)$$

This introduces the annihilation and creation operators of the electromagnetic field, $\hat{a}_{\mathbf{K}}$ and $\hat{a}_{\mathbf{K}}^{\dagger}$ respectively, which act on a mode containing a discrete number n of excitations in the following way:

$$\hat{a}_{\mathbf{K}}^{\dagger}|n_{\mathbf{K}}\rangle = \sqrt{n_{\mathbf{K}}+1}\,|n_{\mathbf{K}}+1\rangle \quad (2.7)$$

$$\hat{a}_{\mathbf{K}}|n_{\mathbf{K}}\rangle = \sqrt{n_{\mathbf{K}}}\,|n_{\mathbf{K}}-1\rangle\,. \quad (2.8)$$

They respectively create and destroy a quantum of energy $\hbar\omega_{\mathbf{K}}$, a single Surface Plasmon Polariton, in the mode **K**. Different modes are independent and these operators thus obey the bosonic commutation relations $\left[\hat{a}_{\mathbf{K}}, \hat{a}_{\mathbf{K}'}^{\dagger}\right] = \delta_{\mathbf{K},\mathbf{K}'}$. With $\mathbf{E}(\mathbf{r},t) = \frac{\partial\mathbf{A}(\mathbf{r},t)}{\partial t}$ the electric field can finally be expressed as an operator acting on the quantized field:

$$\hat{\mathbf{E}}(\mathbf{r},t) = i\sum_{\mathbf{K}}\sqrt{\frac{\hbar\omega}{2\epsilon_0 S}}\mathbf{u}_{\mathbf{K}}(z)\hat{a}_{\mathbf{K}}exp(i\mathbf{K}.\mathbf{r})exp(-i\omega t) + H.c., \quad (2.9)$$

with H.c. the hermitian conjugate. The hermitian conjugate part is typically referred to as $\hat{\mathbf{E}}^{(-)}(\mathbf{r},t)$, while the first part is $\hat{\mathbf{E}}^{(+)}(\mathbf{r},t)$. The magnetic field can be similarly converted in a operator with $\mathbf{B}(\mathbf{r},t) = \nabla\times\mathbf{A}(\mathbf{r},t)$, but is of lesser importance in the rest of this work. For a metal surface or plasmonic waveguide without cavity structure, there are is a continuum of modes in terms of $\mathbf{K} = (\frac{n_x 2\pi}{L}, \frac{n_y 2\pi}{L})$. This is achieved by taking the limit of $L\to\infty$ and replacing the sum by an integral of K times the density of states in **K**-space $(\frac{L}{2\pi})^2$: $\sum_{\mathbf{K}} \to (\frac{L}{2\pi})^2\int d\mathbf{K}$. A factor $\frac{L}{2\pi}$ is absorbed into the annihilation operator: $\hat{a}_{\mathbf{K}} \to \frac{2\pi}{L}\hat{a}(\mathbf{K})$. The result for electric field operator in the continuous case is [93]

$$\hat{\mathbf{E}}(\mathbf{r},t) = \frac{i}{2\pi}\int d\mathbf{K}\sqrt{\frac{\hbar\omega}{2\epsilon_0}}\mathbf{u}(\mathbf{K},z)\hat{a}(\mathbf{K})exp(i\mathbf{K}.\mathbf{r})exp(-i\omega t) + H.c.. \quad (2.10)$$

After the quantization in the lossless approximation, loss can be included by coupling the quantized SPPs to a reservoir bath of modes. This is a phenomenological approach where the coupling strength with the reservoir modes is determined from the imaginary part of the dielectric permittivity of the metal $\epsilon(\omega)$.

As pointed out throughout, the derivation is largely equivalent to the one for free space radiation, of course 2.4 becomes the exact expression for the energy of the electromagnetic radiation and the dispersion relations used to calculate the magnitude $K = |\mathbf{K}|$ and κ_j are changed to the light-line. The mode function $u_{\mathbf{K}}(z)$ in the derivation is replaced by a plane wave description, with the important consequence that the basis for a transverse plane wave spans a two-dimensional space, the light can be polarized in any direction perpendicular to $\mathbf{K}$. By defining arbitrary unit vectors $\mathbf{e}_j$ (j = 1,2) that span this space, we can adapt equation 2.10 to [94]:

$$\hat{\mathbf{E}}(\mathbf{r},t) = \frac{i}{(2\pi)^{3/2}} \sum_j \int d\mathbf{K} \sqrt{\frac{\hbar\omega(\mathbf{K})}{2\epsilon_0}} \mathbf{e}_j \hat{a}(\mathbf{K}) \times \exp(i\mathbf{K}.\mathbf{r}) \exp(-i\omega(\mathbf{K})t) + \text{H.c.}. \tag{2.11}$$

A common choice for $\mathbf{e}_{1,2}$ is two real perpendicular vectors, one example is horizontal and vertical polarization, which is the basis that will be used in chapter 5.

In the experimental work reported in this thesis, the concept of a single photon (or SPP) is central. Before we defined it as the single excitation with energy $\hbar\omega_{\mathbf{K}}$ in mode $\mathbf{K}$: $\hat{a}^\dagger_{\mathbf{K}} |0_{\mathbf{K}}\rangle$. This is the theoretical description of a perfectly monochromatic single photon, in reality photons always have a frequency spread with consequent finite coherence length. This can be constructed as a superposition of a single excitation on several modes:

$$|1\rangle = \sum_{\mathbf{K}} c_{\mathbf{K}} |0,...,0,n_{\mathbf{K}} = 1,0,...\rangle = \sum_{\mathbf{K}} c_{\mathbf{K}} |1_{\mathbf{K}}\rangle , \tag{2.12}$$

with $\sum_{\mathbf{K}} |c_{\mathbf{K}}|^2 = 1$. The state $|1\rangle$ is not an eigenstate of the separate number operators $\hat{n}_{\mathbf{K}}$, nor is it of the total Hamiltonian (equation 2.5). The evolution of the state (in the Schrödinger notation) through time is thus given by:

$$|1(t)\rangle = \sum_{\mathbf{K}} c_{\mathbf{K}} \exp(-i\omega_{\mathbf{K}} t) |1_{\mathbf{K}}\rangle . \tag{2.13}$$

Just as a pulse in classical optics, the wave packet of a single photon with a finite temporal length is constructed by the summation over a range of frequencies. The state $|1\rangle$ is an eigenstate of $\hat{n} = \sum_{\mathbf{K}} \hat{n}_{\mathbf{K}}$, which we will see is the relevant operator for photon detection.

2.1.2 *Optical detection and coherence*

In classical electromagnetics the electric field $\mathbf{E}(\mathbf{r}, t)$ is typically considered the quantity that is measured experimentally, with the decomposition in the complex conjugate fields $\mathbf{E}^{(\pm)}(\mathbf{r}, t)$ as mere useful mathematical constructions [95]. From the final results for $\hat{\mathbf{E}}(\mathbf{r}, t)$ in the previous section, we can see that is it not accurate for the quantized fields. $\hat{E}^{(+)}(\mathbf{r}, t)$ (the magnitude of $\hat{\mathbf{E}}^{(+)}(\mathbf{r}, t)$ along an arbitrary polarization) is the sum of annihilation operators and thus associated with photon absorption, while $\hat{E}^{(-)}(\mathbf{r}, t)$ represents photon emission. At low frequencies the energy $\hbar\omega$ of a single photon becomes negligible and it can become unclear if a test charge emits or absorbs photons; the implicit summing of of the components $\mathbf{E}^{(+)}(\mathbf{r}, t)$ and $\mathbf{E}^{(-)}(\mathbf{r}, t)$ is a correct assumption. At optical frequencies, photon detection generally involves photon absorption, we are explicitly measuring the positive frequency of the electric field operator: $\hat{E}^{(+)}(\mathbf{r}, t)$. The transition probability of an undefined detector at position $\mathbf{r}$ from an initial state $|i\rangle$ to a final state $|f\rangle$ is:

$$T_{if} = \left| \left\langle f \left| \hat{E}^{(+)}(\mathbf{r}, t) \right| i \right\rangle \right|^2 . \tag{2.14}$$

Glauber [95] defined an ideal photon detector as a system of negligible size which has a frequency-independent photoabsorption probability. The final state of the transition is not measured, we only care about the total counting rate. This means the transition probability has to be summed over all the possible final states $|f\rangle$:

$$\begin{aligned} I(\mathbf{r}, t) &= \sum_f \left| \left\langle f \left| \hat{E}^{(+)}(\mathbf{r}, t) \right| i \right\rangle \right|^2 \\ &= \sum_f \langle i| \hat{E}^{(-)}(\mathbf{r}, t) |f\rangle \langle f| \hat{E}^{(+)}(\mathbf{r}, t) |i\rangle \\ &= \langle i| \hat{E}^{(-)}(\mathbf{r}, t) \hat{E}^{(+)}(\mathbf{r}, t) |i\rangle \qquad (2.15) \\ &\propto \left\langle i \left| \hat{a}^\dagger \hat{a} \right| i \right\rangle . \qquad (2.16) \end{aligned}$$

We used the summation over a complete set of final states, $\sum_f |f\rangle \langle f| = 1$. The last step clearly shows that the measured intensity is proportional to the expectation value of the number operator $\hat{a}^\dagger \hat{a}$. For the

more general case of the initial state of the field not being a pure state but a mixture, the result can easily be extended:

$$I(\mathbf{r},t) = \sum_i p_i \langle i| \hat{E}^{(-)}(\mathbf{r},t)\hat{E}^{(+)}(\mathbf{r},t) |i\rangle \tag{2.17}$$

$$= \mathrm{Tr}\left[\hat{\rho}\hat{E}^{(-)}(\mathbf{r},t)\hat{E}^{(+)}(\mathbf{r},t)\right], \tag{2.18}$$

$\hat{\rho}$ is the density operator we will introduce more in-depth later.

In this work we are interested in more than just the intensity of the electromagnetic field at a certain point $\mathbf{r}$. We can similarly define the rate at which two separate detectors detect photons at two separate points in space and time:

$$\begin{aligned}\sum_f \left|\left\langle f \left| \hat{E}^{(+)}(\mathbf{r_1},t_1)\hat{E}^{(+)}(\mathbf{r_2},t_2)\right| i\right\rangle\right|^2 \\ = \langle i| \hat{E}^{(+)}(\mathbf{r_1},t_1)\hat{E}^{(+)}(\mathbf{r_2},t_2)\hat{E}^{(-)}(\mathbf{r_2},t_2)\hat{E}^{(-)}(\mathbf{r_1},t_1) |i\rangle \\ \propto \left\langle \hat{a}_1^\dagger \hat{a}_2^\dagger \hat{a}_2 \hat{a}_1 \right\rangle\end{aligned} \tag{2.19}$$

With the same extension for a mixed state as in equation 2.18. This can of course be extended to even higher order coincidence rates with more than two separate detectors. The most famous historical examples of higher order intensity measurement experiments, though, involve 2 detectors. Hanbury-Brown and Twiss conducted intensity correlation measurements with photo-detectors at both outputs of a beam splitter, figure 2.1 (a), with light entering only one input port, equivalent to correlating intensity measurements of the input beam at two different moments, so equation 2.19 with $(\mathbf{r},t_1)$ and $(\mathbf{r},t_2)$. This allowed them to probe how bunched photons arrive in time when coming from a specific source of light [96], the difference between single photons, coherent sources and thermal light became well known since then [97]. In 1987 Hong, Ou and Mandel showed the outcome of two single photons arriving at the two input modes of a beam splitter, depicted in figure 2.1 (b). An intensity measurement at one of the outputs does not reveal anything surprising, but the correlated intensity of the two outputs does show distinct quantum behaviour [37]. This effect is the basis of this thesis and we will analyse it more in depth in the next section.

Historically, experiments probing the correlation between electric field amplitudes at 2 different places or times has been at the heart of the

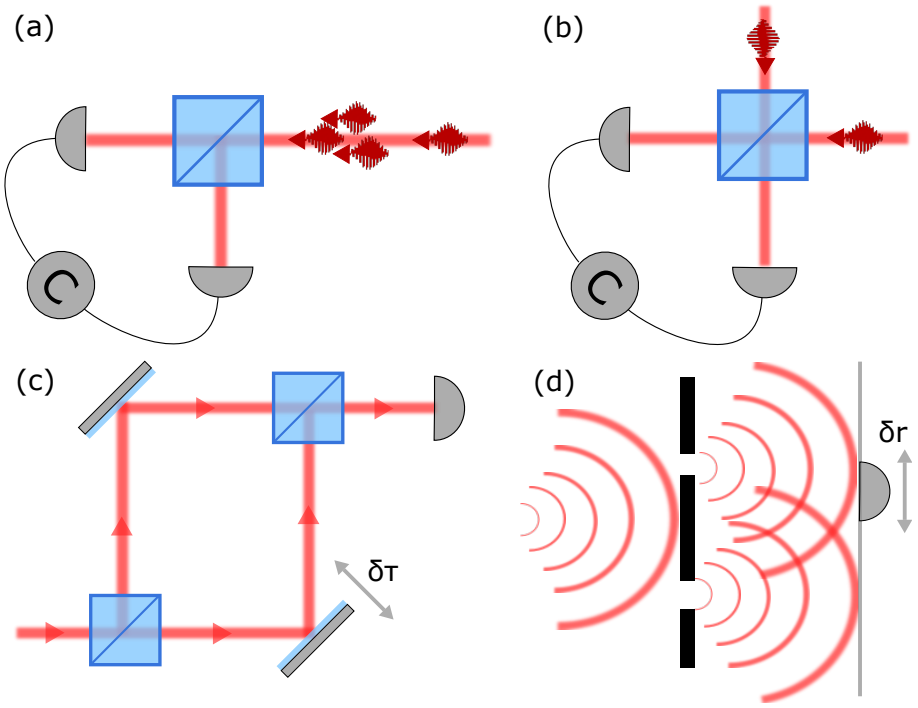


Figure 2.1: **(a)**, Hanbury Brown and Twiss set-up. **(b)**, Hong-Ou-Mandel experiment. **(c)**, Mach-Zehnder interferometer. **(d)**, Young's double slit experiment.

success of classical optics. First and higher order correlation functions can be defined with quantum operators as:

$$G^{(1)}(x_1;x_2) = \mathrm{Tr}\left[\rho\hat{E}^{(-)}(\mathbf{r_1},t_1)\hat{E}^{(+)}(\mathbf{r_2},t_2)\right] \tag{2.20}$$

$$G^{(n)}(x_1,...,x_n;x_{n+1},...,x_{2n}) = \mathrm{Tr}\left[\rho\hat{E}^{(-)}(x_1)...\hat{E}^{(-)}(x_n)\hat{E}^{(+)}(x_{n+1})...\hat{E}^{(+)}(x_{2n})\right], \tag{2.21}$$

with x_j as a compact notation for $(\mathbf{r_j}, t_j)$. It can be easily shown that the interference fringes from scanning the delay-line in a Mach-Zehnder set-up, figure 2.1 (c), or the position along the photographic plate in Young's double slit experiment, figure 2.1 (d), are related to the magnitude of $G^{(1)}(\mathbf{r},t_1;\mathbf{r},t_2)$ and $G^{(1)}(\mathbf{r_1},t;\mathbf{r_2},t)$ respectively [89]. Classical optics and quantum-mechanics with a quantized EM-field generally predict the same results for measurements probing a $G^{(1)}(\mathbf{r_1},t_1;\mathbf{r_2},t_2)$. In chapter 5, we will see how higher order correlations can be less straight-forward to measure.

2.1.3 *Quantum interference*

In 1987, Hong, Ou and Mandel showed the outcome of two single photons arriving at the two inputs of a 50/50 beam splitter [37]. The general relations between the annihilation operators of the bosonic input modes (mode 0 and 1) and output modes (mode 2 and 3) for a symmetric beam splitter are given by [98]:

$$\hat{a}_2 = (t\hat{a}_0 + r\hat{a}_1), \quad \hat{a}_3 = (r\hat{a}_0 + t\hat{a}_1). \tag{2.22}$$

The used labelling of the modes is shown in figure 2.2. Using these relations to calculate the output state with $|1\rangle_0 |1\rangle_1$ as an input state gives:

$$\begin{aligned} \hat{a}_0^\dagger \hat{a}_1^\dagger |00\rangle_{01} &\overset{BS}{\rightarrow} \frac{1}{t^{*2} - r^{*2}} (t^* \hat{a}_2^\dagger - r^* \hat{a}_3^\dagger)(-r^* \hat{a}_2^\dagger + t^* \hat{a}_3^\dagger) |00\rangle_{23} \\ &= \frac{-\sqrt{2} r^* t^*}{t^{*2} - r^{*2}} |20\rangle_{23} + \frac{-\sqrt{2} r^* t^*}{t^{*2} - r^{*2}} |02\rangle_{23} \\ &+ \frac{t^{*2}}{t^{*2} - r^{*2}} |11\rangle_{23} + \frac{r^{*2}}{t^{*2} - r^{*2}} |11\rangle_{23} \end{aligned} \tag{2.23}$$

$$= \frac{-\sqrt{2} r^* t^*}{t^{*2} - r^{*2}} (|20\rangle_{23} + |02\rangle_{23}) + \frac{t^{*2} + r^{*2}}{t^{*2} - r^{*2}} |11\rangle_{23} \tag{2.24}$$

In the case of a lossless 50/50 beam splitter, we can choose $t = \frac{1}{\sqrt{2}}$ and $r = \frac{i}{\sqrt{2}}$. The $\pi/2$ phase shift between r and t is necessary to make the output modes orthogonal, while energy conservation - $|r|^2 + |t|^2 = 1$ - implies $|r| = |t| = \sqrt{0.5}$ for a 50/50 beam splitter. Together they ensure that the bosonic commutator relationships between the different modes - $\left[\hat{a}_i, \hat{a}_j\right] = \delta_{ij}$ are satisfied [99]. Plugging these values into equation 2.24, we see that the $|1\rangle_2 |1\rangle_3$ component disappears; the two photons never leave the beam splitter into the separate output modes. Physically this can be understood in the following way: there are four ways for the photons to leave the beam splitter, as shown in figure 2.2. The two ways that deliver one photon at each output, both photons reflected or both transmitted, are indistinguishable for two detectors placed the behind outputs of the beam splitter, even in principle, as long as the photons itself are indistinguishable. Because of this -going from equation 2.23 to equation 2.24- the probability amplitudes of both situations are added before being squared to get the probability of detecting one photon at each output:

$$P_{23} = \left\langle \hat{a}_2^\dagger \hat{a}_3^\dagger \hat{a}_3 \hat{a}_2 \right\rangle = |t^* t^* + r^* r^*|^2 = \left| \frac{1}{\sqrt{2}} . \frac{1}{\sqrt{2}} + \frac{i}{\sqrt{2}} . \frac{i}{\sqrt{2}} \right|^2 = 0.$$

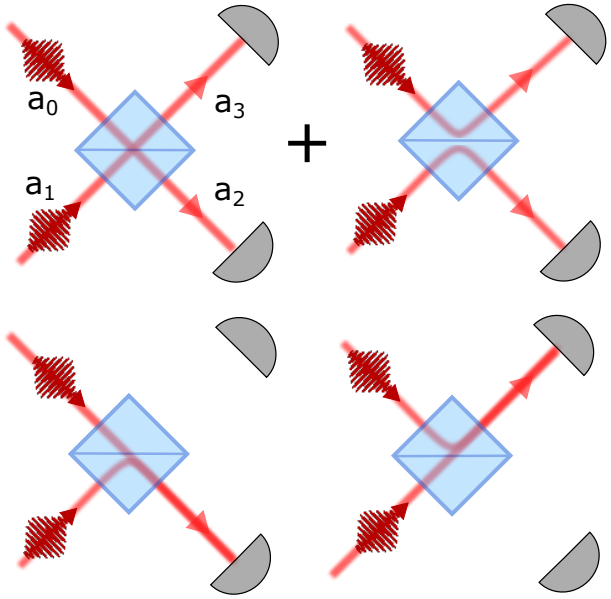


Figure 2.2: The four different combinations of the two photons leaving the beam splitter. The top two interfere with each other in the case of indistinguishable photons.

(2.25)

Due to the $\pi/2$ phase shift between reflectance and transmittance, both situations interfere destructively and the probability of one photon at each detector becomes zero. Note that when the two photons are not identical in a certain degree of freedom, so with different values α and β, the addition and consequent destructive interference does not happen because $|1_\alpha 1_\beta\rangle_{23} \neq |1_\beta 1_\alpha\rangle_{23}$. This could be the polarization, the frequency or, in the non-monochromatic case, the arrival time of the photons.

In the original experiment and most of the later variations on it, including our work, the 2 photons are generated as a photon pair in a nonlinear crystal by spontaneous parametric down-conversion, explained in section 4.2.1. As for any source, these photons have a certain spectral width and are in fact even frequency entangled. The spectral distribution of the bi-photon state can be represented by a linear superposition over the frequency ω [100]:

$$|\psi\rangle = \int d\omega \phi(\omega_0/2+\omega, \omega_0/2-\omega)\, |\omega_0/2+\omega, \omega_0/2-\omega\rangle\,, \quad (2.26)$$

with $\phi(\omega_1, \omega_0 - \omega_1)$ a weight function around $\omega_{1,2} = \frac{\omega_0}{2}$, ω_0 is the frequency of the pump laser. The wavepacket of the photons in the time domain is directly given by the Fourier transform of the weight function:

$$G(\tau) = \int \phi(\omega_0/2 + \omega, \omega_0/2 - \omega) e^{-i\omega\tau} d\omega \tag{2.27}$$

In most experiments, the shape of $\phi(\omega_1, \omega_0 - \omega_1)$ is determined by the spectral filters used on the down-converted photons, as the original output of the SPDC source is rather broadband. The observed coincidence counts by the detectors as a function of the difference in arrival time of the two photons entering the beam splitter, $\delta\tau$, can be calculated with $G(\tau)$ [37]:

$$N_c(\delta\tau) = C \left[|t|^4 + |r|^4 + 2Re(r^2 t^2) \frac{\int_{-\infty}^{+\infty} G(\tau) G(\tau - \delta\tau) d\tau}{\int_{-\infty}^{+\infty} G^2(\tau) d\tau} \right] \tag{2.28}$$

With C a constant to take into account the count rate. For the unitary 50/50 beam splitter, the normalized version of equation 2.28 simplifies to $N_c(\delta\tau) = 1 - \frac{\int_{-\infty}^{+\infty} G(\tau) G(\tau - \delta\tau) d\tau}{\int_{-\infty}^{+\infty} G^2(\tau) d\tau}$. When the time delay $\delta\tau$ between the photons is zero, the second term becomes one and the coincidence counts drop to zero, like in the case with two perfectly monochromatic photons explained before. When $\delta\tau$ deviates from zero, the second term goes to zero. The two photons gradually become distinguishable and the destructive interference disappears, coincidence counts do happen. This difference in arrival time at the beam splitter is normally done by inserting a delay line in one of the two paths from the nonlinear crystal to the beam splitter. The experimental results never show a perfect disappearance of coincidence counts. One of the reasons is the real values of r and t in equation 2.28. We can define a visibility of the interference as the normalized difference between the off-symmetry baseline of the experimentally measured coincidence counts and the the value at $\delta\tau = 0$:

$$V = \frac{N_c(\delta\tau = \infty) - N_c(\delta\tau = 0)}{N_c(\delta\tau = \infty)} \tag{2.29}$$

When the coincidence counts at the detectors fall below 50 % of the maximum amount of coincidences (when the two photons are perfectly distinguishable), so a visibility of over 0.5, it proves the bosonic nature of the photons. It was theoretically shown that in the general case of two separately positioned correlated detectors, the modulations in coincidence counts can never go over 50 % with classical

light without a definite phase relation between the two beams [101, 102]. This 50 % limit was shown experimentally with the fluorescent light from a dye laser [103]. Breaking the limit with two photons coming from a parametric down-conversion source, which do not have a definite phase relationship, -as we will do later- can thus only be explained non-classically. This effect was considered seminal in the quantum optics community. It is also crucial in Linear Optical Quantum Computation (LOQC) schemes [21, 104] and it allowed the authors of the original publication [37] to show that the two photons in photon pairs generated in parametric down-conversion are generated simultaneously, with an accuracy of several orders of magnitude better than the resolution of the used photon detectors.

With quantum computation and communication applications in mind, the interference effect has been shown with a plethora of other single photon sources. Photons coming from a variety of quantum emitters like quantum dots [105, 106], single trapped atoms [107], organic molecules [108], Nitrogen-vacancy [109, 110] and Silicon-vacancy centres [111] in diamond have all been used to show this quantum interference effect. This has been done by interfering two sequentially emitted photons from the same emitter or with two photons coming from two separate emitters. As the visibility of the interference is directly related to the indistinguishability of the photons [112], the former experiment allows to probe the (spectral) stability of the emitter over time, while the latter shows the possibility of creating two identical sources. These two features are vital for the success of any photon source scheme, and it is thus no surprise that the experiment is conducted with any quantum emitter platform that claims to be the future of quantum optics technology.

2.1.4 *Density operator*

A density operator is the most general description of a quantum state. It allows us to obtain maximal information about pure states and mixed states, which are a statistical ensemble of pure states $|\Psi_n\rangle$ with probabilities p_n, $\rho = \sum_n p_n |\psi_n\rangle \langle\psi_n|$. Pure states can be represented as a state vector in the Hilbert space, whereas mixed states cannot. The expectation value $\langle \hat{A} \rangle$ of a physical quantity is the weighted av-

erage of the expectation values $\langle\Psi_n|\hat{A}|\Psi_n\rangle$ for the individual pure states of the mixed state ensemble, so [113]:

$$\langle\hat{A}\rangle = \sum_n p_n \langle\Psi_n|\hat{A}|\Psi_n\rangle \tag{2.30}$$

$$= \sum_a \sum_n p_n \langle\Psi_n|\hat{A}|a\rangle\langle a|\Psi_n\rangle \tag{2.31}$$

$$= \sum_a \langle a| \sum_n p_n |\Psi_n\rangle\langle\Psi_n|\hat{A}|a\rangle . \tag{2.32}$$

As the density operator is defined as:

$$\hat{\rho} = \sum_n p_n |\Psi_n\rangle\langle\Psi_n| , \tag{2.33}$$

we can write equation 2.32 as:

$$\langle\hat{A}\rangle = \mathrm{Tr}\left[\hat{\rho}\hat{A}\right] . \tag{2.34}$$

This shows the importance of the density operator, it allows to predict the expectation value of any measurement and contains as such all the information we can obtain of a state. The representation of a density operator in a given basis $\{|m\rangle\}$ is called the density matrix:

$$\hat{\rho} = \sum_{mn} \rho_{mn} |m\rangle\langle n|, \tag{2.35}$$

with ρ_{mn} the elements of the density matrix ρ. From definition 2.33 it is clear that the density operator is Hermitian and thus so is the density matrix in any basis. The density operator has several other characteristics, first of all it is normalized:

$$\mathrm{Tr}[\hat{\rho}] = \sum_n p_n \mathrm{Tr}\left[|\Psi_n\rangle\langle\Psi_n|\right] = \sum_n p_n \langle\Psi_n|\Psi_n\rangle = 1, \tag{2.36}$$

as $\sum_n p_n = 1$ for any statistical ensemble. Furthermore it is positive semi-definite, for every vector $|\Psi\rangle$:

$$\langle\Psi|\hat{\rho}|\Psi\rangle = \sum_n p_n |\langle\Psi|\Psi_n\rangle|^2 \geqslant 0. \tag{2.37}$$

For the density matrix this means that all eigenvalues have to be real and non-negative. This is not surprising, considering that the eigenvalues λ_n of the matrix are the probabilities of the state being in the respective eigenstate; in the eigenbasis $p_n = \lambda_n$.

FIDELITY Fidelity is a measure of distance between two quantum states, for two states ρ and σ it is defined as [114]:

$$F(\rho, \sigma) \equiv Tr\left[\sqrt{\rho^{1/2}\sigma\rho^{1/2}}\right]^2 \tag{2.38}$$

The fidelity between a pure state $|\Psi\rangle$ and an arbitrary state ρ simplifies to:

$$F(|\Psi\rangle, \rho) = \langle\Psi|\rho|\Psi\rangle \tag{2.39}$$

Which is the overlap between the two states. The fidelity ranges from 0, the two states are fully orthogonal, to 1, they are identical or completely overlapping. This means fidelity can be used to compare an experimentally obtained density matrix with the theoretically expected (pure) state.

2.1.5 *Entanglement*

Entanglement is considered one the core traits of quantum mechanics. The non-local interactions between particles allowed by quantum mechanics spurred fierce debates about the local reality of Nature from the very start [8]. The Bell inequalities can be seen as the defining measure for the entanglement between subsystems S^A and S^B of system S. An entangled system can break limits set up by John Stewart Bell in 1964 that draw the border for local realist theories [9]. Quantum optics has throughout the years played a crucial role in this fundamental research of the status of quantum mechanics [18, 115]. In the recent decades quantum information theory has nothing less than exploded. Quantum systems promise revolutionary applications in the form of quantum simulation, computation [116, 117] and metrology [118]. All of them are in some way related to and dependent on entanglement between the particles used in the system, often photons, and it has thus become important to define entanglement beyond the Bell measurements [119]. Local (quantum) operations on the two subsystems S^A and S^B and classical communication between them turns out to be the defining feature of entanglement: any system S with two distant subsystems S^A and S^B that can be generated with purely local operations and classical communication is not entangled, while any system that can not be created this way is. This operational view has been shown to be equivalent to the mathematical separability of

the density operator of the state S. A quantum system S containing two subsystems S^A and S^B is separable when it can be represented as a statistical mixture of product states of the subsystems S^A and S^B [120]:

$$\rho^{AB} = \sum_{r=1}^{m} p_r \rho_r^A \otimes \rho_r^B, \quad p_r > 0, \quad \sum_r p_r = 1. \tag{2.40}$$

The equivalence creates the following definition for entanglement: *A quantum state is entangled when it is not separable.*

On top of a definition, a measure of entanglement that allows to quantify entanglement in different states and compare between them would be of great use. Such an entanglement measure E should give 0 for non-entangled states, can be normalized to 1 for maximally entangled states (which are proven to exist) and should not increase under any LOCC (Local Operations and Classical Communication). It was shown by Popescu *et al.* that the Entropy of Entanglement is the only measure for pure states obeying all these requirements in the most general circumstances [121]. It is based on the Von-Neumann entropy, which is defined as an extension of the Shannon entropy to quantum physics:

$$E \equiv -\mathrm{Tr}\left[\hat{\rho} \ln\left[\hat{\rho}\right]\right]. \tag{2.41}$$

In a pure state, there is no uncertainty about the state, which means the entropy (the indeterminacy) is zero. We can also define the entropy of the subsystems S^A and S^B:

$$E(S^A) \equiv -\mathrm{Tr}\left[\hat{\rho}^A \ln\left[\hat{\rho}^A\right]\right], \text{ with } \hat{\rho}^A = \mathrm{Tr}_B\left[\hat{\rho}^{AB}\right], \tag{2.42}$$

$\hat{\rho}^A$ is thus the density matrix of the subsystem A, obtained by taking a partial trace over the system B. When the composite pure system is in a product state (no correlations between subsystem A and B), the same reasoning as for the entropy of the complete state applies: the maximum information is present and both $E(S^A)$ and $E(S^B)$ are zero. When there are correlations between the two subsystems however, there is information contained in these correlations and this information is lost when only looking at the subsystems separately; the entropy of the subsystems is more than 0. The entropy of the subsystems is thus a measure of entanglement between the subsystems of the pure state [121]:

$$0 \leqslant E\left[\hat{\rho}\right] \equiv S_A = S_B \leqslant 1. \tag{2.43}$$

This is the Entropy of Entanglement. If with LOCC k copies of the maximally entangled state (of the same dimension) can be distilled out of n copies of the original state, the Entropy of Entanglement is equal to the ratio $\frac{k}{n}$ for $n \to \infty$, it is thus the 'distillable entanglement'. The number k will also be the amount of maximally entangled states needed to create the n copies for $n \to \infty$, the Entropy of Entanglement is thus also equal to the 'entanglement of formation' [122]. Finding a general entanglement measure for mixed states is still largely unsolved, with only measures available for some specific cases. The most famous is the Entanglement of Formation for a mixed state of two 2-level (qubit) systems [123], which is based on the Entropy of Entanglement. We will explain and use this measure to quantify the entanglement of the reconstructed density matrix in chapter 5.

2.2 QUANTUM PLASMONICS

Quantum plasmonics has throughout the years started attracting interest from a range of communities: plasmonics researchers looking to push the limits of the technology [124], quantum optics groups searching for new ways to achieve stronger light-matter interaction with quantum emitters [62], quantum information theorists interested in the influence of dissipation and decoherence on quantum coherence and hoping to find unexpected ways to use plasmonic losses as a tool [125, 126]. It is no surprise there is currently a wide range of research going on under the umbrella of quantum plasmonics, we will give a short overview here.

2.2.1 *Fundamental studies*

Considered a starting point of the field, Altewischer *et al.* showed in 2002 that polarization entanglement between two photons was not degraded while travelling as SPPs [39]. Maximally polarization-entangled non-collinear photon pairs ($|\psi\rangle = \frac{1}{\sqrt{2}}(|H_1V_2\rangle - |V_1H_2\rangle)$) were generated by pumping a BBO nonlinear crystal by type II parametric down-conversion. Optically thick metal films with sub-wavelength hole arrays (a square grid of 200 nm diameter holes with a spacing of 700 nm) were placed on their paths. It is a well-known plasmonic effect (extraordinary optical transmission) that light travels through

these hole array structures considerably more efficiently than one would expect from diffraction theory alone, thanks to photon-SPP and SPP-photon conversion at the front and back of the film respectively. Rotating polarizers in front of single photon detectors showed that the correlations between the photon polarizations had not degraded while travelling through the holes as SPPs. This result surprised many researchers, as SPPs interact strongly with a macroscopic amount of electrons, estimated around 10^{10}. Many publications on the influence of plasmonic structures on quantum properties of light followed. The preservation of energy-time entanglement in similar structures with extraordinary transmission was shown [127], but a lot of interest went to more challenging and useful situations, where the light travels considerable distances as SPPs in plasmonic waveguides. It was shown that it is possible to create a single SPP travelling through a waveguide in a superposition of two widely separated moments of existence [128]. A Hong-Ou-Mandel experiment was conducted with photons after they travelled through a plasmonic waveguide, showing that the photons did not lose indistinguishability in this process [129]. Furthermore, it was shown that the loss in SPP waveguides does not have an influence on the second order coherence function of single photons [130]. Quadrature squeezed light has been shown to preserve its squeezed properties, both after propagating as SPPs in waveguides [131] and after travelling through an array of silver nanoparticles as Localized Surface Plasmon Resonances [132]. Two-mode squeezed states have already shown their use in a specific type of plasmonic sensor, obtaining sensitivities below the limits set by shot noise [124, 133]. In general, all these results show that quantum properties of light are robust in plasmonic structures, which means that these structures are potentially useful in photonic quantum technologies like quantum metrology and quantum information processing [2].

Probing the bosonic nature of SPPs by performing a Hong-Ou-Mandel interference experiment with a plasmonic beam splitter has received a lot of attention in the recent years. Heeres *et al.* reported an interference visibility of 43 %, thus not conclusively showing the quantized nature of SPPs [36]. The highly miniaturized design, with micron-sized near-field detectors, did show the tantalizing possibilities of a fully integrated approach. Several groups reported on successful in-

terference experiments with visibilities considerably higher than 50 % in 2014. Fakonas *et al.* used 50/50 directional couplers made of two dielectric-loaded gold SPP waveguides and obtained a 93 ±1% visibility, showing there was no significant degradation compared to the photonic case [33]. The efficient coupling of the SPP waveguides to silicon nitride waveguides on the chip could help to connect the beam splitter to a range of optical components. Directional couplers of dielectric-loaded and long-range SPP waveguides were also used to show high (> 90%) visibilities at the telecom wavelength [34, 35]. Also in 2014, we published our results on a Hong-Ou-Mandel interference, but as the only group with a semi-reflective Bragg scattering structure, not directional couplers [1]. Low signal rates and consequent high noise created a very challenging experiment, but we did obtain a visibility of 0.72 ±0.13, shown in figure 2.3. In chapter 4, we will show that a scattering-based approach has advantages (potentially extremely compact), but also creates extra challenges; the scattering creates an extra loss channel that can change the phase relations of the beam splitter. Very recently, a publication showed that this can even convert the HOM dip into a HOM peak, the photons anti-coalesce instead of coalesce [134].

2.2.2 *Light-matter interactions*

Of course, plasmonic structures have to do more than not destroy quantum effects to be useful for quantum optics research and quantum technologies. The demonstrated merging of a well-established plasmonic sensing technique with the fundamental sensitivity improvements promised by quantum metrology is an excellent example [124]. For optical quantum computing, plasmonics bears the same promises as for classical optical computing, the sub-diffraction guiding of light could scale down future quantum processors and help bridge the size mismatch between photonics and electronics.

2.2.2.1 *Sources and switches*

Bridging the size mismatch between photonics and electronics can take a rather different meaning in quantum optics: obtaining coherent photon-quantum emitter interactions and photon-photon interactions mediated by a quantum emitter have been very challenging due to the size mismatch between photons and typical quantum emitters

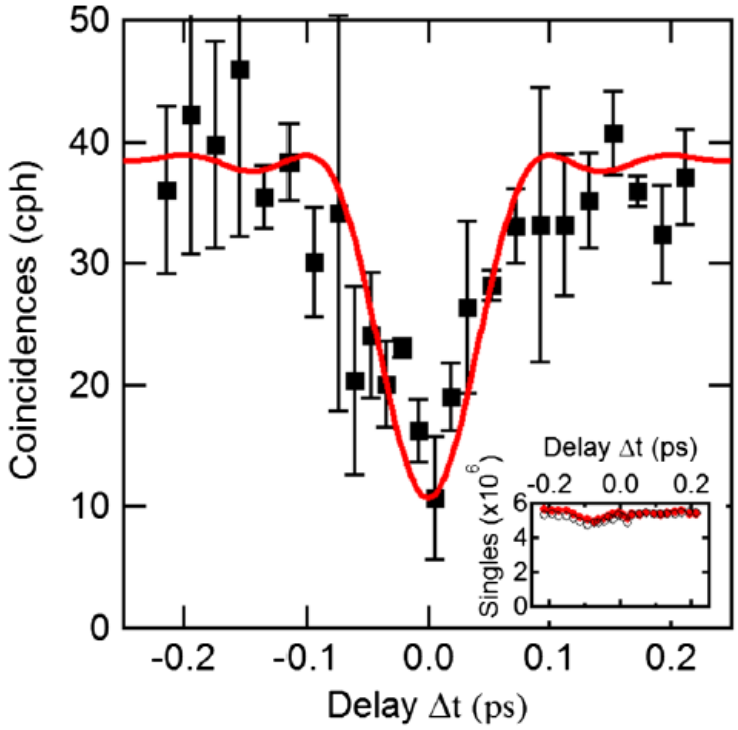


Figure 2.3: Plasmonic Hong-Ou-Mandel interference with a scattering-based plasmonic beam splitter [1]. Reprinted with permission from APS Physics.

like quantum dots, molecules and vacancy centres in diamond. One way to improve the interaction between emitters and light modes in dielectric optics has been the use of cavities. The coupling strength of a dipole with a cavity is often quantified by the Purcell factor [135]:

$$F = \frac{\gamma_{cavity}}{\gamma_{free\ space}} = \frac{3Q}{4\pi^2 V_{eff}} \left(\frac{\lambda}{n}\right)^3, \tag{2.44}$$

where γ is the decay rate of the emitter, V_{eff} the effective mode volume of the optical mode and Q the quality factor of the cavity. The Purcell factor is thus the increase of the decay rate of the emitter in the cavity compared to the emitter in free space. Micro-cavities like photonic crystals and micro-pillars have been very successful in attaining extremely high Purcell factors mainly thanks to improving the quality factor of the cavity, and thus the interaction time between the emitter and the photon, as the mode volume is ultimately limited by the diffraction limit. As we know by now, this is not the case for plasmonic waveguides, and high enhancements could be reached without high quality factors, purely by ultra-small mode volumes. Chang *et al.* theoretically showed it should be possible to achieve Purcell factors up to several hundreds purely by coupling quantum emitters to silver nanowires or tapered endings of silver nanowires [62]. Due to the lack of cavities, these structures are broadband, they create less challenges with spectral tuning and are more suitable for broadband quantum emitters. Experimental verification of this idea was done for the first time by coupling CdSe quantum dots to silver nanowires, with diameters of around 100 nm. Moderate Purcell enhancements of the spontaneous emission of 2.5 were demonstrated [136]. Smaller nanowires and closer emitter-wire coupling are needed to get optimal results, unfortunately making it harder to detect signal in the far-field. Combining plasmonic confinement with increased quality factors has also been shown with plasmonic resonators, obtaining high Purcell factors by patterning a cavity around a highly confined plasmonic waveguide [137]. Due to the propagation losses, it is more challenging to get high quality factors than with dielectric cavities. Great improvements have been reported with this approach with wedge waveguides, see figure 2.4 (a), thanks to novel fabrication techniques that create wedge waveguides with a very smooth surface, resulting in long propagation lengths [86]. The experimentally obtained Purcell factors of up to a 100 were only limited by the use of broadband colloidal quantum dots. With narrowband emitters values of up to a 1000 are possible.

When the emitter couplers very efficiently with the optical mode, the strong-coupling regime can be reached. In the strong-coupling regime, the coupling between the emitter and optical mode is higher than any other loss channel in the system, resulting in coherent oscillations between the excitation of the emitter and the optical mode, so-called Rabi oscillations. Theoretical investigation of several waveguide-based plasmonic resonators shows the strong-coupling regime could be within experimental reach, having higher coupling factors than the loss channels is of course more challenging in plasmonic systems than dielectric cavities [140]. Strong-coupling could be extremely useful to make single photons interact with each other, a basic need for many quantum computation schemes [114]. A three-level system strongly coupled to a silver nanowire for example could reflect incoming SPPs depending on the state of the emitter, which in its turn depends on the presence of a prior single photon pulse, the scheme is shown in figure 2.4 (b) [138]. Interesting, but experimentally even more challenging ideas have recently been suggested where 2 or more quantum emitters are strongly coupled to a plasmonic structure. It was shown that entanglement could be generated between two distant emitters coupled to wire or groove waveguides. Surprisingly, master equation calculations show that the dissipative part of the SPP mediated qubit-qubit coupling is crucial for the entanglement generation [126]. Many parameters, like the strength of the coupling, the positioning of the emitter relative to the waveguide and even the emitter-emitter distance [141], are crucial for these kind of architectures, progress in fabrication techniques is thus important for these more exotic quantum plasmonic ideas to materialize.

A different approach, with localized surface plasmon resonances, has recently shown that strong-coupling between a single molecule and a plasmonic mode can be reached. The structure is shown in figure 2.4 (c) [139]. A single molecule is positioned between a gold film and a gold nano-sphere with diameter 40 nm, in a gap of only 0.9 nm. The resulting spectra show how the resonance of the emitter couples with the cavity resonance, resulting in two new peaks; a clear sign of Rabi oscillations. An interesting feature about strong-coupling with plasmonic cavities is the low Q-factor, there is no big increase in interaction time, which makes the approach fundamentally fast [135]. Other

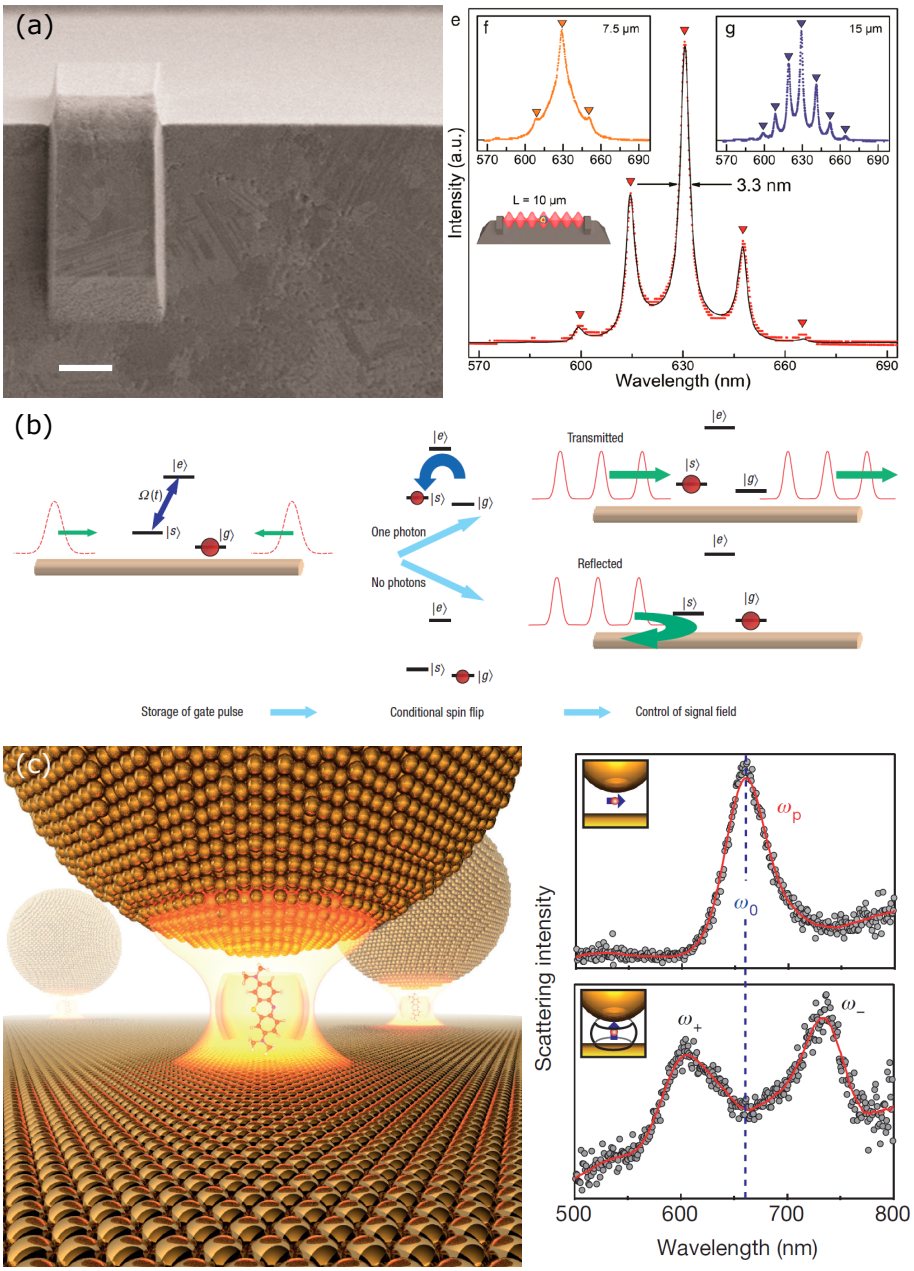


Figure 2.4: **(a)**, The left SEM picture shows half of a plasmonic resonator, consisting of an ultra-smooth wedge waveguide and two block reflectors, delivering a high-Q plasmonic resonator, as shown by the spectra on the right. Images taken from Kress *et al.* [86], with permission from ACS Publications. **(b)**, A 3-level system strongly coupled to a plasmonic waveguide can serve as a single SPP transistor. The reflection of the SPP is conditional on the excitation of the 3-level system, possible by a prior single SPP. Images taken from Chang *et al.* [138], with permission from NPG. **(c)**, The right shows the difference between the scattering intensity of the cavity shown left with a molecule coupled (bottom) and without a molecule coupled (top) to the optical mode of the cavity. The splitting of the scattering resonances are a clear sign of strong coupling. Images taken from Chikkaraddy *et al.* [139], with permission from NPG.

nanoparticle-on-mirror geometries have been shown to be promising structures to optimize quantum emitters as single photon sources; chemically synthesised mono-crystalline nano-cubes on gold films show Purcell enhancements up to several thousands for quantum emitters positioned in the narrow gap between, while still having excellent radiative properties [142]. Most of the emitted photons are radiated in a favourable angle for microscope objectives, rather than quenched, creating an ideal platform for single photon sources with high repetition rates.

2.2.2.2 *Detectors*

SPPs are typically detected in the far field, where photons scattered out of the waveguide are collected with a microscope objective and measured with cameras and single photon detectors. This is clearly not a very efficient scheme, especially as smaller plasmonic structures aimed at extremely high optical confinements scatter less into the far-field. Two different near-field detectors designs have proven to efficiently detect single photons. Figure 2.5 (a) shows a silver nanowire waveguide coupled to a germanium nanowire field-effect transistor. The oscillating electric field of the SPPs generates electron-hole pairs in the semiconductor, which are separated by an applied d.c. bias. The resulting current is then monitored, with a sensitivity proven to be high enough to detect single SPPs coming from a quantum dot [143]. A second approach uses a superconducting NbN wire meandering around the plasmonic waveguide [144], figure 2.5 (b), where SPPs absorbed by the wire introduce a small resistive region, creating a detectable voltage pulse. The result is a single SPP detector with extremely low timing jitter and short recovery times. Alternatively, superconducting based near-field detectors could even provide number-resolving capabilities, an extremely useful prospect for quantum computation schemes [145].

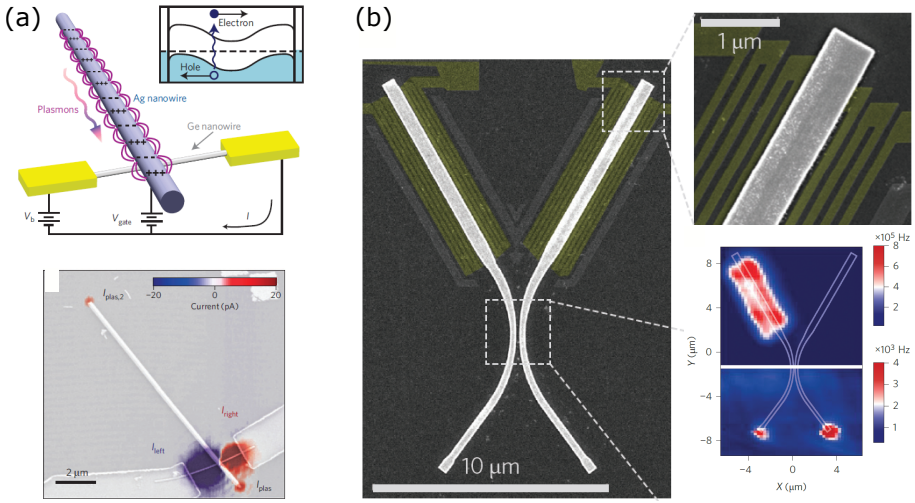


Figure 2.5: **(a)**, schematic depiction of a silver nanowire coupled to a germanium nanowire based near-field SPP detector. Image taken from Falk *et al.* [143], with permission from NPG. **(b)**, near-field detector based on a superconducting wire meandering around a stripe plasmonic waveguide. Image taken from Heeres *et al.* [144], with permission from NPG.

3

QUANTUM METROLOGY WITH SPPS

In this chapter theoretical work on the combination of two-mode entangled states with plasmonic waveguides to obtain quantum enhanced sensitivities in the measurement of a phase shift is presented. The phase shift is generated by the optical mode in a plasmonic waveguide with a variable surrounding medium. The concepts of measurement sensitivity and minimum resolution are introduced in section 3.1. The optical behaviour of the used waveguide structures, nanowires and wedge waveguides, are discussed in 3.3. The background of quantum enhanced measurements, quantum metrology, is explained in section 3.4. Combining the concepts of these sections allows us to present novel results in 3.5. A more compact presentation of all this can be found in our recent publication [3]. Images in this chapter are reprinted (adapted) with permission, copyright 2016 American Chemical Society.

3.1 INTRODUCTION

Plasmonic sensors have evolved to a mature technology in the recent decades, the sensitivity of SPPs on the refractive index of the surrounding material has made them an excellent tool for characterizing biomolecular interactions and concentrations. A range of techniques are being used and researched, including surface plasmon resonance sensors based on SPPs [4, 76] or LSPRs [27, 146], and the combination of plasmonic modes with molecular identification techniques such as Surface Enhanced Raman Spectroscopy (SERS) [73]. Several companies have already commercialized Kretschmann configuration based surface plasmon resonance sensors, where the excitation angle of SPPs can be accurately related to the refractive index of the material, typically a solution, at the top of the metal film [76].

Quantum techniques on the other hand have been shown to be able to outperform classical methods by providing measurements with resolutions below the shot-noise or standard quantum limit (SNL or SQL).

This limit is the lowest possible resolution of the estimated phase in an interferometry measurement and is dependent on the number of photons N in the state: $\frac{1}{\sqrt{N}}$. Non-classical entangled states can deliver precisions scaling as $\frac{1}{N}$, known as the Heisenberg limit, and research to optimal strategies is the core of a research field known as quantum metrology [13, 118, 147]. The improved scaling can be used to obtain higher precisions, or for keeping the same precision with a lower photon flux. This can be crucial for fragile samples, like biomolecules that can suffer from photodamage [148], or measurement techniques that suffer from heating induced measurement changes [149]. Recently, interest in quantum metrology strategies robust against imperfections has risen dramatically, especially robustness against loss in optical implementations is of high importance as it is crucial to push these implementations to applications [150].

These loss-robust schemes can also open to the door to SPP-based sensing with quantum states, potentially delivering highly sensitive and miniaturized devices for biological and chemical applications. Indeed, Pooser *et al.* [124, 133] showed that two-mode squeezed light, created with four-wave mixing in a Rubidium vapor, can be used to more accurately measure the excitation angle of SPPs in a Kretschmann-configuration SPR sensor. Although one of the leading SPP-based sensors, plasmonic sensors in a phase-sensitive interferometer-based scheme generally obtain higher sensitivities [151, 152]. We will here discuss phase-sensitive two-mode interferometry in which one mode travels through a plasmonic waveguide surrounded by a bio-solution with variable refractive index. Figure 3.1 shows the scheme of interest: a two-mode light state is prepared at the source stage, the photons in mode 1 will accumulate a surplus phase ϕ compared to mode 2 by travelling through a waveguide surrounded by a liquid solution. The measurement stage is optimized to estimate this phase difference ϕ.

3.2 SENSITIVITY

The refractive index n_{bio} in mode 1 is typically the quantity of interest, as it for example depends on the concentration of a solute of interest in a solution. The refractive index in turn influences ϕ, so we

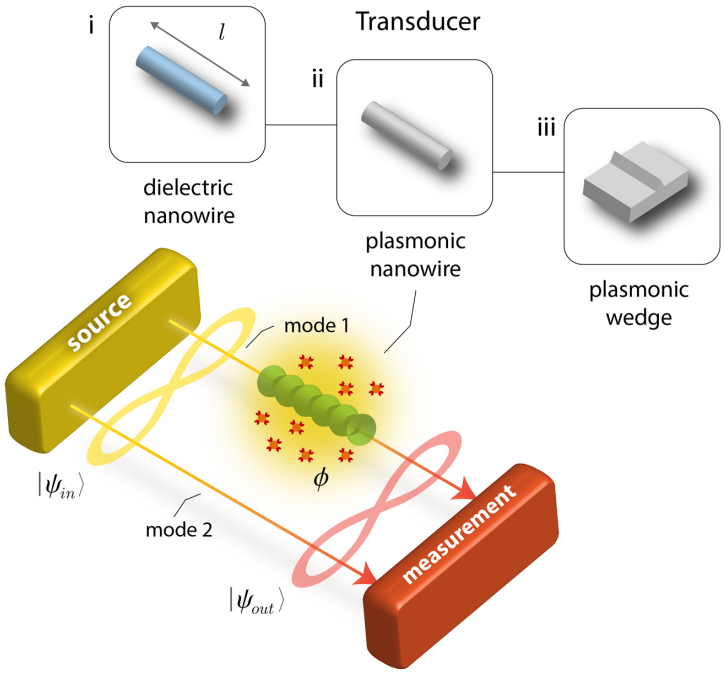


Figure 3.1: Schematic depiction of a general two-mode interferometer, one arm travels through a nano-waveguide, which transduces the changes of the surrounding refractive index onto the optical mode by a phase shift $\Delta\phi$. The quantum or classical state $|\Psi_{\mathrm{in}}\rangle$ is generated at the source stage and the phase shift is probed by measuring the output state $|\Psi_{\mathrm{out}}\rangle$ at the measurement stage.

write $\phi(n_{bio})$. The sensitivity of a sensor is defined as the ratio of the change in the sensor output $\langle\hat{O}\rangle$ to the change in n_{bio}:

$$S = \frac{\partial\langle\hat{O}\rangle}{\partial n_{bio}} = \frac{\partial\langle\hat{O}\rangle}{\partial\phi}\frac{\partial\phi}{\partial n_{bio}}. \tag{3.1}$$

For the wedge waveguide we take a realistic range between 1.333 and 1.44 for n_{bio}. Bovine Serum Albumin (BSA) in water, is an example of a well-characterized solution that can be used as a benchmark [153], with $n_{bio} = n_s + A \times C$, where $n_s = 1.333$ denotes water as a solvent, $A = 0.00182$ represents BSA and C is the number of grams of BSA per 100 mL of solution. For the nanowires we will limit the range up to 1.4 due to the lack of confinement for the dielectric case when n_{bio} comes too close to the value of the waveguide core $n_{silica} = 1.4475$. To still have an interesting range, we will extend it to 1.1 at the lower end side. From equation 3.1 one could think it is possible to resolve an arbitrarily small change in n_{bio} (and thus in C), by just measuring a small enough change in $\langle\hat{O}\rangle$: $\Delta n_{bio} = \frac{\Delta\langle\hat{O}\rangle}{S}$. Unfortunately, due to the quantum nature of light, the observable $\hat{O}$ has a certain uncertainty, imposing a minimum resolution on the measurement of the quantity of interest. The minimum resolution can be related to the uncertainty of the the observable $\hat{O}$ by the linear error propagation method [154]:

$$\Delta n_{bio} = \frac{\Delta\hat{O}}{\left|\partial\langle\hat{O}\rangle/\partial n_{bio}\right|}. \tag{3.2}$$

$(\Delta\hat{O})^2$ is the variance of the observable and thus $\Delta\hat{O} = \sqrt{\langle\hat{O}^2\rangle - \langle\hat{O}\rangle^2}$. Using the chain-rule, we convert the expression for the minimum resolution of n_{bio} to

$$\begin{aligned}\delta n_{bio} &= \frac{\Delta\hat{O}}{\left|\frac{\partial\langle\hat{O}\rangle}{\partial\phi}\frac{\partial\phi}{\partial n_{bio}}\right|} \\ &= \delta\phi\left|\frac{\partial\phi}{\partial n_{bio}}\right|^{-1},\end{aligned} \tag{3.3}$$

where the expectation value $\langle\hat{O}\rangle$ is assumed to only be dependent on n_{bio} through ϕ. The minimum resolution for n_{bio} can clearly be split into two parts. The first part in equation 3.3, $\delta\phi$, depends on the measurement observable and the output state $|\Psi_{out}\rangle$, it is this part that can be decreased under the shot noise limit with the right choice of source and measurement. An effect also referred to as super-sensitivity [155, 156]. We will explain this in section 3.4.

The sensitivity of ϕ on n_{bio}, $\frac{\partial\phi}{\partial n_{bio}}$, on the other hand, depends on the waveguide structure used and can be improved by using a plasmonic transducer. The total relative phase picked up is given by the propagation constant of the waveguide mode β and the length of the waveguide: $\phi(n_{bio}) = \beta(n_{bio}) \times l$. The importance of the waveguide structure for the phase sensitivity can thus be expressed as:

$$\frac{\partial\phi}{\partial n_{bio}} = \frac{\partial\beta}{\partial n_{bio}} \times l. \tag{3.4}$$

β, and also the loss α, depends on n_{bio} and the waveguide structure used. The three different structures we compare: a dielectric nanowire, a silver nanowire and a silver wedge waveguide are described in the next section.

3.3 WAVEGUIDE STRUCTURES

3.3.1 *Dielectric nanowire*

Fabrication techniques have made great progress to fabricate low-loss smooth dielectric nanowires with uniform diameters below the wavelength of the guided light [157]. Unlike optical fibres with larger diameters, a large portion of the light consists of evanescent fields in the surrounding medium [158], making them interesting structures for sensing applications. Figure 3.2 shows the mode shape of the single mode of a silica, $n = 1.4475$, dielectric fibre with a diameter of a 100 nm, surrounded by water. It clearly shows most of the light is outside of the fibre as evanescent fields, the width of the mode is many micrometers wide, in stark contrast to the plasmonic modes shown later. The diameter of a 100 nm was chosen to be able to compare results directly to the 100 nm wide silver nanowire, but it is important to note that a wavelength-to-diameter ratio of $\frac{810nm}{100nm} = 8.1$ is at the limit of what is possible, both experimentally and theoretically. This results in experimental propagation losses higher than the lossless case assumed here [157, 159]. The eigenvalue equation of the lowest order mode, LP_{01}, is given by

$$k_d r \frac{J_1(k_d r)}{J_0(k_d r)} - k_{clad} r \frac{K_1(k_{clad} r)}{K_0(k_{clad} r)} = 0, \tag{3.5}$$

with $k_d = k_0\sqrt{n_d^2 - (k/k_0)^2}$ and $k_{clad} = k_0\sqrt{(k/k_0)^2 - n_{clad}^2}$. n_d is the dielectric constant for the silica, i.e. 1.4475, and n_{clad} the refrac-

tive index of the surrounding medium, i.e. n_{bio}. Equation 3.5 can be solved for k numerically, which is the propagation constant in this lossless case.

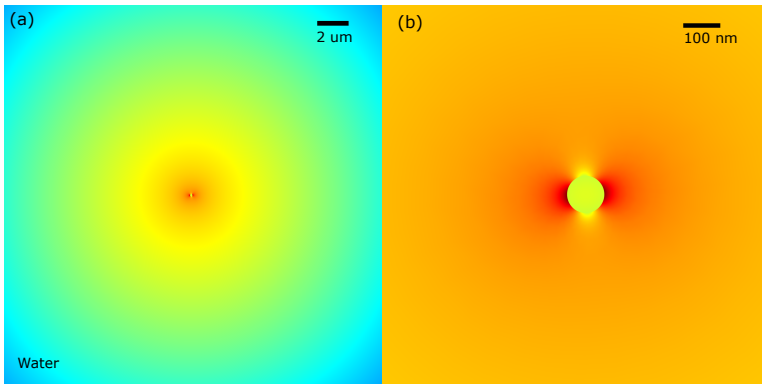


Figure 3.2: **a**, Electric field norm $|\mathbf{E}|$ of the only optical mode of a thin dielectric wire (diameter = 100 nm) in the middle, shown more in detail in **(b)**. The wire has a refractive index of 1.4475 and is surrounded by water, $n = 1.333$.

3.3.2 *Silver nanowire*

As explained in chapter 1, plasmonic waveguides can guide light below the diffraction limit. The smaller the silver nanowire, the smaller the lowest-order optical mode, shown in figure 3.3, will become; it shrinks instead of becoming more and more evanescent like the optical mode of the dielectric nanowire. For a fixed diameter, the mode also becomes more confined with a higher surrounding refractive index, the influence on the propagation loss of this is shown in figure 3.3 (b): the total transmission η decreases with increasing n_{bio} for a wire with fixed length of 4 μm. Also the silver nanowire has closed-form expressions for the modes, the eigenvalue equation for the TM mode is:

$$\frac{\epsilon_m}{k_m}\frac{I_1(k_m r)}{I_0(k_m r)} + \frac{\epsilon_{clad}}{k_{clad}}\frac{K_1(k_{clad} r)}{K_0(k_{clad} r)} = 0, \tag{3.6}$$

with $k_m = k_0\sqrt{(k/k_0)^2 - \epsilon_m(\omega)}$ and $\epsilon_m(\omega)$ the dielectric constant of the silver, taken from experimental values obtained by Rakic *et al.* [160].

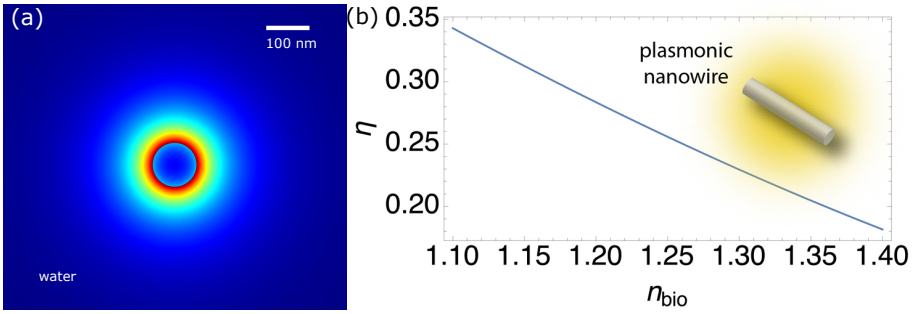


Figure 3.3: **(a)**, Electric field norm |E| for the TM_0 mode, the total transmission of this mode in function of the surrounding refractive index for a 4 µm wire is shown in **(b)**.

Figure 3.4 shows the difference in influence of n_{bio} on the propagation constant β of the dielectric and metal nanowire. The value is considerably higher for the silver nanowire, Chapter 1 explained this relation between high confinement and deviation from the light line. Unfortunately, this confinement comes with the price of high losses, with a propagation length that varies around 3 µm. The important value is of course $\frac{\partial \beta}{\partial n_{bio}}$, where the silver nanowire delivers an improvement of almost 40%.

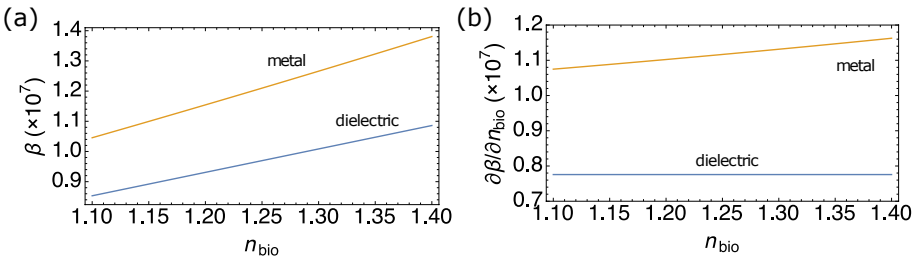


Figure 3.4: **(a)**, Propagation constant of silver and dielectric nanowire in function of the refractive index of the surrounding medium n_{bio}. **(b)**, Derivative of the propagation constant to n_{bio}, in function of the refractive index. The metal nanowire shows a stronger dependence on n_{bio} over the whole calculated range of n_{bio}.

3.3.3 *Wedge waveguide*

From studying the coupled modes on thin metal films, we know that the effective refractive index of the bound asymmetric mode is higher when the film is thinner. The smaller distance from face to face thus creates a higher refractive index for light coupled at the top of the wedge compared to light coupled lower down the structure, result-

ing in a vertical confinement of the plasmonic mode at the top [161]. These waveguide structures have been popular for some time due to their high confinement and reasonable propagation lengths [162]. Template stripping silver from etched silicon has recently been shown to produce high quality wedge waveguides, where the ultra-smooth surfaces deliver lower propagation losses than expected from simulations with the material properties of the silver taken from Rakic *et al.* [43, 86] There is no exact equation to obtain the propagation constant β and loss for wedge waveguides. Instead, a 2D finite element method (FEM) mode-solver simulation in COMSOL was done with n_{bio} as a changing parameter. The optical mode with $n_{bio} = 1.333$ and transmission for a changing n_{bio} is shown in figure 3.5. The dielectric constant $\epsilon_m(\omega)$ was taken from Rakic *et al.* [160] to make comparisons with the silver nanowire more straightforward, which makes this a more lossy structure than optimally possible. We did use the same top angle as obtained by silicon etching, being 70.6°, rounded with a realistic radius of curvature of 20 nm. The height of the wedge was taken 5 µm for robustness of the simulations, but the optical mode is highly confined and at optical wavelengths the structure can be made as small as 50 - 100 nm without considerable coupling to the base corners.

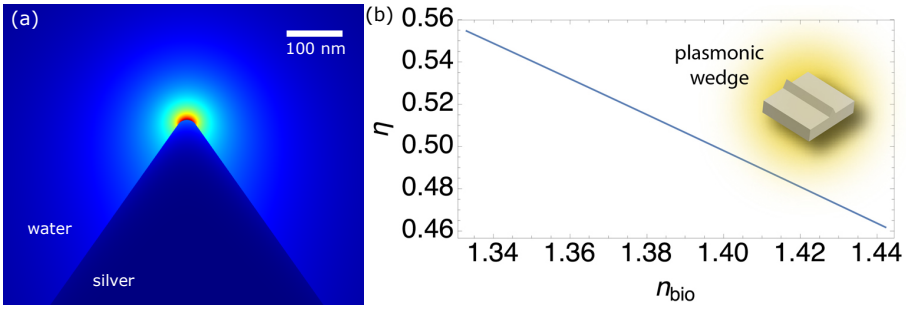


Figure 3.5: **(a)**, Electric field norm |E| for the TM mode, the total transmission of this mode in function of the surrounding refractive index for a 4 µm waveguide is shown in **(b)**.

3.4 QUANTUM METROLOGY

A typical example of a classical two-mode phase measurement is the measurement of the phase difference between the two arms of a Mach-Zehnder interferometer, typically with a coherent laser beam entering the interferometer at one of the two input modes of the first

beam splitter. A coherent beam can be expressed in the Fock basis $|m\rangle$ of the quantized field as [95]:

$$|\Psi_{in}\rangle = |\alpha\rangle = e^{-|\alpha|^2/2} \sum_{m=0}^{\infty} \frac{\alpha^m}{\sqrt{m!}} |m\rangle , \tag{3.7}$$

with a mean photon number $|\alpha|^2 = N$. When the other input port of the first beam splitter only contains the vacuum state, the output state of the two modes behind the second beam splitter becomes:

$$|\Psi_{out}\rangle = \left|\frac{1}{2}\alpha(e^{i\phi} - 1)\right\rangle \left|\frac{1}{2}i\alpha(e^{i\phi} + 1)\right\rangle . \tag{3.8}$$

An intensity-difference measurement, $\hat{M} = \hat{N}_1 - \hat{N}_2$, is performed at the two outputs of the second beam splitter; with output state $|\Psi_{out}\rangle$ the expectation value of that measurement is $\langle\hat{M}\rangle = M_0 cos\,(\phi(n_{bio}))$. With quantum techniques on the other hand, we can choose a NOON state generated at the source state of figure 3.1:

$$|\Psi_{in}\rangle = \frac{1}{\sqrt{2}}(|N0\rangle_{12} + |0N\rangle_{12}), \tag{3.9}$$

with N the number of photons in the state. Each photon in mode 1 accumulates a relative phase difference of ϕ resulting in a total phase shift of $N\phi$:

$$|\Psi_{out}\rangle = \frac{1}{\sqrt{2}} \left(\underbrace{e^{i\phi}...e^{i\phi}}_{\text{N times}} | \underbrace{1...1}_{\text{N times}} , \underbrace{0...0}_{\text{N times}} \rangle_{12} + |0...0, 1...1\rangle_{12} \right) \tag{3.10}$$

$$= \frac{1}{\sqrt{2}}(e^{iN\phi}\,|N0\rangle_{12} + |0N\rangle_{12}). \tag{3.11}$$

The optimal observable at the measurement stage is $\hat{A} = |0N\rangle\langle N0| + |N0\rangle\langle 0N|$, with an expectation value $\langle\hat{A}\rangle = A_0 cos(N\phi(n_{bio}))$. It is clear that $\langle\hat{A}\rangle$ oscillates N times faster than the classical $\langle\hat{M}\rangle$, a well-known effect called phase super-resolution [163, 164], and shown for the case of $N = 4$ in figure 3.6 (a). A small change in $\phi(n_{bio})$ clearly has a stronger effect on $\langle\hat{A}\rangle$ than on $\langle\hat{M}\rangle$ and we thus expect a smaller resolution δn_{bio} for the first; indeed, using equation 3.3 gives:

$$\delta\phi(n_{bio}) = \frac{(\langle\hat{M}^2\rangle - \langle\hat{M}\rangle^2)^{1/2}}{\left|\partial\hat{M}/\partial\phi(n_{bio})\right|} = \frac{1}{|\alpha|\,sin(\phi(n_{bio}))} \tag{3.12}$$

$$\delta\phi(n_{bio}) = \frac{(\langle\hat{A}^2\rangle - \langle\hat{A}\rangle^2)^{1/2}}{\left|\partial\hat{A}/\partial\phi(n_{bio})\right|} = \frac{1}{N}. \tag{3.13}$$

The Mach-Zehnder set-up can typically be positioned around $\phi = \frac{\pi}{2}$, the minimum resolution $\delta\phi$ in equation 3.12 then becomes $\delta\phi = \frac{1}{|\alpha|} = \frac{1}{\sqrt{N}}$, with N the mean photon number in the coherent state. This is indeed the SNL and is the optimal resolution for any classical approach. The NOON state on the other hand performs better with a resolution of $\delta\phi = \frac{1}{N}$, which is the Heisenberg limit. This is the optimal resolution for any approach. It is important to note that although useful to intuitively understand the effect, super-resolution of ϕ does not always imply super-sensitivity; super-resolution can be achieved with purely classical light with the right measurement set-up, but these approaches will not deliver super-sensitivity [155, 156]. The exact needed quantum resource to perform quantum-enhanced measurements in a general setting is still an open debate [154, 165].

Combined with the information of figure 3.4, we can now compare the classical and quantum approach for both the dielectric and silver nanowire, summarized in figure 3.6 (c). The expectation value of the measurement operator of the quantum approach oscillates faster in function of n_{bio} than the classical approach. This is true for both the dielectric and metal nanowire, due to the higher sensitivity to the induced change in ϕ. For both the classical and quantum approach the observable oscillates faster in function of n_{bio} for the plasmonic waveguide, due to the higher value for $\frac{\partial\beta}{\partial n_{bio}}$ shown before. The resulting resolutions are shown in figure 3.6 (d), the plasmonic quantum approach delivers a substantial improvement over the dielectric quantum and plasmonic classical approaches. Unfortunately, NOON states are very sensitive to loss, even the loss of a single photon destroys any phase information in the state as it collapses into a product of two Fock states $|N-1,0\rangle$. This means that other states have to be considered to obtain an improvement in realistic scenarios.

Several attempts have been made to find path-entangled number states that are robust in the presence of loss [166, 167]. We will calculate the optimal state present in a given amount of loss, taken from the transmission η from the waveguides, and assume the optimal measurement is performed. The resolution is then given by the quantum Cramer-Rao bound [154]:

$$\delta\phi \geqslant F_Q^{-1/2}. \tag{3.14}$$

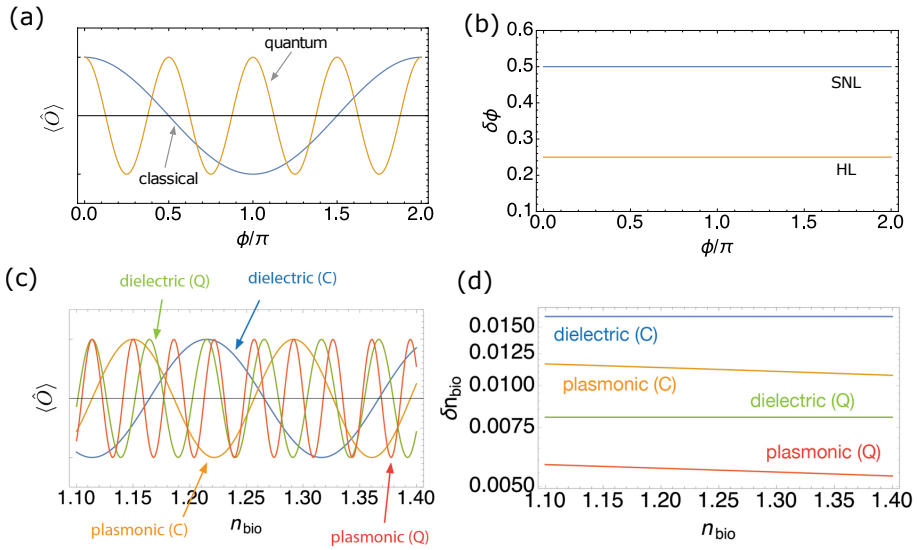


Figure 3.6: **(a)**, Comparison of quantum and classical metrology by comparing expectation values $\langle \hat{A} \rangle$ and $\langle \hat{M} \rangle$, the first one oscillates 4 times faster in function of $\phi(n_{bio})$. **(b)**, The Heisenberg and shot-noise limit for a 4-photon state. **(c)**, Oscillations of the expectation value of the measurement operator, $\langle \hat{O} \rangle$, by the change of n_{bio} for the four different combinations of dielectric or plasmonic waveguide and classical or quantum measurement approach. **(d)**, Minimum resolution δn_{bio} for these four approaches over the range of n_{bio}.

F_Q is the quantum Fisher information:

$$F_Q[\rho_\phi] = \mathrm{Tr}\left[\rho_\phi L\left[\rho_\phi\right]^2\right]. \tag{3.15}$$

$L\left[\rho_\phi\right]$ is the Symmetric Logarithmic Derivative, which can defined by $\frac{\partial \rho_\phi}{\partial \rho} = \frac{1}{2}\left(\rho_\phi L\left[\rho_\phi\right] + L\left[\rho_\phi\right]\rho_\phi\right)$. The quantum Fisher information (QFI) is a natural extension of the Fisher information in statistics, given by $F\left[p_\phi\right] = \left\langle\left(\frac{\partial}{\partial\phi}\ln(p_\phi)\right)^2\right\rangle$, with $p_\phi(X)$ a probability density function with parameter ϕ, and is a measure to quantify the amount of information variable X modelled by a distribution $p_\phi(X)$ contains about ϕ. The more information about ϕ is contained in the state, the higher the resolution of the estimate of ϕ can be, as shown in equation 3.14. It has been shown that the projective measurement on the eigenbasis of $L\left[\rho_\phi\right]$ saturates the Cramer-Rao bound, obtaining the minimum resolution $\delta\phi = F_Q^{-1/2}$ for a given state is thus always theoretically possible [154, 168].

Quantum states with a definite number of N photons will be used in the following results, the general description of these states is given by:

$$|\Psi_{in}\rangle = \sum_{n=0}^{N} c_n |n, N-n\rangle. \tag{3.16}$$

The defining coefficients c_n of these states can be optimized so that F_Q is maximized. For the situation depicted in figure 3.1 with only loss in one mode, F_Q can be calculated as [169]

$$F_Q = 4\left(\sum_{k=0}^{N} k^2 x_k - \sum_{l=0}^{N} \frac{\left(\sum_{k=l}^{N} x_k k B_l^k\right)^2}{\sum_{k=l}^{N} x_k B_l^k}\right), \tag{3.17}$$

with $x_k = |c_k|^2$ and $B_l^k = \binom{k}{l}\eta^k\left(\eta^{-1}-1\right)^l$. For the following results, it is this function that will be maximized for a chosen number of photons N and an amount of loss $(1-\eta)$ given by the plasmonic waveguide. Of course, photon loss also has an influence on the classical measurement precision. For the case of $(1-\eta)$ loss in one arm, the phase sensitivity can be optimized by using unbalanced beam splitters in the Mach-Zehnder configuration, resulting in a standard interferometric limit (SIL) [170]:

$$\delta\phi = \frac{1+\sqrt{\eta}}{2\sqrt{N\eta}}, \tag{3.18}$$

which, as expected, is inversely proportional to the square root of the average amount of transmitted photons ηN, but performs a factor $\frac{1+\sqrt{\eta}}{2}$ better than the SNL in the non-optimized case.

3.5 RESULTS

We can now combine the transmissivity coefficients η shown in figures 3.3 and 3.5 with the optimized quantum Fischer information given in equation 3.17. Figures 3.7 (a) and (b) show the minimum resolution δn_{bio} for the silver nanowire and wedge waveguide with lengths $l = 4$ µm and photon number $N = 4$. The latter is chosen with current experimental progress in quantum optics research in mind [171, 172]. The optimal state is located in the shaded area between the SIL and the HL, showing that a improvement in sensitivity is possible, even when realistic losses are included. This is the case over the whole range of n_{bio}. The NOON state, on the other hand, always performs worse than the classical limit for the whole n_{bio} range. Combining the popular NOON-state based quantum metrology with lossy plasmonic structures does not create an improved resolution. It is worth noting that the optimal quantum state with the plasmonic waveguide does not achieve a better resolution δn_{bio} than the NOON state for the assumed lossless dielectric wire, for which the resolution is shown in figure 3.6. This does not mean the dielectric nanowire is always the best strategy; the large mode-size of the dielectric wire prohibits this method for use on scales below the operating wavelength. On top of that, as mentioned before, the dielectric case would also not be lossless experimentally, especially with a extremely narrow nanowire with a diameter of a 100 nm. The diameter of the nanowire influences the fraction of the light that travels outside of the wire as evanescent fields, and thus the sensitivity of the mode to changes in the surrounding refractive index. One could thus also investigate the trade-off between propagation/coupling losses and phase-sensitivity for the dielectric case. Figures 3.7 (c) and (d) show the performance of the optimal state and NOON state for increasing N with the silver and wedge waveguide. It is possible to construct a state that performs better than the SIL for any N, which with current technology becomes increasingly hard for larger N. Considering the high losses, it can become more efficient to send more identical states with a lower photon number N, resulting in the same total amount

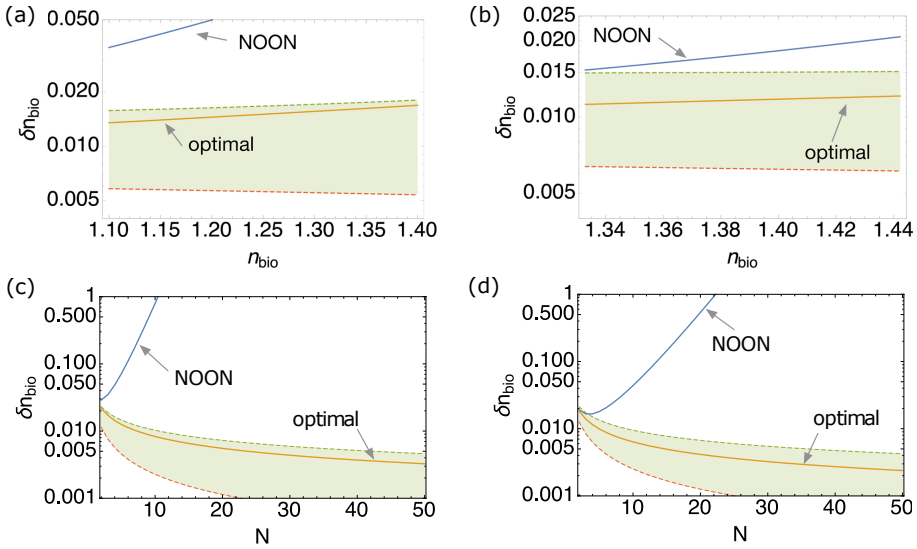


Figure 3.7: **(a)**, The minimum resolution calculated with the Cramer-Rao bound for the NOON state and the optimal state for $N = 4$ for calculated transmissivities η ($l = 4\mu m$) over the range of n_{bio} for the silver nanowire and **(b)** wedge waveguide. **(c)**, The minimum resolution for the NOON state and the optimal state for varying N with $n_{bio} = 1.1$ for the silver nanowire and **(d)** $n_{bio} = 1.333$ for the wedge waveguide. The shaded areas in all images are bounded by the SIL at the top and the HL at the bottom.

of photons, the so-called chopping strategy [168]. The NOON state deviates strongly from the SIL for high N, which is not surprising, the chance that the intact state makes it to the measurement stage is $\frac{\eta^N}{2}$.

The coefficients $\{x_n\}$ for the silver nanowire and wedge are shown in figure 3.8 (a) and (b) respectively, for N = 4. The changing transmission η in function of n_{bio} clearly has an influence on the optimal state, the coefficients change considerably over the range of n_{bio}. From a practical point of view, it is undesirable that the needed optical state depends on the unknown quantity of interest. It is thus interesting to see how sensitive the resolution of an optimal state for a certain n_{bio} is to (small) changes in this quantity. We took the optimal state for three different values of n_{bio}, labelled by (1), (2) and (3) in figure 3.8 (a) and (b), and calculated their minimum resolution over the whole range of n_{bio}, shown in 3.8 (c) and (d) for the nanowire and wedge waveguide respectively. The states are shown to be reasonably robust against changes in the refractive index, one fixed state could

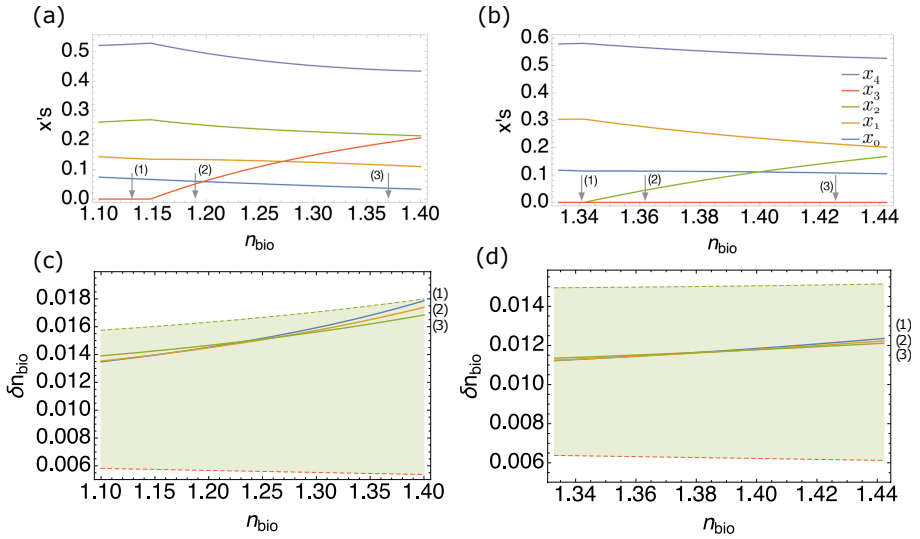


Figure 3.8: The coefficients $\{x_n\}$ of the optimal states for the silver nanowire in **(a)** and wedge waveguide in **(b)**, transmissivities η again the same as in figures 3.3 and 3.5. The minimum resolutions over the whole range of n_{bio} of the states (1), (2) and (3) labelled in **(a)** and **(b)** for **(c)** and **(d)** respectively.

be chosen, optimized for the middle of the experimental region of n_{bio} for example, and used to deliver phase measurements below the SIL over the whole range of n_{bio}. This clearly makes the use of these states for plasmonic sensing applications more straightforward, although a feedback mechanism could probably be used to optimize the state throughout measurements.

3.6 OUTLOOK

In this chapter, we have investigated the possibility of combining the already established technique of plasmonic sensing with the rapidly expanding research on quantum-enhanced measurement schemes. The rather general approach of using a two-mode definite-photon state was combined with 2 specific plasmonic waveguide structures which induce a phase-shift dependent on the surrounding medium of interest. With these structures it was shown that in theory a range of quantum states could enhance sensitivity of the phase measurements. Of course, a different waveguide structure would need its own investigation, but the results presented here can be seen as a first step in the di-

rection of exploring quantum plasmonic sensing. This will also have to include losses due to the coupling into and out of the waveguides, which were not taken into account in the calculations performed here. These discrete steps of loss are highly dependent on the used scheme and would make the analysis overly complicated. It is clear that the success of quantum plasmonic metrology, and many other plasmonic applications, will depend on the development and fabrication of efficient structures, especially in terms of photon-SPP coupling. Research in the integration of plasmonic waveguides with silicon photonics and efficient coupling between dielectric and plasmonic waveguides shows promising results, summarized in chapter 1. This would allow plasmonic sensing to benefit from the rapid progress in silicon quantum photonics [22, 173]. On the out-coupling side, a full integration with near-field detectors would, see chapter 2, also minimize losses.

Two main directions can be persued from here for more theoretical and experimental research. First, a closer connection with current plasmonic sensing techniques can be made, as many plasmonic sensors often use an altogether different approach than the waveguide based phase measurements analyzed here. For a transformation of the analysis to a different setting one just has to find the correct parameter X to express the sensitivity in: $S = \frac{\partial\langle\hat{O}\rangle}{\partial X}\frac{\partial X}{\partial n_{bio}}$, the minimum resolution would become $\delta n_{bio} = \delta X \left|\frac{\partial X}{\partial n_{bio}}\right|^{-1}$, with $\delta X = \Delta\hat{O}/\left|\partial\left\langle\hat{O}\right\rangle/\partial X\right|$. For the well-established Kretschmann configuration plasmon resonance sensor for example, the reflection coefficient $|R|^2$ would have to be used as the parameter X. One could also consider the phase-sensitive implementation of the Kretschmann configuration; the sensor is well-established and highly sensitive and the two-mode phase-sensitive configuration makes it the obvious next step from the work presented here [151, 152]. The implementation of this set-up is depicted in figure 3.9, the excitation of SPPs through the prism not only creates a modulation in the reflected intensity of the light, but also results in a phase shift highly sensitive on the refractive index of the medium behind the gold layer. This phase shift is measured with photodetectors behind the Mach-Zehnder interferometer. Advanced implementation of this basic scheme to minimize noise have already achieved sensitivities close to the SNL, a quantum metrology implementation would thus be a desirable next step [174].

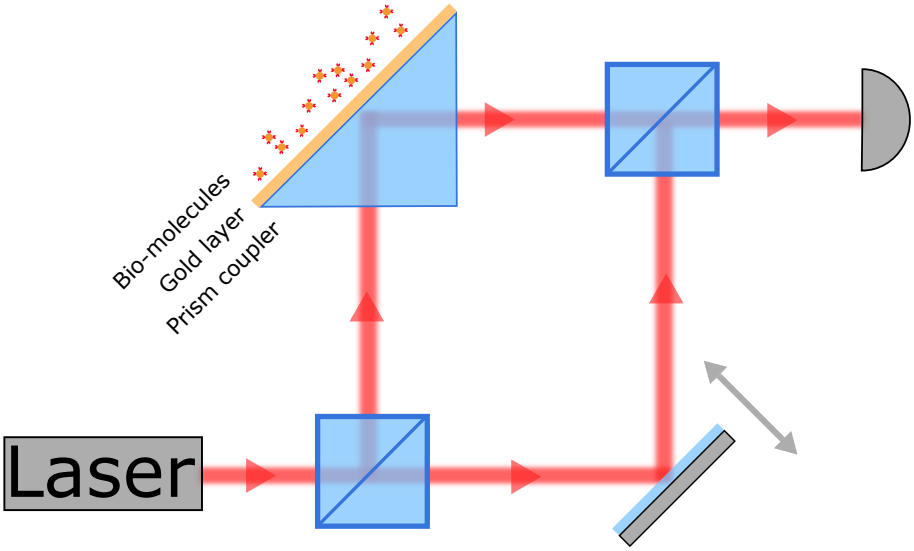


Figure 3.9: Schematic depiction of a Mach-Zehnder based phase-sensitive surface plasmon resonance sensor.

The analysis here was performed with quantum states that only contain a low number of photons. Considering the $\frac{1}{\sqrt{N}}$ scaling of the SNL, obtaining quantum improvements with high intensity states would be desirable for systems that do not impose experimental limits on the optical power. The first formal proposal of quantum metrology involved the combination of a coherent laser beam with a squeezed vacuum state at the two input ports of a Michelson interferometer. It is with this approach the most tantalizing use of quantum metrology has been shown: enhanced sensitivity of the LIGO gravitational wave detector [13, 175, 176]. The experimental advantage of using a laser source is clear, it provides the ability to generate photon numbers many orders of magnitude higher than the exotic states used here. Also for these quantum states interest in the influence of loss on the measurement performance has grown recently [154, 177]. The growing understanding on the general framework of lossy quantum metrology [178], together with a rapid technological progress, makes it the right time to envision and investigate potential ways of improving plasmonic sensing techniques with quantum technologies.

4

QUANTUM INTERFERENCE

The two photon quantum interference experiment with Surface Plasmon Polaritons was reported by us [1] and several other groups in a short period of time in 2013-2014 [33–36]. We were the only group that used a scattering-based beam splitter, offering an interaction length of less than two wavelengths, but with an added loss channel in the form of scattering into free space. Subsection 4.1 goes through the efforts to characterize the sample. After our publication, it was decided to rebuild the set-up to obtain stronger results and better insights into them. The rebuilt set-up and the final results are explained in subsections 4.2 and 4.3 respectively.

4.1 SAMPLE

A scattering based plasmonic beam splitter, a 3D sketch and an optical picture, taken with the set-up depicted in figure 4.2 (a), are shown in figure 4.1. Two gold plasmonic stripe waveguides (2 µm wide and 70 nm thick) cross perpendicularly halfway. Rectangular ridges acting as a Bragg reflector were patterned on top of the crossing point to mix the light coming from one input into both outputs. To overcome the phase mismatch between photons and SPPs and couple the light into and out of the waveguides, gratings consisting of rectangular ridges were patterned at the four ends of the waveguides. Beam splitters with a range of parameters were fabricated during the PhD of Giuliana DiMartino [40]. The period of the coupling gratings range from 540 to 700 nm in steps of 40 nm, with the ridges always 90 nm high and a width half of the period (270 to 350 nm). All gratings have 11 ridges. The Bragg reflectors consist of 2, 3 or 4 rectangular ridges, 90 nm high and a 150 nm wide, spaced with a 500, 550 or 600 nm period. The total of 45 different combinations (5x3x3) were experimentally characterized by Dr. DiMartino and myself to chose the structure with the best optical behaviour, i.e. efficient in- and out-coupling at the wavelength of interest (808 $\pm$10 nm) and 50/50 splitting of the Bragg reflector. For our first publication [1], grating couplers with a

period of 620 nm and a Bragg reflector with 3 ridges and a period of 500 nm were chosen. A summary of the characterization results from the measurements performed before the first publication are extended and compared with new results in the following subsections. These results made us change to grating couplers with a period of 580 nm, phase measurements on the Bragg reflector also gave us more insight on the lack of perfect visibility of the quantum interference. A more complete analysis of the influence of the wavelength and all of the sample feature variations on the optical properties of the structures can be found in Dr. DiMartino's PhD thesis [40] and my Master thesis [179].

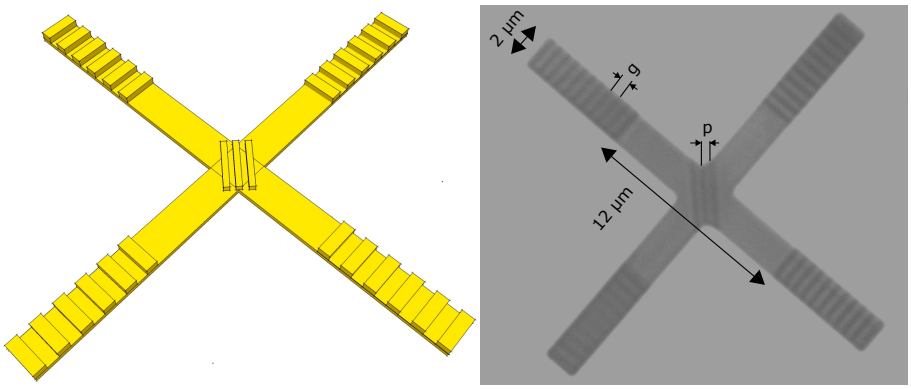


Figure 4.1: 3D sketch left and right optical picture of a beam splitter sample, taken with set-up depicted in figure 4.2 (a). All the fabricated beam splitters had 2 µm wide and 12 µm long waveguides. Beam splitters were made with a variation in the periodicity g of the coupling gratings (540, 580, 620, 660 and 700 nm). The central Bragg reflector varied with 2, 3 or 4 ridges and with a spacing p of 500, 550 and 600 nm.

4.1.1 *Fabrication*

The structures were fabricated by two step Electron Beam Lithography (EBL). The first step patterned the waveguides on the glass substrate, while the second step created the grating couplers and the Bragg reflectors on top. In both steps a 300 nm thick film of PMMA is used as a positive tone resist, the exposed parts are developed by a mixture of methyl isobutyl ketone and isopropanol (3:1). In the first step, the open areas of the substrate are covered with a self-assembled monolayer of (3-marcaptopropyl)trimethoxysilane before depositing the gold by thermal evaporation. This assures a good adhesion be-

tween the glass and the gold, with a smaller influence on the optical properties of the plasmonic waveguide compared to other common binding layers as Titanium or Chromium [180]. After the gold deposition the rest of the resist is removed by acetone. With the exception of drop casting the self-assembled monolayer, the same steps are taken for the second writing step. Careful alignment with the waveguides created in the first step is obviously crucial to position the grating couplers and Bragg reflectors at the right position.

4.1.2 *Stripe waveguides*

Previous research has shown that thin stripe waveguides support quasi-TM modes at both wide interfaces, the number depending on the width of the waveguide. The gold-glass interface sustains bound modes, while at the gold-air interface there are only leaky modes [181]. The thickness of the waveguide (70 nm) makes sure this leakage only has a small influence on the total loss of the propagating mode. An approximate analytical ray optics model, similar to a dielectric slab waveguide, can be used to derive the following relation [182]:

$$N < \frac{2W}{\lambda}\sqrt{\frac{-\epsilon_d^2}{\epsilon_d + \epsilon_m}}, \tag{4.1}$$

with W the width of the waveguide and N the number of modes. Plugging in the values for the relative permittivity of gold ($\epsilon_m = -25.8$ [183]) and air ($\epsilon_d = 1$), gives one leaky mode. By using the value for glass ($\epsilon_d = 2.25$), we see that there are also 2 potential bound modes at the gold-glass interface. An experimental value of the propagation length of 12.4 ± 0.3 μm was obtained with the cut-back method [184]. This method estimates the propagation length by measuring the output intensity of waveguides of of varying length with equal input intensity, while the input and output coupling efficiencies are assumed to be constant. A single-mode pigtailed diode laser [LM9LP, Thorlabs] with a wavelength of 785 nm was used to consecutively excite the inputs of waveguides from 7.5 μm up to 27.5 μm in steps of 2.5 μm. Every time a picture was taken with the camera, without back illumination. The intensity values of the pixels corresponding to the output gratings were summed in post-processing to obtain a total output intensity, which are the data points in figure 4.2 (c). Fitting an

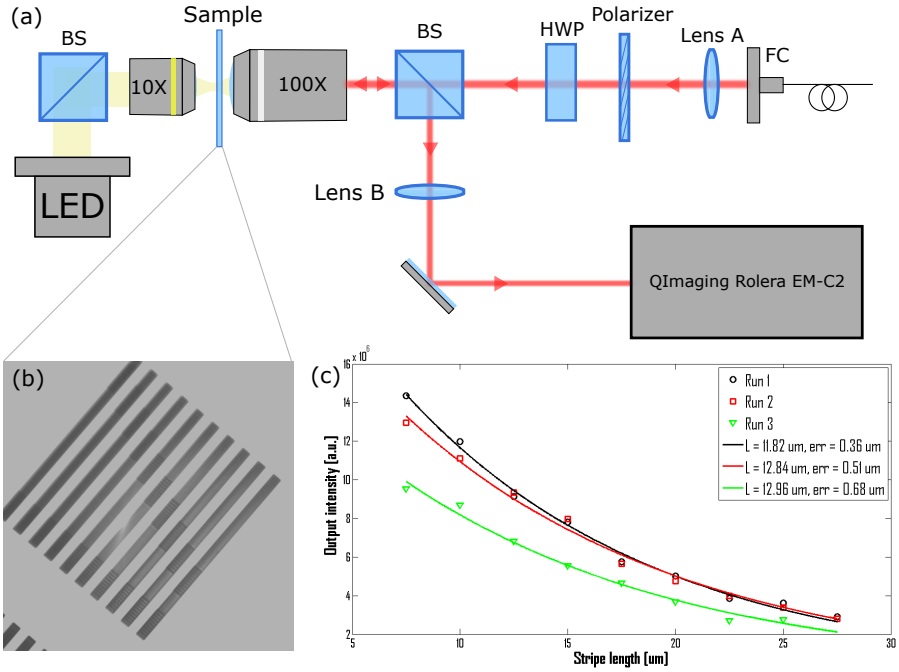


Figure 4.2: **(a)**, Schematic drawing of the optical set-up. Lens A (f = 25 mm) collimates the light coming from the fibre coupler towards the 100x objective [Olympus LMPlan IR]. Light scattered out of the structures is collected with the same objective and directed to the camera [QImaging Rolera EM-C2], with tube lens B (f = 300 mm). The LED in combination with the 10x objective provides backside illumination. **(b)**, Optical picture of the waveguides used in the cut-back measurement. Grating to grating lengths ranging from 5 µm to 27.5 µm in steps of 2.5 µm. **(c)**, Data points and exponential fits from three different measurement runs.

exponential function to the data points gives an estimate of the propagation length. The obtained value agrees well with the numerical value of 11.7 µm for the leaky mode given by COMSOL mode-solver. Figure 4.3 shows the strong confinement at the gold-air interface of the mode with some leakage into the glass substrate. To further test we are exciting the SPP modes of the waveguides, the polarization of the input light was changed from TM to TE and a strong suppression of the output intensity was measured, as expected. COMSOL also finds three bound modes, in reasonable agreement with the 2.5 obtained from equation 4.1. We assume these bound modes to have only a small influence on our experiments, as the excitation gratings are positioned at the gold-air interface, thus preferentially exciting the leaky mode [185].

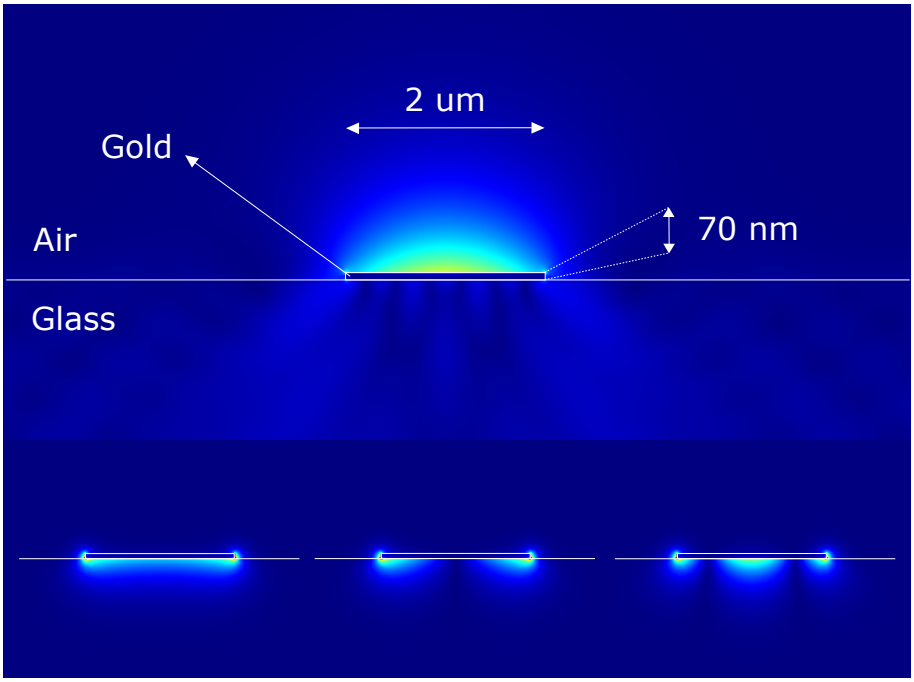


Figure 4.3: The top image shows the leaky mode at the gold-air interface, obtained with COMSOL 2D mode solver. Bottom three images are the bound modes at the gold-glass interface.

4.1.3 *Grating couplers*

As explained before, grating scattering is one of the most common used techniques to alleviate the difference in momentum between a photon and SPP. Gratings have the advantage of being highly localized, SPPs can be excited by a focused beam with a position accuracy of the diffraction limit. Out of convenience we restate the formula for a small sinusoidal modulation [49], explained in section 1.2.2:

$$k_{SPP} = \pm k_0 \sin(\theta) \pm nK. \tag{4.2}$$

The grating adds momentum in multiples of the grating Bragg wave vector $K = \frac{2\pi}{L}$, with L being the period of the grating. This makes it straight-forward to see that for a perpendicular incident plane wave the period of the grating has to match the wavelength of the SPPs.

Considering the shape and height of our ridges, we can expect a considerable deviation from this formula in terms of higher order K-values and dispersion curve of the SPPs. In the quantum experiments the gratings were illuminated with a focused spot of approximately 1-2 μm. We've looked at numerous publications that study

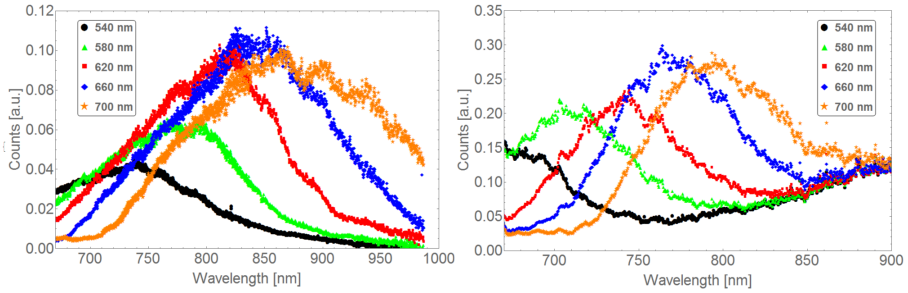


Figure 4.4: Spectra (normalized by the spectrum of the source) of the light measured at the output grating, with both in- and output grating 540, 580, 620, 660 or 700 nm. Left, input gratings illuminated with large spot coming from a OceanOptics HL2000 white light source. Right, input gratings illuminated with focused broadband laser spot.

the influence of the different grating parameters on the efficiency of excitation in section 1.2.2. Unfortunately no studies have been found on the influence of the spot size with a grating of fixed size. The spectrum of the excited SPPs for gratings with different periods (but always 11 ridges, a ridge height of 90 nm and a duty-cycle of 0.5) was measured by illuminating the input gratings of 10 µm long waveguides and measuring the light scattered at the output gratings with a spectrometer. The difference between excitation with a large (~ 10 µm) and small illumination spot (1-2 µm) spot is shown in figure 4.4. There is a clear blue-shift going from the input spot covering most of the grating to the small spot, the excitation also becomes more narrowband. This is rather counter-intuitive, as a grating with less elements normally has a broader resonance. The larger range of angles involved in the tighter focus could be an explanation for this more selective excitation. Overall, studying these lossy gratings is a complex problem with the interplay of the scattering properties of the single ridges and the influence of the parameters of the grating itself. The spectral measurements with the large spot excitation were the reason the 620 nm period gratings were chosen for the first quantum interference experiments, as they peak around 800 nm. The difference with the smaller spot excitation shows that these measurements are in fact not representative for the setting the structure will be used in. The second measurements show that none of the gratings have their resonance at 808 nm, fortunately the angle of incidence of the light is another free parameter to optimize the throughput of the waveguides with. Excitation at non-perpendicular incidence also breaks the

symmetry and it can be expected that a higher percentage of forward scattering can be obtained, thus improving the overall efficiency. As a complete study with numerical simulations is outside of the goal of this work, it was decided to optimise the input angle for each of the 5 grating periodicities and select the one with the highest efficiency. The new period of choice for the future experiments became 580 nm. We confirmed that the resonance was indeed centred around 808 nm at the optimized angle, figure 4.5.

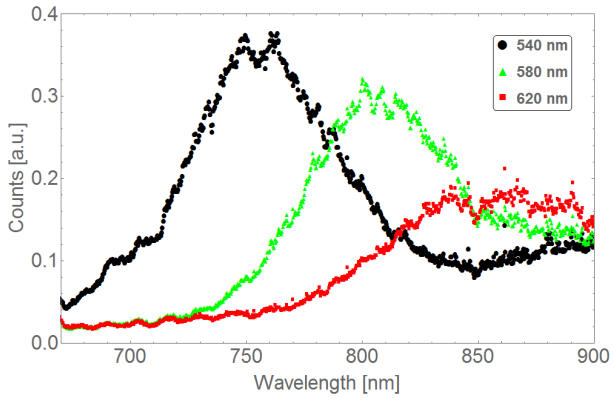


Figure 4.5: Spectrum obtained from illuminating gratings of 540, 580, 620 nm periodicity. The input angle was optimized for the 580 nm grating and has a resonance peak around 800 nm as expected. The 540 nm and 620 nm gratings deliver a blue- and red-shift respectively when excited at the same angle.

4.1.4 *Bragg reflectors*

SPPs are highly confined to the metal surface and thus sensitive to perturbations of this surface. The influence of surface roughness on both the dispersion curve and radiation losses of the SPPs were already well-studied decades ago [186] and are still of prime interest today [43], as we've also seen in chapter 1. It is not surprising the idea of using purposely patterned surfaces to introduce functionalities quickly found its way into the plasmonics community as a tool to achieve integrated photonics goals. Rows of circular perturbations of several 10s of nm on a silver surface was one of the first successful experimental demonstrations of creating basic optical elements like mirrors and beam splitters [187–189]. It was shown that incoming SPPs could be deflected efficiently, without too much scattering losses into free space. Subsequently, a lot of research was conducted into other

(semi-transparent) mirror structures like gratings of grooves [190] and ridges [191, 192]. Most of these structures were patterned or simulated on two-dimensional silver or gold films instead of on the crossing of two waveguides to serve as a waveguide beam splitter, as we need for our Hong-Ou-Mandel experiment. Some publications studied the reflection efficiency of patterned structures on a single waveguide, with the light thus at normal incidence of the structure [82, 190, 193]. To our knowledge only one publication reported on the use of a grating to reflect SPPs in a waveguide structure at non-normal incidence [194]. They used a grating of rectangular ridges similar to ours to guide SPPs around a 90° bent in a stripe waveguide, and to split a single input stripe into two perpendicular output stripes. Our structure is thus an extension of this idea to two input waveguides.

The ridges on the waveguide crossing can be considered a Bragg reflector, the basic formula for the resonance wavelength of such structure is given by [194]

$$\lambda = 2p\cos(\alpha_{inc}), \tag{4.3}$$

with p the period of the grating and α_{inc} the angle between the SPP mode and the normal on the grating. With formula 4.3 in mind, the spacings p of 500, 550 and 600 nm should deliver resonance wavelengths of 707, 779 and 849 nm respectively, around our wavelength of interest. Broadband measurements (from 600 to 900 nm) showed no clear resonance peaks for the structures [40, 179], which could be expected from the small number of ridges and the high losses in a plasmonic system. The scattering into free space did noticeably increase at shorter wavelengths, but fortunately optical images showed only a small amount of scattering ($<$ 10% compared to the scattering at the output gratings) at 808 nm. Set-up shown in figure 4.2 (a) was used to calculate the reflection and transmission coefficients of each beam splitter, the results are shown in table 1 [40, 179]. Making several measurements of the most promising beam splitter (3 ridges, 500 nm spacing) gave an average reflectivity of 0.51 $\pm$0.05.

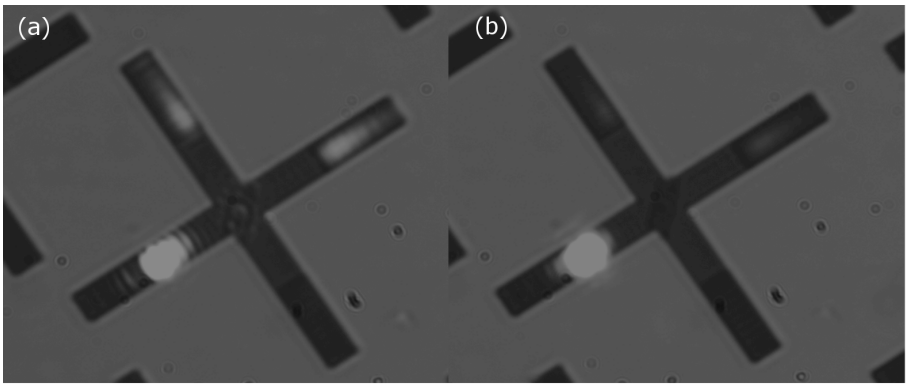


Figure 4.6: Excitation of the beam splitter structure with laser light with **(a)** TM and **(b)** TE polarization. The strong suppression of light scattered out at the two top gratings in picture (b) shows that the laser light excites a SPP mode of the waveguide. Optical images without background illumination were used to calculate the relative reflection and transmission coefficients.

# ridges	spacing [nm]	T1	R1	T2	R2
0		1	0		
2	500	0.74	0.26	0.75	0.25
	550	0.73	0.27	0.78	0.22
	600	0.78	0.22	0.79	0.21
3	500	0.53	0.47	0.55	0.45
	550	0.55	0.45	0.57	0.43
	600	0.63	0.37	0.63	0.37
4	500	0.35	0.65	0.40	0.6
	550	0.38	0.62	0.45	0.56
	600	0.64	0.36	0.58	0.42

Table 1: Splitting ratios of the different structures, normalized by dividing by (R + T)

In addition to the contribution to losses, light scattered into free space at the Bragg reflector is important as it creates an extra in-/output port, potentially changing the phase relationship between r and t [195]. In fact, any loss channel (including absorption) can change the phase relationship, as the transformation between in- and output modes does not need to be unitary any more [99]. Since this has an influence on the visibility of the HOM interference, we decided

to measure the phase difference ϕ_{r-t}between r and t in our preferred beam splitter structure. This was done with a Mach-Zehnder interferometer going from a photonic beam splitter (BS1) to the plasmonic one, depicted in figure 4.7 (a). A 808 nm diode laser was connected into a collimator (RC1). Scanning delay-line 2 between the two beam splitters while recording the counts collected by the two APDs allowed us to measure the phase difference. We can relate the output intensity at the outputs of the second beam splitter with the input state at the first beam splitter (see Loudon's *The Quantum Theory of Light* [196]) as:

$$\langle \hat{n}_3 \rangle = |R_{MZ}|^2 \langle \hat{n}_1 \rangle \text{, with } R_{MZ} = R_1 R_2 e^{ikz2} + T_1 T_2 e^{ikz1} \quad (4.4)$$

$$\langle \hat{n}_4 \rangle = |T_{MZ}|^2 \langle \hat{n}_1 \rangle \text{, with } T_{MZ} = R_1 T_2 e^{ikz2} + T_1 R_2 e^{ikz1} \quad (4.5)$$

R_{MZ} and T_{MZ} are thus the reflection and transmission amplitudes of the total MZ interferometer as a function of the reflection and transmission amplitudes of both the first and the second beam splitter and the path difference in the interferometer. The first beam splitter is assumed to be a unitary 50/50 beam splitter ($R_1 = \frac{1}{\sqrt{2}} e^{i\pi/2}$, $T_1 = \frac{1}{\sqrt{2}}$), the plasmonic beam splitter is given a unknown phase difference between R and T ($R_2 = \frac{1}{\sqrt{2}} e^{i\phi_{r-t}}$, $T_2 = \frac{1}{\sqrt{2}}$). Plugging all these relations into equations 4.5 and fitting them to the measured data, we can extract the phase shift in the second beam splitter as 1.21 ± 0.01, clearly deviating from the standard $\frac{\pi}{2}$ phase shift. This is also visible in figure 4.7, the two output intensities are not perfectly out of phase as normally expected, a $\frac{\pi}{2}$ phase shift in the amplitudes delivers a π phase difference between the measured intensities. Interestingly, among the many publications on different designs of scattering based plasmonic beam splitters or reflectors, none of the previously cited mention the potential loss of the unitary input - output relations. One numerical study of a chain of spherical perturbations on a gold substrate did show an influence of the size of the perturbations on ϕ_{r-t}, but did not contain an in-depth analysis of the effect [197].

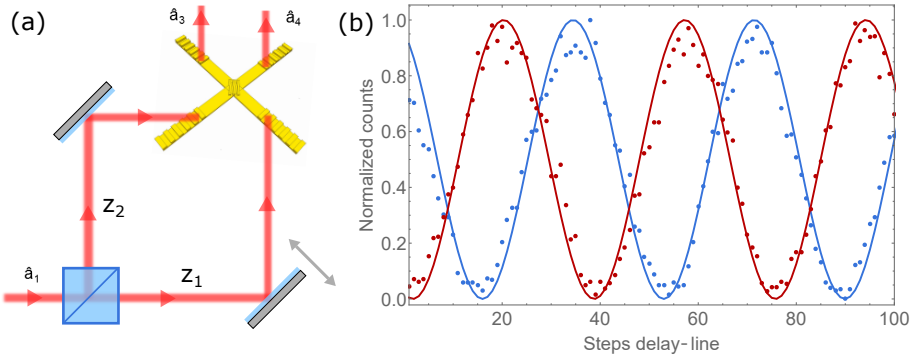


Figure 4.7: **a,** Schematic drawing of the set-up, laser light was inserted in input 1, light coming out of the plasmonic beam splitter at output 3 and 4 were measured with separate APDs. **b,** Signal of both APDs in function of the delay line in path z_1.

4.2 EXPERIMENTAL SET-UP

4.2.1 *Spontaneous parametric down-conversion*

Spontaneous parametric down-conversion is a three-wave mixing process in which a pump laser at frequency ω_0 generates two photons at frequencies ω_1 and ω_2. It is a parametric process, so the total energy and momentum have to be conserved:

$$\omega_0 = \omega_1 + \omega_2 \tag{4.6}$$

$$\mathbf{k}_0 = \mathbf{k}_1 + \mathbf{k}_2 \tag{4.7}$$

Due to the need for indistinguishable photons, the set-up is built at the degenerate point: $\omega_1 = \omega_2$. It is important to note that there is no seeding laser at the down-converted frequencies, a quantum treatment of the down-converted modes is needed to explain the generation of photon pairs out of vacuum fields. The interaction Hamiltonian can be written as:

$$\hat{H}_I = \hbar g(\hat{a}_1^\dagger \hat{a}_2^\dagger \hat{a}_0 + \hat{a}_1 \hat{a}_2 \hat{a}_0^\dagger) \tag{4.8}$$

With g a coupling constant linearly dependent on the second-order nonlinear susceptibility $\chi^{(2)}$ of the crystal [88]. Starting from an initial

state with only photons in the pump mode, $|\Psi(t=0)\rangle = |0,0,N_0\rangle$, the output state after interaction time L/c becomes:

$$|\Psi(t=L/c)\rangle = e^{-it\hat{H}_I/\hbar}\,|00N_0\rangle \tag{4.9}$$

$$\begin{aligned} &\approx (1-\mu^2/2)\,|0,0,N_0\rangle - i\mu\,|1,1,N_0-1\rangle \\ &\quad - \mu^2/2\,|2,2,N_0-2\rangle \end{aligned} \tag{4.10}$$

With $\mu = g\sqrt{N_0}L/c$ and the second line a second order approximation. When μ is sufficiently small to ignore the second order term, the process reliably generates photons in pairs [198].

To achieve the phase matching condition in equation 4.7, a birefringent crystal must be used to compensate for dispersion between the pump beam and the down-converted photons ($n_0 \neq n_{1,2}$). In so-called type I SPDC, the pump beam is polarized along one axis of the birefringent crystal (typically the extra-ordinary) and the down-converted photons have the same polarization to each other, but perpendicular to the pump polarization. We use a 5 mm long biaxial BiBO crystal [Newlight Photonics Inc.] that has its faces cut in specific angles in relation with the optical axes, so that -for the degenerate case- the momentum is conserved for down-converted photons in a cone with a 3° half angle around the pump beam, a schematic drawing of our set-up is shown in figure 4.8. It is crucial to align the fibre launchers correctly for collecting light coming out at exactly 3°. Furthermore, to efficiently collect photons from the same pairs, rather than single photons from uncorrelated pairs, the light must be collected from antipodal points of the cone. This means that the pump beam and the two collected modes have to be in one plane. The optical alignment is done by first sending laser light at 808 nm in the opposite direction, from the fibres to the crystal. This allows to visually align the set-up up to reasonable accuracy, after which optimization is done by maximizing the amount of detected photon pairs with the APDs and photon correlation equipment. Many iterations between the tilt of the crystal (which is placed on a kinematic mount), the mirrors, and fibre launcher of both arms are typically needed to achieve good alignment.

The spectrum of the collected downconverted photons depends on the focus of the pump beam, the length of the crystal and the collection angle of the collection fibers. For a set of wavevectors $\mathbf{k_0}$ created

by the pump focus, a set of wavevectors $\mathbf{k_1}$ and $\mathbf{k_2}$ obey 4.7, which are then filtered by the position of the collection fibers. For long crystals, like our 5 mm, the crystal length starts to become the dominant factor in the spectrum due to dispersion relations [199]. In SPDC set-ups without a cavity effect the spectrum of the photons is typically wide, as can be seen in figure 4.9 (a). As in most SPDC set-ups, interference filters are used to filter a narrow frequency range, to make the photons more indistinguishable and minimize frequency entanglement between them. We used 20 nm band-gap filters [808 $\pm$ 10 nm, Semrock FF01-810/10-25)], this is wider than in most experiments, but due to the high losses in the plasmonic system high rates of photon pairs were needed. The interference filters are not shown on figure 4.8, they are positioned just in front of the avalanche photodiodes (APDS) [PerkinElmer SPCM-AQR], effectively shielding the APDs from many sources of ambient light. In figure 4.9 (b), we can see that the photons have reasonably well matched spectral shapes after the filtering, important to serve as indistinguishable photons.

In figure 4.9 (c), the temporal distribution of the photon pair coincidence counts is shown. The peak has a FWHM of 800 ps, so 1 ns bins with the maximum coincidence counts were used in all following experiments. We end up with 500 000 coincidence counts per second, with single photon rates of $4 - 4.5 * 10^6/s$. The temporal spread in coincidence counts comes from the jitter in the experimental set-up (APD, Hydraharp 400); the photons itself are generated simultaneously and have wavepackets of only 10s of fs long. From the tails, we can also infer how often a coincidence count is measured from two photons that do not belong to the same pair (so called accidental counts), it is calculated around 12 000 counts/s for a 1 ns bin, so only around 2 % of the true coincidence counts. These numbers are from a rebuilt set-up, performed after the first publication in 2014 [1]. A 3 mm BBO crystal was replaced with the 5 mm BiBO crystal, which has a $\chi^{(2)}$ that is 1.5 - 2 times higher [200]. Furthermore a 100 mW pump laser was replaced with a 175 mW version. From equation 4.10, it can be shown that the generation rate of photon pairs scales linearly with the pump power and quadratically with the crystal length L and the nonlinear susceptibility. Originally only 17 000 pairs per second were recorded.

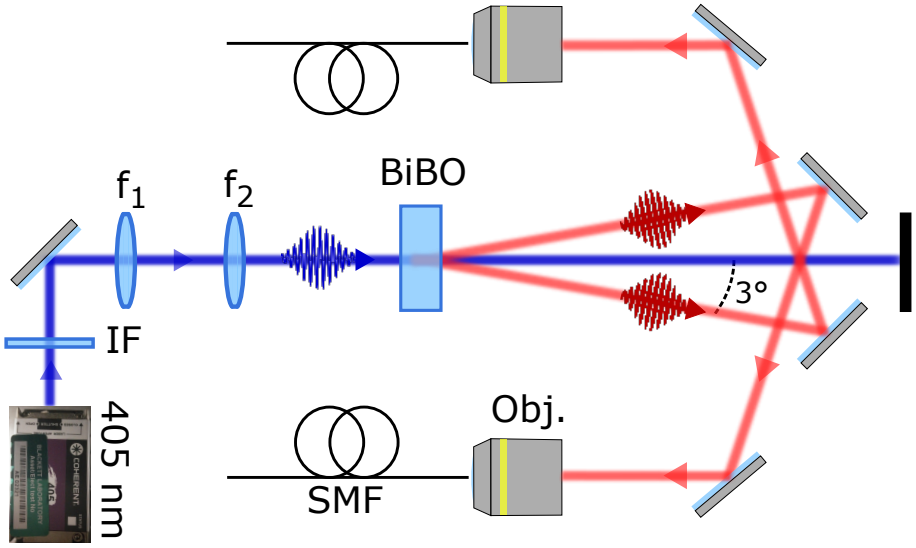


Figure 4.8: A CW 405 nm laser [Coherent OBIS 405 LX] pumps the BiBO crystal with 175 mW. A movable telescopic set-up ($f_1 = 175$ mm,$f_2 = 125$ mm) is used to optimize the focus of the pump beam on the crystal. The output beams are collected into single mode fibres with 10X objectives [Olympus]. Broadband dielectric mirrors [Thorlabs BB1-E03] are used in combination with the interference filters to minimize leakage of scattered laser light into the signal.

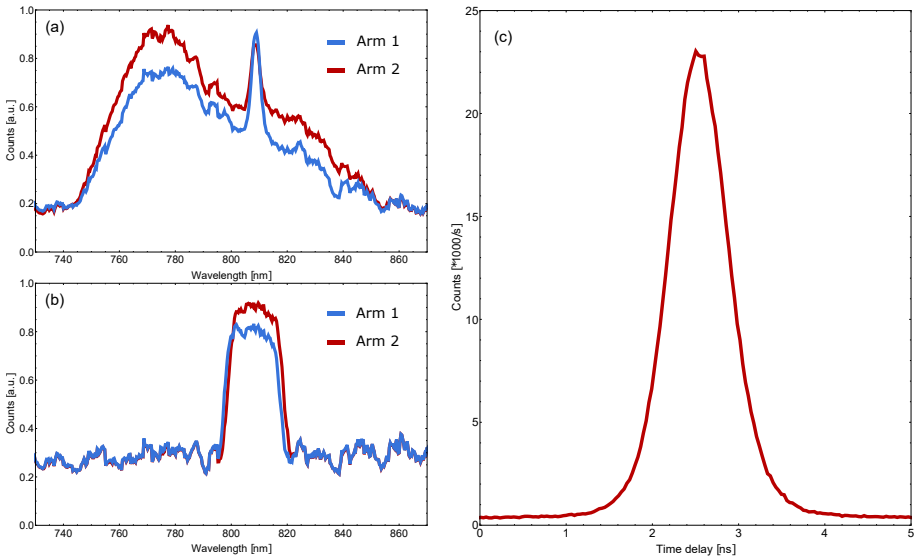


Figure 4.9: **(a)**, The spectrum of both collected down-converted arms. The spurious sharp peak at 808 nm is a higher order diffraction of the pump laser on the spectrometer's grating. **(b)**, spectrum of both arms with the interference filters. **(c)**, Coincidence rate in 32 ps time-bins, one APD has an additional electronic delay of 2 ns.

4.2.2 *Microscope set-up*

To perform the HOM interference experiment with the plasmonic beam splitter, we need to be able to excite the two input gratings with the two separate single photon beams. To achieve accurate discrimination between the two gratings, a high magnification microscope objective [Olympus LMPlan 100x IR] is used. The photons coming out of the output gratings are collected with the same objective and sent to the avalanche photodiodes (APD). Typically, a 50-50 beam splitter is placed in front of the back entrance of the objective to split the photons coming out of the objective from the incoming photons, like in figure 4.2. As each photon has to pass through the beam splitter twice, 3/4 of the photons are lost, which means $1-(\frac{1}{4})^2 = \frac{15}{16}$ of the photon pairs would be lost purely due to the need of splitting the in- and output modes. To avoid this in our measurements, a more intricate imaging set-up was used, shown in figure 4.10. BS1, M1 and M2 are placed on flip-mounts and are flipped down for the plasmonic experiment. The photons coming out of the reflective collimators are guided in a collimated mode with a waist of 2 mm to a pyramid shaped silver mirror, see inset (b). Lenses A with a focal length of 500 mm are placed 500 mm in front of the two faces of the pyramid. This focuses the beams on the pyramid with a spot size diameter of [201]:

$$D = 2\theta_0 f = 2 * 0.00018 * 500mm = 175\mu m \tag{4.11}$$

Where 0.00018 is the approximate divergence angle of the beam coming out of the reflective collimators given on the Thorlabs website [202]. The mirror has a 25 x 25 mm base and the four faces are at an 45° angle. The sample is placed in the focal plane of the objective, this way the objective in combination with tube lens B [f = 300 mm] serves as an infinity corrected imaging system, creating a magnified image with magnification [203]:

$$M_1 = \frac{f_B}{f_{obj.}} = \frac{300mm}{1.8mm} = 167. \tag{4.12}$$

The pyramid mirror is placed in the focal plane of lens B, the magnified image is thus focused on the mirror. The grating to grating distance in the image of the beam splitter is thus just above 2 mm, this means we only use the very tip of the pyramid, but it is possible to align the four arms of the structure nicely along the four sides of the pyramid. The magnification M_2 of the combination of

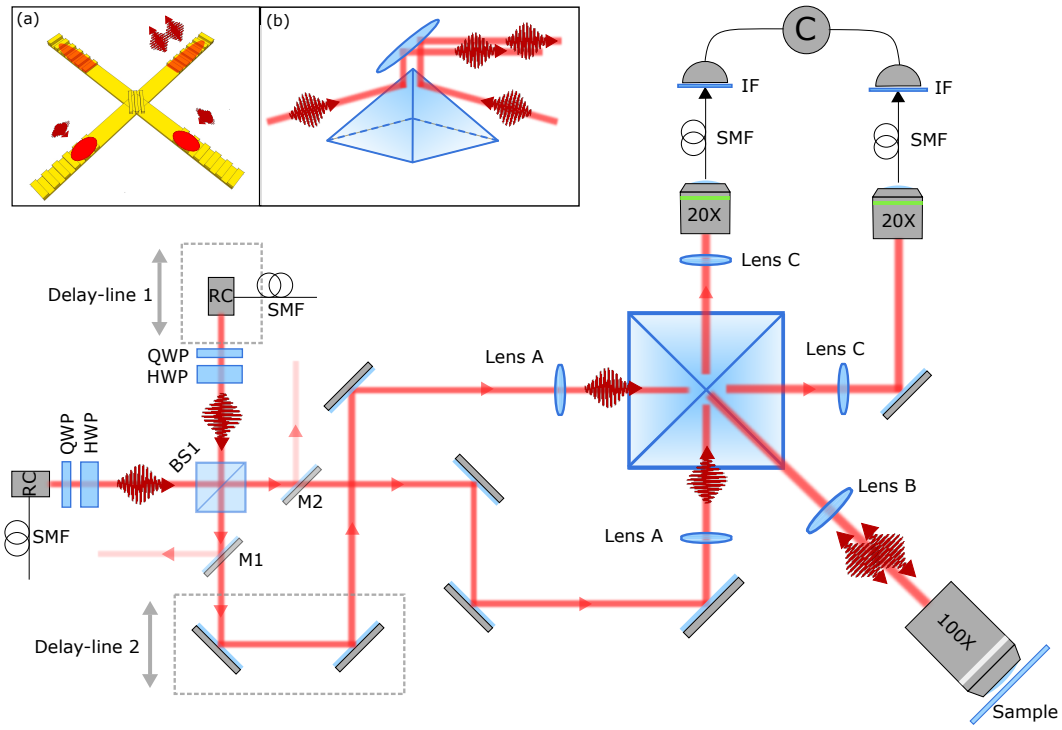


Figure 4.10: Photonic experiment: The single photons coming from the reflective collimators (RC) are directed to a cube beam splitter (BS1), mirrors M1 and M2 guide the output light towards to a collection set-up similar to the top right (not on picture). Plasmonic experiment: BS1, M1 and M2 are taken out of the set-up. The photons are guided through lenses A (f = 750 mm), lens B (f = 300 mm) and 100x objective [Olympus] to the plasmonic beam splitter.

lens C (f = 1000 mm) and the 20x objective in front of each of the single mode fibres, can be calculated with the same formula 4.12: $M_2 = \frac{9mm}{1000mm} = 0.009$. The total magnification from sample to single mode fibre is thus $M_1 M_2$ or 1.5; A circle with diameter ± 3 µm on the sample plane is imaged on the 4.4 µm fibre core. If aligned correctly, we can thus couple the light scattered out at the first 6-7 ridges of the output grating into the single mode fibres. Figure 4.6 shows that this makes it possible to capture most of the photons scattered into free space at the output gratings. The light from the single mode fibres is then coupled to the free space APDs, which are correlated to calculate the coincidence counts, with the 20 nm bandgap interference filters in front of them, as mentioned before.

4.3 RESULTS

4.3.1 *Photonic result*

A photonic interference experiment was done first, to assure the set-up was working correctly and to check the quality of the photon pair source [112]. M1, M2 and BS1 are flipped up for the photonic measurement, the photons do not go to the microscope set-up. Instead both paths are directly redirected to a 10x objective and coupled into single mode fibres (not shown in figure 4.10), which are then coupled to the same APDs shown in the figure. Together with the QWPs and HWPs in between the reflective collimators and BS1, polarizing beam splitters placed in front of both objectives were used to insure that the interfering photons had the same polarization. By coupling into single mode fibres after the beam splitter, we also ensure that the photons are indistinguishable in terms of spatial modes [37]. The top reflective collimator was placed on a motorized delay-line, the driving software of the actuator [Newport TRA25 + ESP301] was integrated with the interface of the PicoQuant Hydraharp 400 in a LabVIEW virtual interface. This allowed automatic measurement of the coincidence counts at the outputs of the beam splitter while gradually changing the relative time delay between the two input photons.

Figure 4.11 shows the result of this scan with 1 μm steps. Each data point is the sum of 4 measurements of 250 ms, the error bars are the estimated standard deviations of the distributions of the sum of the four measurements at each point. This standard deviation is calculated as $\sqrt{4}\sigma_i$, with σ_i the standard deviation of the four measurements at that point [204]. Assuming a top hat shape of the interference filters with a spectral width of $\Delta\omega$, we can derive the expected shape of the interference dip in function of the relative time delay from the general equation 2.28:

$$N_c\,[\delta\tau] := N_c\,[\delta\tau = \infty] * (1 - V * \mathrm{Sinc}\left(\frac{\delta\tau\Delta\omega}{2}\right)^2). \tag{4.13}$$

The fit obtained with free parameters V, $\Delta\omega$ and $N_c\,[\delta\tau = \infty]$ is shown in figure 4.11. A visibility of 0.928 $\pm$0.001 was obtained when the accidental counts are subtracted. The width of the dip corresponds with a spectral width of the photons of 15 nm, which means the dip is slightly wider than expected from the source and filters. The high

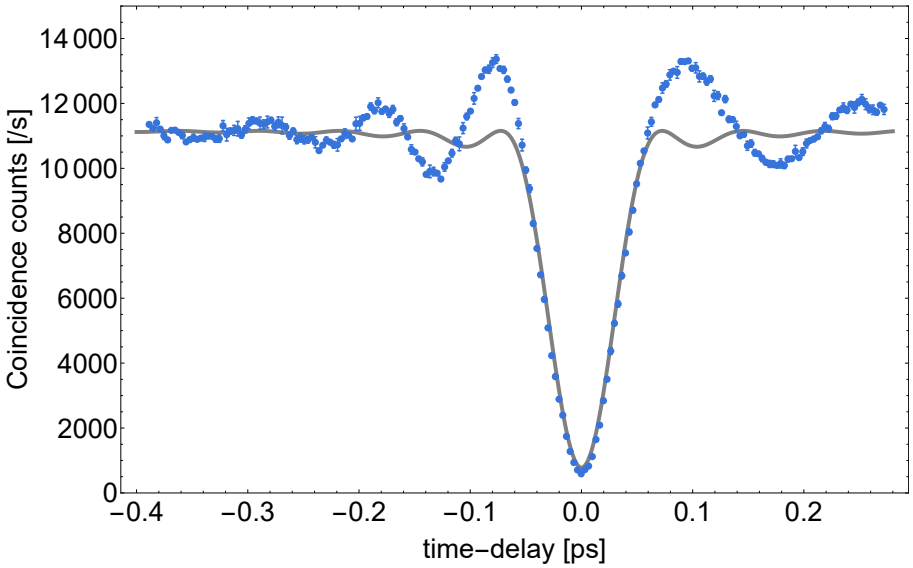


Figure 4.11: Hong-Ou-Mandel interference result on a 50-50 cube beam splitter.

overshooting wings, the slight asymmetry in these wings and the widened dip can probably be attributed to a finite spectral width of the pump and small dispersion effects in the system [205]. Dispersion can also influence the visibility of the dip, but considering the near-perfect interference this can only be a small effect in this measurement.

4.3.2 *Plasmonic result*

In addition to being a benchmark for the Hong-Ou-Mandel interference inside our plasmonic structure, the photonic interference experiment serves as an aid to find the expected location of the plasmonic interference. When the SPDC source and the set-up in figure 4.10 are optimized, a coincidence count rate of 20 per second is reached for the beam splitter with 580 nm input gratings and the Bragg reflector with 3 ridges. This means it would take many hours to scan several millimetres to find the position of the interference. Instead, the two paths going from BS1 to the plasmonic sample are again used as a Mach-Zehnder interferometer, similar to the measurement in figure 4.7. The diode laser [PicoQuant LDH-P-810] has a spectral width of 5-7 nm, resulting in a coherence length of around 50 µm. The result

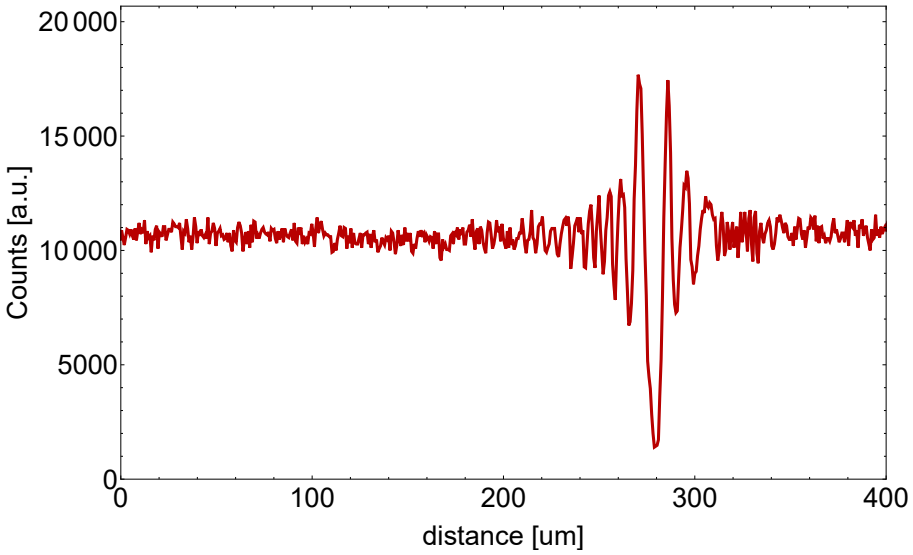


Figure 4.12: Mach-Zehnder interference.

of such a quick scan is shown in figure 4.12, interference fringes allow us to locate the symmetry position within tens of microns.

BS1 is taken out of the the optical path after this measurement (with a flip mount) and delay-line 1 is used to scan for the plasmonic Hong-Ou-Mandel dip. The result is shown in figure 4.13 below. The interference has a visibility of 0.579 $\pm$0.004, which is well above the classical limit of 0.5. However, it does not come close to the 0.93 obtained with the cube beam splitter. The biggest reason for this is the deviation from the $\pi/2$ phase shift between r and t, the equations in section 2.1.3 show that the earlier measured phase shift of 1.21 puts the maximum obtainable visibility at 0.75. This number is rather sensitive to the phase shift, a small change to 1.15 already puts the maximum visibility at 0.66. It is thus not unrealistic that the real phase shift contributes more to the loss in visibility than expected from a measured value of 1.21. Dispersion in the plasmonic part of the system can also have had an influence. Together with a photon pair source that does not deliver 100 % indistinguishable photons (shown by the photonic interference visibility) and potential small deviations from 50/50 splitting of the beam splitter, a visibility of 0.58 is within the range of expectation. Our first publication in 2014 showed a visibility of 0.72 $\pm$ 0.13; although we obtained a lower estimate of the visibility after rebuilding the set-up, the current results break the classical limit of 0.5 much more reliably. A scan was also performed with a

beam splitter with 4 gratings and a 550 nm period for the Bragg reflector. According to table 1, the reflection/transmission is around 0.6/0.4, yet a visibility of only 0.24 was reached. This clearly shows the sensitivity of the phase difference on the specific Bragg reflector parameters and its consequent influence on the coalescence effect. This has been explicitly shown in a very recent publication where the coalescence dip was turned into a anti-coalescence peak by tuning the parameters of a groove plasmonic Bragg reflector to obtain a phase difference ϕ_{r-t} of π [134, 206]. Interestingly, imperfect visibility of the dip due to a deviation from the $\frac{\pi}{2}$ phase difference implies a coalescence of the two photons into the unmeasured channel. In both our measurements and the aforementioned anti-coalescence peak this channel could be scattering losses into free space at the Bragg reflector. More exotic is the effect when the only loss channel is absorption (into the metal), as the coalescence of the photons into this loss channel implies non-linear absorption in the linear medium. In the perfect case the photons or get absorbed together or they don't get absorbed [99]. The more well-known phase dependent absorption process Coherent Perfect Absorption (CPA) has already been performed on the single photon level with a plasmonic film [207] and a hybrid silicon-plasmonic waveguide-based coupler has been suggested to perform CPA recently [208]. Further investigations in this direction to directly prove two-photon absorption in a linear medium could be of high interest.

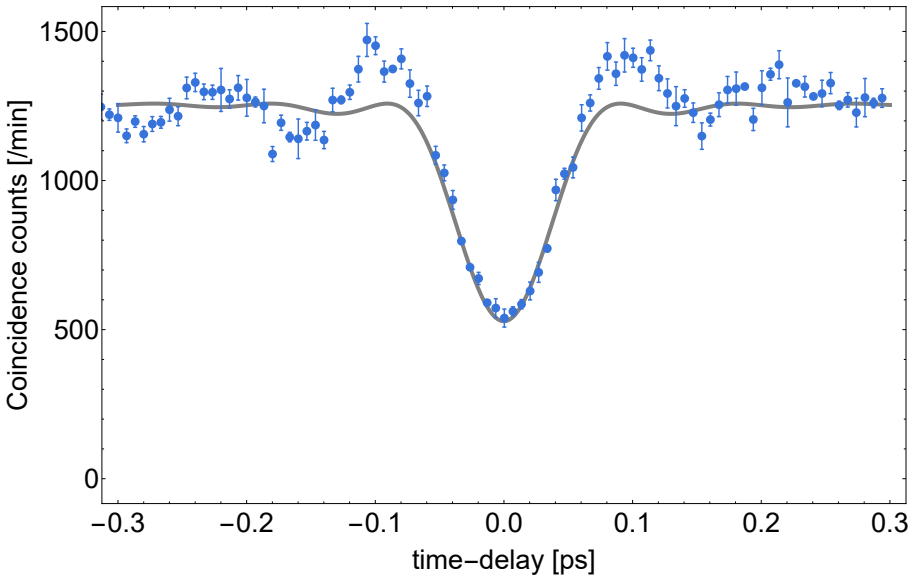


Figure 4.13: Hong-Ou-Mandel interference at the plasmonic beam splitter. The grey line shows a fit of function 4.13 with the visibility, spectral width and the baseline taken as free parameters.

5

QUANTUM STATE TOMOGRAPHY

After showing the bosonic behaviour of Surface Plasmon Polaritons by performing a Hong-Ou-Mandel interference experiment, we now probe whether entanglement is generated in this interference. Preservation of entanglement of SPPs has been shown in a variety of experiments, yet, to our knowledge, none probes the generation in a plasmonic structure. To do this, we reconstruct the density matrix of the output state of the interference by performing quantum state tomography. In section 5.2 we will outline a tomography technique for single-mode photon-number states in the polarization basis:

$$\sum_{n=0}^{N} c_n \left|n\right\rangle_V \left|N-n\right\rangle_H, \qquad \sum_{n=0}^{N} |c_n|^2 = 1. \tag{5.1}$$

To make this useful for the quantum interference, we have to transform the output state from the two output paths of the beam splitter to a single spatial mode, while transferring the path information onto the polarization basis. For the expected NOON state, this means:

$$(|20\rangle + |02\rangle)/\sqrt{2} \rightarrow (|20\rangle_{VH} + |02\rangle_{VH})/\sqrt{2} \tag{5.2}$$

In section 5.3 we will explain how this is done by superimposing both beams onto a polarizing beam splitter (PBS). The several experimental steps needed to align the set-up and the final results will also be shown here. First, the Entanglement of Formation, a well-known entanglement measure for a 2-qubit system will be introduced together with its use for our situation.

5.1 ENTANGLEMENT OF FORMATION

The SPDC photon pair source emits by good approximation only 2 photons at a time, we use this assumption to limit the basis of both output modes of the beam splitter to a maximum of 2 photons: $\{|0\rangle, |1\rangle, |2\rangle\}$. Each output mode could thus separately be treated as a three-level quantum system or qutrit, resulting together in a qutrit-qutrit structure. Unfortunately, there are no clear techniques or measures to quantify entanglement for general mixed qutrit-qutrit states,

so we will reduce our problem to a qubit-qubit problem. First, our measurements are conducted in the coincidence basis, so only components with exactly 2 photons in the 2 output modes together are considered. This results in a basis for the full state with only the three components $\{|20\rangle, |11\rangle, |02\rangle\}$, so a 3 by 3 density matrix. We can filter out the $|11\rangle$ state with a hypothetical filter that measures if there is exactly one photon in the mode and only passes through the states of which this is not the case. This is a local operation and the filter uses no information about the the number of photons in the other output mode [209]. This means the operation cannot generate entanglement between the modes [121]. It can destroy entanglement in the system, meaning that the measured entanglement in the filtered state will be a lower bound for the entanglement present in the actual experimental state. The filtering is simply done in the post-processing:

$$\begin{pmatrix} \rho_{11} & \rho_{12} & \rho_{13} \\ \rho_{21} & \rho_{22} & \rho_{23} \\ \rho_{31} & \rho_{32} & \rho_{33} \end{pmatrix} \rightarrow \begin{pmatrix} 0 & 0 & 0 & 0 \\ 0 & \rho_{11} & \rho_{13} & 0 \\ 0 & \rho_{31} & \rho_{33} & 0 \\ 0 & 0 & 0 & 0 \end{pmatrix} \tag{5.3}$$

All the $|11\rangle$ components are discarded and a new matrix is constructed in the $\{|00\rangle, |20\rangle, |02\rangle, |22\rangle\}$ basis, which is the basis for 2 coupled qubits with the two levels $|0\rangle$ and $|2\rangle$. The $|22\rangle$ components are set to 0 with the same assumption as before: there are only 2 photons in the system due to the source. Considering the high losses in the system, the top left $|00\rangle\langle 00|$ component is in reality large, yet not directly measurable. We are interested in the subset of the output states with useable entanglement -for hypothetical quantum optics circuitry after the beam splitter- and so also this component is set to 0. The majority of input states $|11\rangle$ will result in an output state with 0 photons, but it is on the subset of output states with two photons that we want to show the generation of entanglement, by using the Entanglement of Formation.

The Entanglement of Formation is the extension of the entropy of entanglement to 2-qubit mixed states. It is defined as the average entanglement of the pure states of the decomposition, minimized over all possible decompositions of ρ [120]:

$$E(\rho) = \min \left[\sum p_i E(\Psi_i) \right] \tag{5.4}$$

It was shown by Wootters [123] that the above equation can be expressed as an explicit function of ρ for a system of two qubits:

$$E(\rho) = h\left[\frac{1+\sqrt{1-C[\rho]^2}}{2}\right], \text{ with:} \tag{5.5}$$
$$h[x] = -x\log_2(x) - (1-x)\log_2(1-x),$$
$$C(\rho) = \max\{0, \lambda_1 - \lambda_2 - \lambda_3 - \lambda_4\}.$$

Where the λ_is are, in decreasing order, the square roots of the eigenvalues of the matrix $\rho\tilde{\rho}$. $\tilde{\rho}$ is the spin-flipped state of ρ. The spin-flip on a single qubit, here in the basis $\{|0\rangle, |2\rangle\}$, is defined by the operator $\sigma_y = \begin{pmatrix} 0 & -i \\ i & 0 \end{pmatrix}$. For a two qubit state, the spin-flip on each separate qubit results in the density matrix $\tilde{\rho} = (\sigma_y \otimes \sigma_y)\rho^*(\sigma_y \otimes \sigma_y)$. Both the Entanglement of Formation E or the Concurrence C range from 0 to 1, with 0 meaning no entanglement and 1 meaning full entanglement between the two qubit subsystems.

5.2 QUANTUM TOMOGRAPHY SET-UP

5.2.1 *Polarization optics*

In the Jones matrix notation, where horizontally polarized light $|H\rangle = \begin{pmatrix} 1 \\ 0 \end{pmatrix}$ and vertically polarized light $|V\rangle = \begin{pmatrix} 0 \\ 1 \end{pmatrix}$, polarization transformations of incoming light by quarter-wave and half-wave plates are given by respectively:

$$QWP(\alpha) = \begin{pmatrix} \cos^2(\alpha) + i\sin^2(\alpha) & (1-i)\sin(\alpha)\cos(\alpha) \\ (1-i)\sin(\alpha)\cos(\alpha) & \sin^2(\alpha) + i\cos^2(\alpha) \end{pmatrix} \tag{5.6}$$

and

$$HWP(\alpha) = \begin{pmatrix} \cos(2\alpha) & \sin(2\alpha) \\ \sin(2\alpha) & -\cos(2\alpha) \end{pmatrix}. \tag{5.7}$$

With α the angle between the fast axis of the phase retarder and the horizontal axis. Wave plates are thin slabs of a birefringent material, typically quartz, in which light polarized along two specific orthogonal axes experience (slightly) different refractive indices. For light of

any polarization, the phase difference between the polarization components along the axes of the material will thus gradually change. Half-wave plates and quarter-wave plates create phase shifts of exactly a half a wavelength (and thus π radians of phase) and a quarter of a wavelength ($\frac{\pi}{2}$) respectively, resulting in the above given transformations of the polarization of the incoming light. In the experiments explained later in this chapter, zero-order wave plates are used [Thorlabs] in which two multi-order quartz wave plates are combined to result in a total path length difference of $\frac{\lambda}{2}$ or $\frac{\lambda}{4}$, rather then $n + \frac{\lambda}{2}$ or $n + \frac{\lambda}{4}$ for single multi-order wave plates. This delivers a broader wavelength range at which the wave plates work as intended. For the 20 nm spectral width of our photons the deviation is less than 0.5 %.

It was proven that a combination of two quarter-wave plates and a half-wave plate (in any order) can realize any polarization transformation, or equivalent, any rotation on the Poincare sphere.[210] With abstract angles θ and ϕ, such a transformation can be expressed as:

$$\begin{pmatrix} \hat{b}_H \\ \hat{b}_V \end{pmatrix} = U(\theta, \phi) \begin{pmatrix} \hat{a}_H \\ \hat{a}_V \end{pmatrix}, with: \tag{5.8}$$

$$U(\theta, \phi) = \begin{pmatrix} \cos(\theta) & e^{i\phi}\sin(\theta) \\ -e^{-i\phi}\sin(\theta) & \cos(\theta) \end{pmatrix}$$

$\hat{a}_{H,V}$ and $\hat{b}_{H,V}$ are the annihilation operators of the modes before and after the phase retarders. This fact is crucial for the polarization-based quantum state tomography set-up we use in our experiments.

5.2.2 *Polarization-based Quantum State Tomography*

It was shown by Agarwal *et al.* that all N-order coherences between the two polarization modes $\hat{a}_H$ and $\hat{a}_V$ of any light field in a single spatial mode can be obtained by measuring only N-order intensity moments of one of the two polarization modes behind two quarter-wave and one half-wave plate [211, 212]. The horizontal mode is selected by adding a polarizing beam splitter after the wave plates, see figure 5.1. Due to the lack of photon number detectors, two correlated detectors placed at the two output ports of a 50/50 beam splitter are typically used to measure the second order intensity of a light mode. We can easily show that this measurement is indeed proportional to

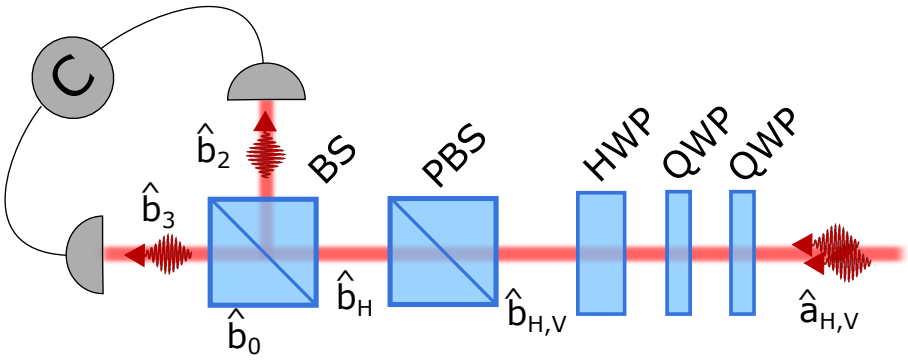


Figure 5.1: Quantum state tomography set-up.

the second order intensity $\left\langle (\hat{b}_H^\dagger)^2 \hat{b}_H^2 \right\rangle$; with $\hat{b}_{2,3}$ the bosonic operators of the two output modes behind the beam splitter and $\hat{b}_0$ of the second input mode:

$$\begin{aligned}\left\langle \hat{b}_2^\dagger \hat{b}_3^\dagger \hat{b}_2 \hat{b}_3 \right\rangle &= \frac{1}{4} \left\langle (-i\hat{b}_H^\dagger + \hat{b}_0^\dagger)(\hat{b}_H^\dagger - i\hat{b}_0^\dagger)(i\hat{b}_H + \hat{b}_0)(\hat{b}_H + i\hat{b}_0) \right\rangle \\ &= \frac{1}{4} \left\langle \hat{b}_H^\dagger \hat{b}_H^\dagger \hat{b}_H \hat{b}_H \right\rangle \end{aligned} \tag{5.9}$$

The first step uses the input-output relations of the unitary beam splitter, the second step the fact that input 0 only contains the vacuum mode and $\hat{b}_0 |0\rangle = 0$.

We want to reconstruct the density matrix, so we have to show that the elements of the density matrix are related to the higher order coherences the set-up can measure. This can be done by calculating $\langle \hat{A} \rangle = \mathrm{Tr}[\hat{\rho}\hat{A}]$ in the matrix notation for the higher order coherences, writing out the calculations gives:

$$\begin{aligned}&\left\langle (\hat{a}_H^\dagger)^{N-w} (\hat{a}_V^\dagger)^w \hat{a}_H^{N-y} \hat{a}_V^y \right\rangle \\ &= \sum_{\mu\nu} \langle \mu\nu | \sum_{\gamma\kappa,\alpha\beta} \rho_{\gamma\kappa,\alpha\beta} |\gamma\kappa\rangle \times \\ &\qquad \langle \alpha\beta | (\hat{a}_H^\dagger)^{N-w} (\hat{a}_V^\dagger)^w \hat{a}_H^{N-y} \hat{a}_V^y |\mu\nu\rangle \\ &= \langle N-y, y | \sum_{\gamma\kappa,\alpha\beta} \rho_{\gamma\kappa,\alpha\beta} |\gamma\kappa\rangle \times \\ &\qquad \langle \alpha\beta | (\hat{a}_H^\dagger)^{N-w} (\hat{a}_V^\dagger)^w \hat{a}_H^{N-y} \hat{a}_V^y |N-y, y\rangle \\ &= \rho_{yw} \langle N-y, y | N-y, y\rangle \times \\ &\qquad \langle N-w, w | (\hat{a}_H^\dagger)^{N-w} (\hat{a}_V^\dagger)^w \hat{a}_H^{N-y} \hat{a}_V^y |N-y, y\rangle \\ &= \rho_{yw} \sqrt{(N-w)!w!(N-y)!y!}. \end{aligned} \tag{5.10}$$

For this we used $\hat{a}^n |n\rangle = \sqrt{n!}\,|0\rangle$ and $\langle n|m\rangle = \delta_{nm}$. We can see that the measured value of a N^{th} order coherence is related to the density

matrix element with the same indices, but it is important to include the factor $\sqrt{(N-w)!w!(N-y)!y!}$.

There are 9 second-order coherences of the initial state: $\left\langle \hat{a}_H^\dagger \hat{a}_H^\dagger \hat{a}_H \hat{a}_H \right\rangle$, $\left\langle \hat{a}_H^\dagger \hat{a}_H^\dagger \hat{a}_H \hat{a}_V \right\rangle$, $\left\langle \hat{a}_H^\dagger \hat{a}_V^\dagger \hat{a}_H \hat{a}_H \right\rangle$, $\left\langle \hat{a}_H^\dagger \hat{a}_V^\dagger \hat{a}_H \hat{a}_V \right\rangle$, $\left\langle \hat{a}_H^\dagger \hat{a}_H^\dagger \hat{a}_V \hat{a}_V \right\rangle$, $\left\langle \hat{a}_H^\dagger \hat{a}_V^\dagger \hat{a}_V \hat{a}_V \right\rangle$, $\left\langle \hat{a}_V^\dagger \hat{a}_V^\dagger \hat{a}_H \hat{a}_V \right\rangle$, $\left\langle \hat{a}_V^\dagger \hat{a}_V^\dagger \hat{a}_H \hat{a}_H \right\rangle$ and $\left\langle \hat{a}_V^\dagger \hat{a}_V^\dagger \hat{a}_V \hat{a}_V \right\rangle$. Only the second-order intensities $\left\langle \hat{a}_H^\dagger \hat{a}_H^\dagger \hat{a}_H \hat{a}_H \right\rangle$, $\left\langle \hat{a}_V^\dagger \hat{a}_V^\dagger \hat{a}_V \hat{a}_V \right\rangle$ and $\left\langle \hat{a}_H^\dagger \hat{a}_V^\dagger \hat{a}_H \hat{a}_V \right\rangle$ are directly accessible. With equation 5.8, any second order-coherence of the field after the SU(2) gadget can be expressed in function of the second-order coherences of $\hat{a}_{H,V}$:

$$\begin{aligned}
&\left\langle (\hat{b}_H^\dagger)^i (\hat{b}_V^\dagger)^{(2-i)} \hat{b}_H^i \hat{b}_V^{(2-i)} \right\rangle = \\
&\sum_{w,y=0}^{i} \sum_{x,z=0}^{2-i} \binom{i}{w}\binom{i}{y}\binom{2-i}{x}\binom{2-i}{z} \times \\
&(\cos(\theta))^{4-w-x-y-z} (\sin(\theta))^{w+x+y+z} (-1)^{x+z} e^{i\phi(x+y-w-z)} \times \\
&\left\langle (\hat{a}_H^\dagger)^{(i+x-w)} (\hat{a}_V^\dagger)^{(2-i-x+w)} \hat{a}_H^{(i+z-y)} \hat{a}_V^{(2-i-z+y)} \right\rangle
\end{aligned} \tag{5.11}$$

As explained in the schematic drawing, we are only measuring the second-order intensity of the horizontal field, which means putting $i = 2$ in the previous equation, resulting in a more simple equation:

$$\begin{aligned}
B = \sum_{w,y=0}^{2} &\binom{2}{w}\binom{2}{y} \cos(\theta)^{4-w-y} \sin(\theta)^{w+y} \times \\
&e^{i\phi(y-w)} \sqrt{(2-w)!w!(2-y)!y!}\, \rho_{2-w,w,2-y,y}
\end{aligned} \tag{5.12}$$

Where we replaced the second-order coherences by the state's density matrix elements with equation 5.10. We can clearly see in the above equation that B is function of all of the nine second-order coherences of the initial field, or all nine elements of the density matrix. To solve for these 9 independent variables $\rho_{2-y,y,2-w,w}$, we need 9 independent linear equations. This is achieved by choosing a right combination of 9 pairs (θ_k, ϕ_k), which were calculated in ref [211], the angles

are shown in table 2. With B_k the coincidence measurement for the k^{th} angle pair, the set of linear equations can be written as:

$$B_k = \sum_{w,y=0}^{2} R_k^{wy} \rho_{wy} \tag{5.13}$$

$$R_k^{wy} = \binom{2}{w}\binom{2}{y} \cos(\theta)^{4-w-y} \sin(\theta)^{w+y} e^{i\phi(y-w)} \times \frac{}{\sqrt{(2-w)!w!(2-y)!y!}} \tag{5.14}$$

For notation convenience, we will use ρ_{wy} for $\rho_{2-w,w,2-y,y}$. $Det[R_k^{wy}] \neq 0$ confirms that the equation are independent; we can find a unique solution for each of the second-order coherences of the initial field if we perform the 9 measurements of B with the different angle pairs. For this, we need to relate the abstract angles θ and ϕ to the experimental angles α_{QWP1}, α_{QWP2} and α_{HWP} between the horizontal axis and the fast axes of the two quarter-wave plates and the half-wave plate respectively. This is done by solving $U(\theta,\phi) = HWP(\alpha_{HWP}) \times QWP(\alpha_{QWP2}) \times QWP(\alpha_{QWP1})$ -obtained by combining equations 5.6, 5.7 and 5.8- to α_{QWP1}, α_{QWP2} and α_{HWP}. The result of this is also shown in table 2.

θ_k	ϕ_k	α_{QWP1}	α_{QWP2}	α_{HWP}
$\frac{\Pi}{8}$	$\frac{2\Pi}{3}$	0.102	0.440	1.740
$\frac{2\Pi}{8}$	$\frac{2\Pi}{3}$	1.803	1.144	2.812
$\frac{3\Pi}{8}$	$\frac{2\Pi}{3}$	2.010	1.083	2.678
$\frac{\Pi}{8}$	$\frac{4\Pi}{3}$	0.102	2.906	1.402
$\frac{2\Pi}{8}$	$\frac{4\Pi}{3}$	0.232	2.715	1.241
$\frac{3\Pi}{8}$	$\frac{4\Pi}{3}$	0.439	2.654	1.107
$\frac{\Pi}{8}$	0	$\frac{\Pi}{4}$	$\frac{\Pi}{4}$	$\frac{13\Pi}{16}$
$\frac{2\Pi}{8}$	0	$\frac{\Pi}{4}$	$\frac{\Pi}{4}$	$\frac{14\Pi}{16}$
$\frac{3\Pi}{8}$	0	$\frac{\Pi}{4}$	$\frac{\Pi}{4}$	$\frac{15\Pi}{16}$

Table 2: The 9 different combinations of abstract angles (θ,ϕ) and experimental angles (α_{QWP1}, α_{QWP2}, α_{HWP})

A first approach to obtain the density matrix from the experimental values would be by solving the nine equations directly, in matrix notation: $\rho_{mn} = \sum_{k=1}^{9} (R_k^{wy})^{-1} B_k$. Unfortunately, due to experimental noise, this could result in a non-physical density matrix, i.e. a

matrix that is not Hermitian, positive semi-definite or normalized. This problem can be solved by searching for the most likely physical state (so density matrix) that could have produced the experimentally obtained results. The Cholesky decomposition in linear algebra says that any Hermitian positive-semidefinite matrix can be decomposed in a lower triangular matrix and its conjugate transpose. Any 3 by 3 physical density matrix can thus be described with 9 unknown real parameters:

$$\rho_{phys}(t_1, t_2, ..., t_{10}) = T^\dagger T, \text{ with :} \tag{5.15}$$

$$T = \begin{pmatrix} t_1 & 0 & 0 \\ t_4 + it_5 & t_2 & 0 \\ t_6 + it_7 & t_8 + it_9 & t_3 \end{pmatrix} \tag{5.16}$$

By replacing ρ by ρ_{phys} in equation 5.13, we get a set of equations that ensure a physically correct solution. Due to the extra restrictions, an exact solution is normally not possible. Instead maximum likelihood estimation (MLE) is used, which maximizes a likelihood function over the variables t_i. If we assume uncorrelated Gaussian noise for each of the 9 coincidence measurements, the conditional probability of a set of measurements is given by:

$$P(B_1, ..., B_9 | t_1, ..., t_9) \propto \prod_{k=1}^{9} Exp\left[-\frac{(B_k - \sum_{w,y=0}^{2} R_k^{wy} \rho_{phys,wy})^2}{2\sigma_k^2} \right] \tag{5.17}$$

Maximizing this probability function, which was done by minimizing $\sum_{k=1}^{9} \frac{(B_k - \sum_{w,y=0}^{2} R_k^{wy} \rho_{phys})^2}{2\sigma_k^2}$ with the NMinimize function in Mathematica, gives us the most likely combination of parameters $\{t_i\}$ for the given set of measurements and thus the most likely density matrix. We assume Poissonian shot noise as the main noise contributor, which means we can approximate σ_k as $\sqrt{B_k}$. To have an understanding of the influence of the shot noise on the estimated density matrix and extracted measures like Entanglement and Fidelity, a Monte Carlo simulation with a 1000 iterations is done. In each iteration, the experimentally obtained values B_k are replaced by random numbers taken from Poissonian distributions with parameter B_k. These values are then used for the same optimization distribution as before.

5.3 RESULTS

To use the described polarization based tomography set-up on the output of a Hong-Ou-Mandel interference, the state has to be transformed from the 'path-basis' to the polarization basis. This is done by superimposing both output beams from the beam splitter on a polarizing beam splitter, as shown in figure 5.2 for the photonic case and 5.5 for the plasmonic one. With quantum state tomography we are capable of distinguishing this pure state from the mixed NOON state variant $(|20\rangle\langle 20| + |02\rangle\langle 02|)/\sqrt{2}$, which would give identical results with a simple coincidence measurement. The spectral width and thus finite coherence length of both the separate photons and combined biphoton state imposes the need for temporal alignment of the system, equivalent to the difference between the coalescence effect of two monochromatic photons and the real-life Hong-Ou-Mandel dip. The final tomography results and the steps needed to get there will be outlined in the following subsections for the photonic and plasmonic case respectively. The work with a photonic cube beam splitter was performed to both test the set-up and to have a benchmark for the plasmonic results.

5.3.1 *Photonic results*

The set-up shown in figure 5.2 uses the same optical elements as the beginning of the set-up shown in figure 4.10 in the previous chapter: the two photons coming out of two separate single mode fibres are collimated by reflective collimators and both go through a quarter and half wave plate to create a linear horizontal polarization, after which they are mixed at the 50/50 cube beam splitter BS1. The half wave plate in one of the two outputs changes the polarization to vertical, this results into all photons in that beam being reflected, while the photons coming from the other output of BS1 are being transmitted through the PBS due to their horizontal polarization. The beam containing both polarizations is then coupled into a polarization maintaining fibre, to make it easier to switch between the photonic and plasmonic set-up and to clean up the spatial modes, and sent to the quantum tomography set-up depicted in figure 5.1. To couple the two polarizations correctly on the two perpendicular axes of the birefringent PMF, a half wave plate was added in front of the objective. This

ensures minimal mixing of the two polarizations while travelling in the fibre. Furthermore, a half wave plate was added behind the PMF to rotate the two perpendicular polarization modes back to horizontal and vertical polarization in free space. Considering the correct representation of the initial interference output state depends on a correct alignment of the polarizations, we experimentally characterized the polarization of the beam after the PMF. This was done by measuring the Stokes parameters while blocking the horizontal and vertical path in the Mach-Zehnder interferometer consecutively. To minimize the influence of potential errors in the angles of the quarter wave and half wave plates, this was done with a technique that involves only one rotatable quarter wave plate and a fixed polarizer (the PBS in this case). It is shown that the Stokes parameters can be calculated out of an even number of intensity measurements (minimum 8) behind the PBS with the quarter wave-plate rotating in equal steps of π/N [213]. After optimizing the PMF, both the vertical and horizontal polarization have less than 1^o of ellipticity and are within 1^o of the correct polarization. This means that the polarization tomography should represent the output state of the beam splitter in the path basis accurately.

To probe the output HOM state, we first have to align delay-line 1 into the symmetric position. This was done without having to move any optical elements by aligning the fast axes of the quarter and half wave plates of the tomography part horizontally, so putting the angles of the rotators at 0 radians. The final PBS will only transmit the photons from the horizontal path after BS1. By measuring the coincidence counts of the two detectors, we can measure the rate of the two photon state $|2\rangle$. In the ideal case, scanning delay-line 1 into symmetry changes the state entering the tomography stage from $(|1_A 1_B\rangle_{VV} + |1_A 1_B\rangle_{VH} + |1_A 1_B\rangle_{HV} + |1_A 1_B\rangle_{HH})/2$ to $(|20\rangle_{VH} + |02\rangle_{VH})/\sqrt{2}$. We can only drop the labels A and B of the two separate photons when they are fully indistinguishable, also temporally. We will explain the influence of the distinguishability of the photons on our tomography scheme later. In the situation where the delay line is out of symmetry, we will only measure coincidences when both photon A and B are in the horizontal mode, which is 25 % of the time. When the photons do arrive simultaneously at the beam splitter, the coalescence of the

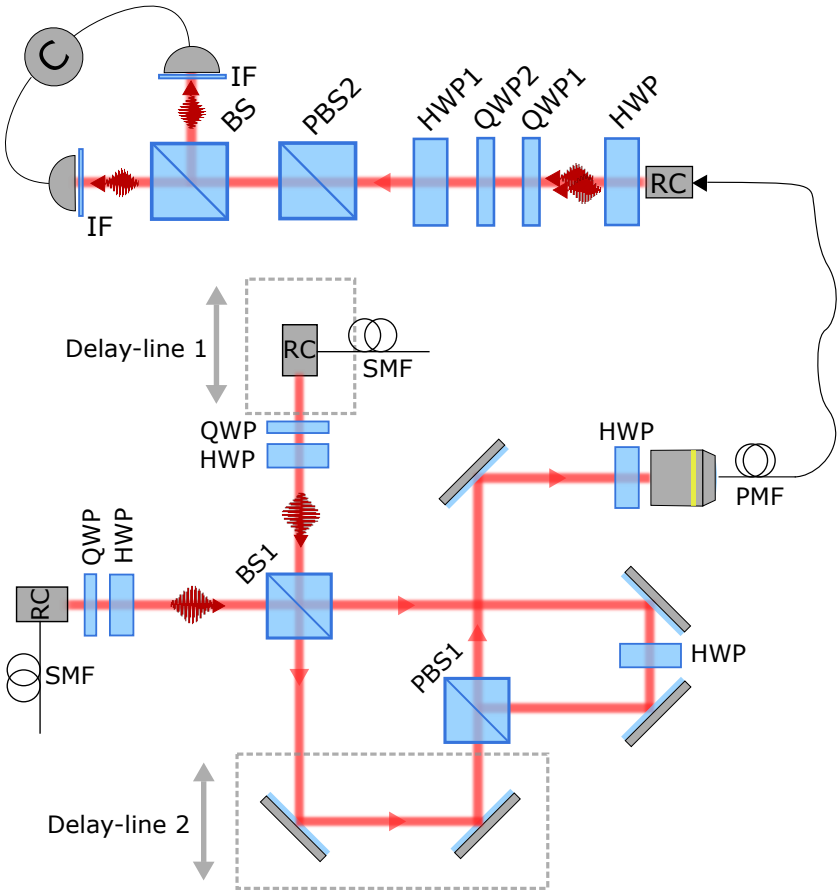


Figure 5.2: Schematic drawing of the photonic QST set-up. QWP1, QWP2 and HWP1 are placed in motorized rotators.

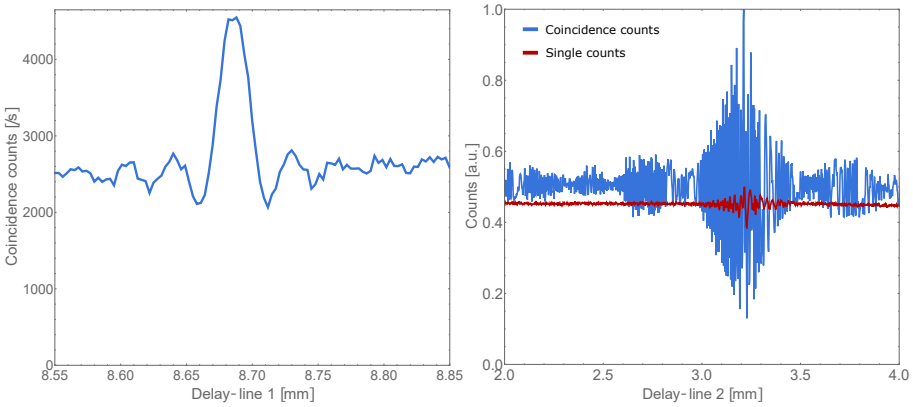


Figure 5.3: Left: Scan of delay-line 1 with the tomography quarter and half wave plates at 0 radians. Right: Scan of delay-line 2 with the tomography phase retarders set at angle combination 8.

photons will double this to 50 %, as we can also see from the state vector. This peak in coincidence counts in function of the delay-line position is shown in figure 5.3 (a). Converting a full width of approximately 50 µm to picoseconds we get a temporal width of 0.16 ps, in good agreement with the Hong-Ou-Mandel dip shown in figure 4.11

To find the symmetry position of delay-line 2, we need to make vertical and horizontal polarization interfere with each other. This can be done by having a polarizer with its transparent axis halfway between the two perpendicular polarizations. The electric field passed through is the component of the sum of the two electric fields that is parallel to the polarizer's axis. We make the horizontal and vertical polarization symmetrical around the horizontal axis of the polarizing beam splitter by changing the angles of the wave plates of the tomography set-up: the angle of the HWP is put at $\frac{\pi}{8}$, while the QWPs stay at 0. The horizontal polarization is transformed to a linear polarization with a $\frac{\pi}{4}$ angle (so-called diagonal polarization), while the vertical polarization rotates to a $-\frac{\pi}{4}$ angle, or the anti-diagonal polarization. By scanning delay-line 2, the phase between the anti- and diagonal polarization rotates and the total electric field periodically becomes parallel and perpendicular to the transmitting axis of the PBS. The result is perfectly equivalent to an interference scan with a Mach-Zehnder interferometer in which both arms have the same polarization. The result is shown in figure 5.3 (b). When delay-line 2 is at a 3.2 mm offset, the interference visibility is at its maximum, showing maxi-

mum temporal overlap. It is important to note that the interference probed by measuring the coincidence counts, ie. the second-order coherence, does not come from the interference of the single photons, but rather by interfering the two terms of the bi-photon HOM state. This is also called the de Broglie wave, in which an ensemble of 2 (or N) identical photons have interference fringes with a period of $\lambda/2$ (or λ/N) [156, 214, 215]. From these publications we learn two important characteristics of these de Broglie interferences. First, the coherence length is defined by the coherence length of the pump laser of the SPDC set-up, which is normally considerably longer than the coherence length of the seperate photons. This can be seen by comparing the first order coherence with the second order coherence in figure 5.3. Intuitively this can be understood from the fact that albeit the separate photons have a large frequency uncertainty, the sum of their frequencies is fixed by the frequency of the pump laser, see equation 4.6. In our case, the 404 nm diode laser has multiple longitudinal modes, which results in a complex coherence function, with multiple peaks (only the central one is shown in the figure) and with a coherence length within one peak of several hundreds of micrometer. This coherence length can of course be made considerably longer by pumping with a single-mode laser [216]. The single photon interferences in the first-order coherence do not cancel out perfectly due to slightly imbalanced alignment of the two input ports, so we can use this signal to put the interferometer more accurately into the balanced position. Second, the de Broglie interferences are not a proof of entanglement between the photons travelling in the two arms. Kwon et al. show that the interferences also arise when the two incoming photons are perfectly distinguishable and there is no HOM interference to generate the NOON state [156].

After aligning both the first and the second delay-line, the expected HOM state can be probed with the tomography set-up. A result of our measurements is shown in figure 5.7 (a). The populations on the diagonal are 0.52, 0.03 and 0.45, a perfect interference would give 0.5, 0.0 and 0.5, while the theoretically expected values outside of the Hong-Ou-Mandel interference are 0.25, 0.5 and 0.25. The asymmetry in the $|20\rangle$ and $|02\rangle$ states can be attributed to having one arm of the interferometer slightly better aligned than the other. The $|11\rangle$ dropping from 0.5 to 0.03 is equivalent to an interference visibility of the dip of

94 % , in excellent agreement with the 93 % reported in the previous chapter. From the density matrix we calculated a fidelity compared to the ideal NOON state of 0.95 $\pm$0.01, a purity of 0.94 $\pm$0.01 and most importantly a lower bound on the entanglement of 0.92 $\pm$0.01. The plotted density matrix and these values were obtained by a single tomography measurement on which we, as explained before, simulated Poissonian noise for a thousand iterations. For the distribution of results for 10 separate measurements Fidelities of 0.93 $\pm$0.02, purities of 0.91 $\pm$0.05 and entanglements of 0.89 $\pm$0.04 were obtained. This shows the stability of the system, only small extra inaccuracies are introduced from one measurement to the other. While each tomography in the photonic case was obtained with 9 measurements of 1 second, the plasmonic case takes considerably longer, therefore phase stability of the interferometer will be discussed for the plasmonic case. To show that the interference creates entanglement, the beam splitter is taken out of the set-up. This way, the two single photons are superimposed on the PBS with opposite polarizations, we expect the $|11\rangle$ state. The result in figure 5.7 (b) shows a very close experimental reconstruction. Ten consecutive measurements result in an distribution of Fidelity compared to the expected state of 0.93 $\pm$0.02, a state purity of 0.81 $\pm$0.02 and an entanglement of 0.05 $\pm$0.01. The measurement scheme reliably reconstructs the expected state and it is clear that the interference changes the state from negligible entanglement (in the number degree of freedom) to an almost fully entangled state. At last, we show that the NOON state can be distinguished from the mixed $(|20\rangle\langle 20| + |02\rangle\langle 02|)/\sqrt{2}$ state. Measurement (c) is the tomography result with delay-line 2 outside of the interferences, we expect no coherence between the $|20\rangle$ and the $|02\rangle$ component, the state becomes the mixed state and this is also shown in the measurement. An entanglement of 0.16 $\pm$ 0.05 and a Fidelity of 0.95 $\pm$ 0.01 (compared to the expected mixed state) are obtained. Due to the long coherence length, as visible in the interferences, the measurement wasn't taken completely out of coherence, which explains the residual entanglement in this measurement. It does show the possibility of detecting decoherence on our state.

Ideally, we would want to reconstruct the output state when delay-line 1 is out of its symmetry position. Unfortunately, the set-up only

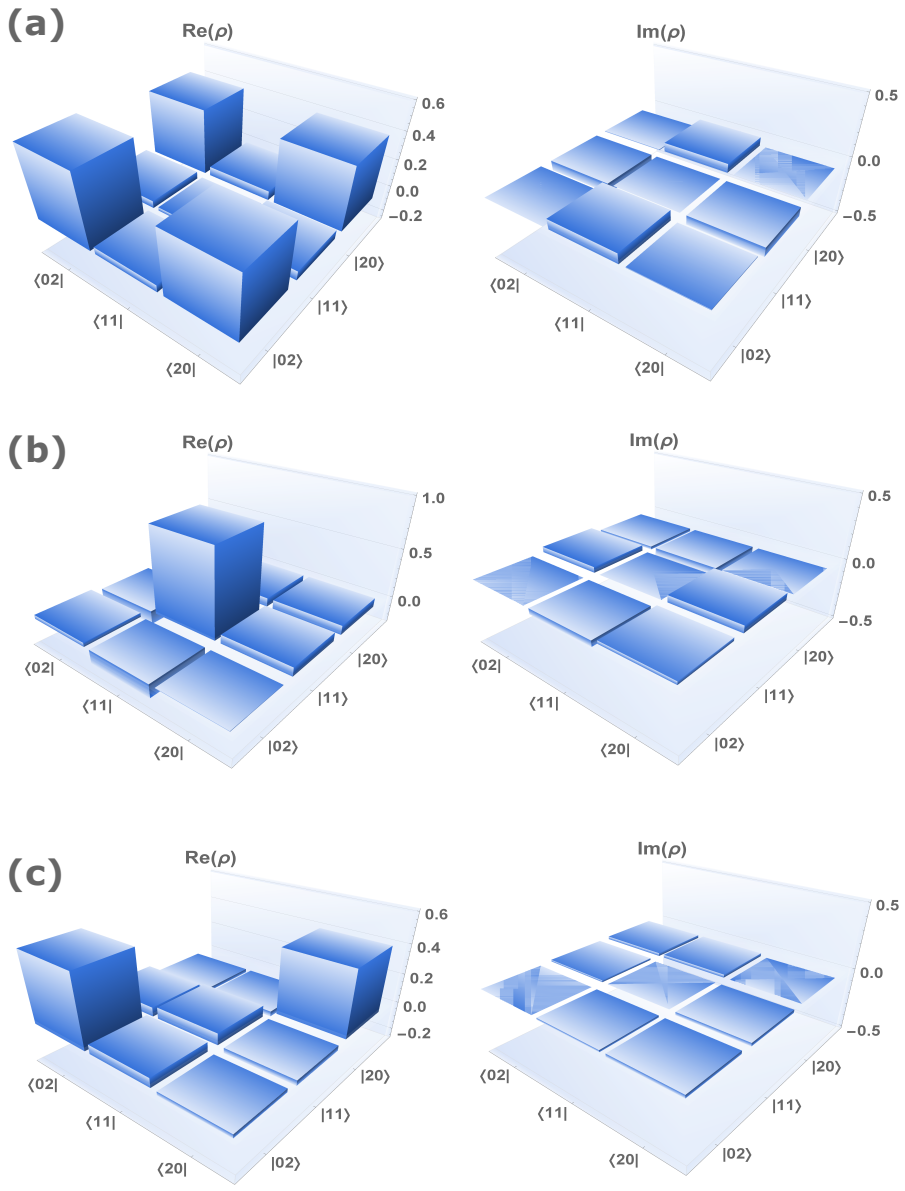


Figure 5.4: **(a)**, Measurement of the NOON state. Populations: 0.52, 0.03 and 0.45. Fidelity: 0.95 ±, purity: 0.94 ± 0.01, entanglement: 0.92 ±0.01. **(b)**, Measurement of the $|11\rangle$ state. Populations: 0.04, 0.87 and 0.09. Fidelity: 0.93 ± 0.01, purity: 0.82 ± 0.02, entanglement: 0.05 ± 0.02. **(c)**, Measurement of the mixed NOON state. Populations: 0.48, 0.08 and 0.44. Fidelity: 0.96 ± 0.01, purity: 0.45 ± 0.01, entanglement: 0.11 ± 0.06.

works when both photons are indistinguishable. A quick calculation with two distinguishable photons A and B starting before the beam splitter shows:

$$\begin{aligned} |H\rangle_A |H\rangle_B &\xrightarrow{BS} \frac{1}{2}(|H\rangle_A + i|H\rangle_A) \otimes (|H\rangle_B - i|H\rangle_B) \\ &\xrightarrow{HWP} \frac{1}{2}(|H\rangle_A + i|V\rangle_A) \otimes (|H\rangle_B - i|V\rangle_B) \\ &\xrightarrow{PBS} \frac{1}{2}(|H\rangle_A + i|V\rangle_A) \otimes (|H\rangle_B - i|V\rangle_B) \end{aligned} \tag{5.18}$$

When applying the 9 different angle combinations and the polarizing beam splitter of the tomography on the two separate photons in the cross product shown in equation 5.18, we will get the same values for B_1 to B_9 (calculated by $\langle \hat{n}_A \rangle \langle \hat{n}_B \rangle$) as for the NOON state with indistinguishable photons shown before. The breakdown of this scheme with distinguishable photons is discussed more in depth publications by Adamson *et al.* [217, 218]. A more extended tomography scheme delivering a 4 by 4 density matrix with a basis $\{|A_V B_V\rangle, |A_V B_H\rangle, |A_H B_V\rangle, |A_H B_H\rangle\}$ by also making correlated measurements on the vertical polarization could potentially have solved this problem.

5.3.2 *Plasmonic results*

To perform the tomography measurement with the plasmonic beam splitter, the set-up is again combined with a microscopy set-up. The two photons coming from the SPDC set-up are again focused on the two input gratings of the plasmonic beam splitter described in the previous chapter. The two input and two output beams are separated from each other with the same reflective pyramid. The two output beams coming from the pyramid mirror are this time recombined on a polarizing beam splitter before being coupled into the polarization maintaining fibre with the same imaging combination of a biconvex lens with focal length = 1000 mm and a 20x objective. Half wave plates before and after the PMF again ensure that the reflected and transmitted beam from PBS1 arrive at the tomography set-up as the vertical and horizontal polarization respectively. In the plasmonic set-up the PMF has the added importance of cleaning up the spatial modes of the light coming out of the output gratings of the plasmonic sample; the single mode nature of the fibre ensures that there is no spatial information to distinguish out of which gratings the light was scattered. The photons scattered out of the beam splitter are not perfectly

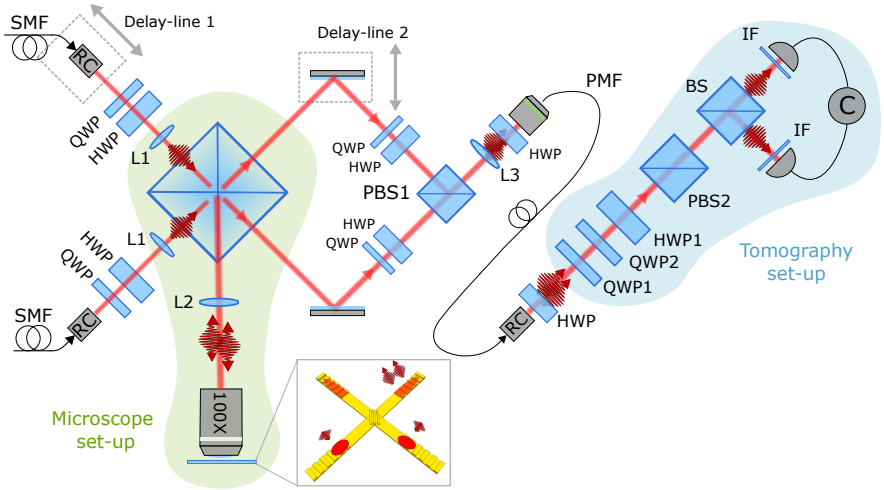


Figure 5.5: The same microscopy set-up from the previous chapter is used for the plasmonic tomography set-up, but here the output beams are recombined on a polarizing beam splitter (PBS1) before being coupled into a fibre by a combination of a lens (lens L3, f = 1000 mm) and objective (Olympus MPLN 20X).

linearly polarized, so to optimize the photons being transmitted and reflected on PBS1, a quarter and half wave plate were added on both paths. Optimizing the polarization and the coupling of both paths into the fibre resulted in a final count rate of 2-3 coincidence counts per second for each polarization separately, when the set-up is not on the symmetry position. As expected, this is even lower than the count rate in the final results of last chapter. A first rough temporal alignment is again achieved by a combination of finding the symmetry position of delay-line 1 with a HOM interference on the pellicle beam splitter (BS1 in figure 4.10) and a interference measurement with the pulsed laser between that beam splitter and the plasmonic structure. After this, delay-line 1 is scanned to obtain the same measurement as shown in figure 5.3.

After aligning delay-line 1, the same scan as performed with delay-line 2 for the photonic tomography set-up -resulting in the measurement shown in figure 5.3 (b) - was done with delay-line 3. Scanning the central part of the interference with steps of only 25 nm results in the pattern shown in figure 5.6. The pattern of the coincidence counts looks at first surprising with a big and intermediate small peak in each period. Ignoring the normalization constants in equation 2.24 and adding a time delay in output mode 3, we get the following

output state of the surviving photon pairs after the plasmonic beam splitter:

$$\left[-t^* r^* ((\hat{a}_2^\dagger)^2 + e^{i2\delta t}(\hat{a}_3^\dagger)^2) + (t^{*2} + r^{*2}) e^{i\delta t} \hat{a}_2^\dagger \hat{a}_3^\dagger\right] |00\rangle \tag{5.19}$$

Taking into account the rest of the set-up, including the transformation matrix with angles $\theta = \frac{\pi}{4}$ and $\phi = 0$ in equation 5.8, the coincidence rate is given by:

$$B = \left| \frac{t^* r^*}{2}(1 + e^{i2\delta t}) - \frac{(t^{*2} + r^{*2})}{\sqrt{2}} e^{i\delta t} \right|^2 \tag{5.20}$$

For a perfect HOM interference, the second component is 0 and the result would be oscillations with a period of half a wavelength, a well known effect of 2-photon NOON states. In the case of our plasmonic beam splitter, the interference is not perfect, there is a $|11\rangle$ component oscillating with the same period as the single counts. This interferes with the NOON component and increases the coincidence counts at half of the peaks and reduces it on the other half. Due to the high losses in the system, most of the measured single photons in the single counts (obtained by taking the count rate of one of the two detectors) are not part of a photon pair any more. The signal shown in the figure is the sum of the single photon interferences from photons coming from both input arms of the plasmonic beam splitter. In a beam splitter with a $\frac{\pi}{2}$ phase shift, the oscillations of the photons coming from input 1 are out of phase with those of input 2, resulting in a constant single count rate of the scan. This is almost the case for the measurement in the photonic set-up, shown in figure 5.3. A visual fit for the coincidence and single counts here shows a phase shift of 1.18, in good agreement with the 1.21 $\pm$0.01 value obtained in section 4.1.4.

The low count rates means that extra care has to be taken to make the set-up stable over the course of a tomography measurement. Figure 5.6 (b) shows the result of a stability measurement, with delay-line 1 on the HOM interference, delay-line 3 is positioned on the slope of oscillations shown in (a). The first 50 points are each coincidence counts integrated over 1 minute while the delay lines are not moving, considerable phase drift in the set-up would result in oscillations of the signal over time that exceed what is expected from Poissonian noise. We can see that the set-up is stable over an extended period of time. Between every measurement of the last 10 points, delay-line 3 made a small step, this shows that the system was indeed positioned on

the slope of an interference fringe. The difference between the maximum and minimum value is 55. With a peak value for the oscillation of 350, a linear estimate indicates that the phase did not drift more than $\pi/7$ during the period of the measurement. Taking into account that the two-photon component has a full period over 404 nm, this means a stability of the optical path difference between the vertical and horizontal mode of around 25 nm. To achieve this level of stability, several improvements turned out to be necessary during the building process, fortunately no active stabilizing techniques were needed. Naturally, the path length where both beams are separate (from the pyramid mirror to PBS1) was kept at a minimum. Monitoring the temperature together with stability measurements showed the necessity of keeping it stable within 0.1-0.2 °C. Luckily this was possible with a combination of air conditioning in the lab, aluminium foil on the windows to block sunlight, and boxing in the set-up. The latter was also crucial to minimize the airflow. Finally, high stability Polaris™ mirror mounts in combination with 1" posts were used. Even though the modes travel along the same optical path in the PMF, temperature drift around this fibre did result in phase drift of the total set-up, meaning that the also the fibre had to be kept inside the box of the set-up.

The final results are shown in figure 5.7, for the coherent state in (a) and the mixed state in (b). Each of the 9 measurements for the full reconstruction were 240 seconds of integration time. Similar results were obtained by summing the measurements of 5 consecutive full scans of 60 seconds integration time for each angle combination. The lower bound for the entanglement of 0.77 $\pm$0.04 clearly shows the entanglement generated in the plasmonic beam splitter. The $|11\rangle\langle 11|$ population is 0.19, equivalent to a 0.62 visibility of the Hong-Ou-Mandel interference in good agreement with the value obtained in the previous chapter. The coherences are mainly located in the imaginary part of the density matrix, this is purely due to the phase difference between the different components and is an outcome of not positioning delay-line 3 at a 0 phase difference as done for the photonic case.

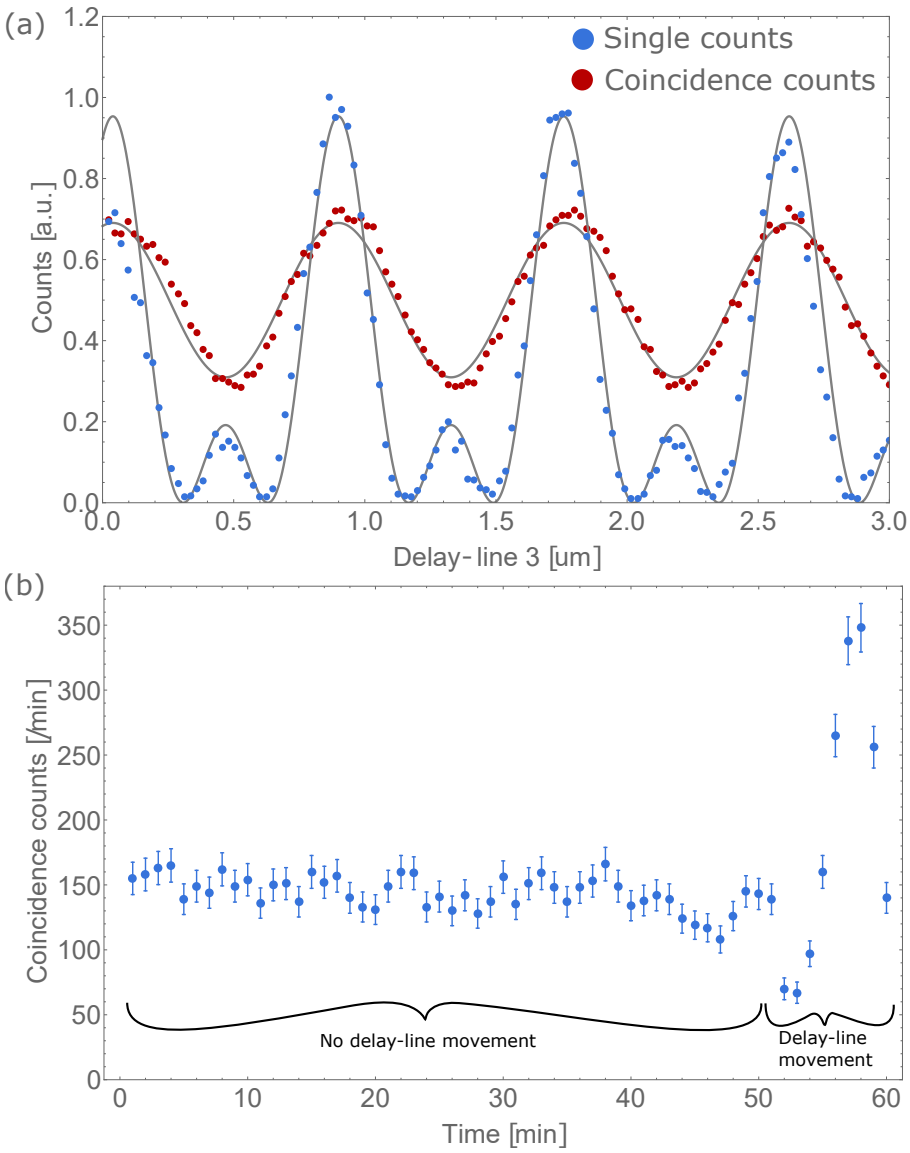


Figure 5.6: **a)**, Scan of the interference fringes in the interferometer going from the plasmonic beam splitter up to PBS2, both the single and coincidence counts. **b)**, Phase stability measurement for the interferometer going from the plasmonic beam splitter up to PBS2. Each point is one minute of measurements, with the error bars calculated under the assumption of Poissonian noise. Last ten points are obtained while taking steps with delay-line 3, to affirm the interferometer was positioned in a region of interference fringes.

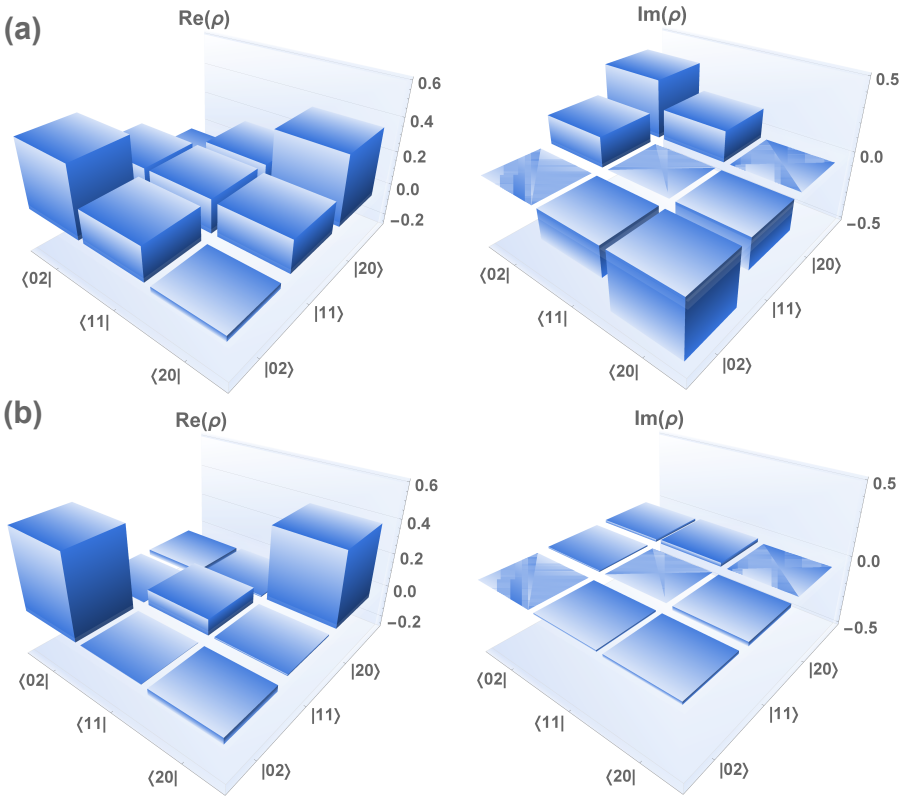


Figure 5.7: **(a)**, Measurement of the NOON state. Populations: 0.41, 0.19 and 0.40. Fidelity: 0.80 ± 0.02, purity: 0.96 ± 0.04, entanglement: 0.77 ±0.04. **(b)**, Measurement of the mixed NOON state. Populations: 0.47, 0.1 and 0.43. Fidelity: 0.94 ± 0.01, purity: 0.46 ± 0.04, entanglement: 0.22 ± 0.12.

CONCLUSION

Quantum optics has experienced strong progress towards integrated devices on a chip. Quantum computation, quantum communication and quantum metrology could all be pushed into real-life applications with the help of integrated photonics.

Plasmonics promises a lot of interesting directions in this context with its miniaturization below the micrometer scale and the proven potential for extremely fast and strong interaction between quantum emitters and plasmonic modes. For this it is important that the quantum nature of SPPs and the survival of quantum coherence is investigated in-depth. In this thesis we experimentally probed two specific quantum effects: two-SPP interference and the entanglement generated in this interference. The two-SPP interference is the plasmonic version of the seminal Hong-Ou-Mandel interference in which two photons arriving at the two input ports of the beam splitter always coalesce together into one of the two output ports. The disappearing chance of having one photon at each output was measured by correlating the detectors at the two output modes of the beam splitter. We showed a visibility of the interference effect of 0.58 ± 0.01. This is worse than the often achieved visibility of over 0.9 in other structures. The main reason is the normally ignored phase difference between reflection and transmission in the beam splitter. In a lossless beam splitter unitarity of the transformation of the in- and output modes imposes a $\frac{\pi}{2}$ phase difference, which is needed for a perfect interference. The plasmonic beam splitter is lossy, which can alter this phase difference. We experimentally measured a value of 1.21, deviating from $\frac{\pi}{2}$. By varying the structural parameters of plasmonic beam splitters, it is possible to tune this phase; potentially opening up new effects to investigate and harness. The visibility is still reliably above the classical limit of 0.5 though, which shows that SPPs behave as bosons.

Measuring the correlated counts at the outputs of the beam splitter does not directly prove entanglement in the output state. Decoherence in the plasmonic waveguide could for example change the ideal output state $\frac{1}{\sqrt{2}}(|20\rangle + |02\rangle)$ to a mixed state $\frac{1}{2}(|20\rangle\langle 20| + |02\rangle\langle 02|)$. We

used quantum state tomography to probe the entanglement, to our knowledge for the first time on a HOM output state. The two output modes of the beam splitter are given perpendicular linear polarizations and combined into one single spatial mode on a polarizing beam splitter. Polarization based quantum state tomography was performed on this single-mode state with polarization correlations. With the reconstructed density matrix we showed that the interference generates entanglement in the plasmonic structure. The calculated entanglement of formation puts a lower bound on the entanglement of 0.77 $\pm$ 0.04. Generation of entanglement in a plasmonic structure has, to our knowledge, not been shown before and opens up further investigations for quantum applications.

We have shown that using quantum metrology techniques with plasmonic structures is an interesting route to harness the power of quantum effects in a plasmonic setting. Plasmonic sensing was the first application in the field of plasmonics and has since then developed into many directions. Many approaches, like the surface plasmon resonance sensor, have been optimized close to the limit of what is possible with classical light. It is thus interesting to investigate if quantum states of light can deliver enhancements, despite the loss in the sensing schemes. We showed that with the right states and measuring scheme quantum metrology could deliver sensitivities with plasmonic structures out of reach with classical light.

BIBLIOGRAPHY

[1] G. Di Martino et al. "Observation of quantum interference in the plasmonic Hong-Ou-Mandel effect." In: *Physical Review Applied* 1.3 (2014), pp. 1–6. DOI: 10.1103/PhysRevApplied.1.034004. arXiv: 1402.0813v1.

[2] M. S. Tame et al. "Quantum plasmonics." In: *Nature Physics* 9.6 (2013), pp. 329–340. DOI: 10.1038/nphys2615.

[3] C. Lee et al. "Quantum plasmonic sensing: beyond the shot-noise and diffraction limit." In: *ACS Photonics* 3 (2016), pp. 992–999. DOI: 10.1021/acsphotonics.6b00082. arXiv: 1601.00017.

[4] J. Homola. "Surface plasmon resonance sensors for detection of chemical and biological species." In: *Chemical reviews* 108.2 (2008), pp. 462–493. DOI: 10.1021/cr068107d.

[5] R. P. Feynman, R. B. Leighton, and M. Sands. *The Feynman Lectures on Physics*. Addison–Wesley, 1964.

[6] P. G. Kwiat. "Nonclassical effects from spontaneous parametric down-conversion: Adventures in quantum wonderland." PhD thesis. University of California, 1993, p. 299.

[7] E. Schrödinger. "Discussion of Probability Relations between Separated Systems." In: *Mathematical Proceedings of the Cambridge Philosophical Society* 31.4 (1935), pp. 555–563. DOI: 10.1017/S0305004100013554.

[8] A. Einstein, B. Podolsky, and N. Rosen. "Can Quantum-Mechanical Description of Physical Reality Be Considered Complete?" In: *Physical Review* 47 (1935), pp. 2–5. DOI: 10.1103/PhysRev.47.777.

[9] J. S. Bell. "The Einstein Podolsky Rosen Paradox and Local Hidden—Variables Theories." In: *Physics* 1.3 (1964), pp. 195–200. DOI: 10.1002/prop.19800281202. arXiv: 1409.4807.

[10] J. P. Dowling and G. J. Milburn. "Quantum technology: the second quantum revolution." In: *Philosophical transactions. Series A, Mathematical, physical, and engineering sciences* 361.1809

(2003), pp. 1655–1674. DOI: 10.1098/rsta.2003.1227. arXiv: 0206091 [quant-ph].

[11] R. P. Feynman. "Simulating physics with computers." In: *International Journal of Theoretical Physics* 21.6-7 (1982), pp. 467–488. DOI: 10.1007/BF02650179. arXiv: 9508027 [quant-ph].

[12] D. Deutsch. "Quantum theor, the Church-Turing principle and the universal quantum computer." In: *Proceedings of the Royal Society of London A* 400.July 1984 (1985), pp. 97–117. DOI: 10.1098/rspa.1983.0054.

[13] C. M. Caves. "Quantum mechanical noise in an interferometer." In: *Phys. Rev. D* 23.8 (1981), p. 1693.

[14] P. Shor. "Polynomial-Time Algorithms for Prime Factorization and Discrete Logarithms on a Quantum Computer." In: *SIAM Journal on Computing* 26.5 (1997), pp. 1484–1509. DOI: 10.1137/S0097539795293172. arXiv: 9508027 [quant-ph].

[15] C. Monroe et al. "Demonstartion of a Fundamental Quantum Logic Gate." In: *Physical Review Letters* 75.25 (1995), pp. 4714–4717. DOI: 10.1103/PhysRevLett.75.4714.

[16] P. R. Tapster, J. G. Rarity, and P. C. M. Owens. "Violation of bell's inequality over 4 km of optical fiber." In: *Physical Review Letters* 73.14 (1994), pp. 1923–1926. DOI: 10.1103/PhysRevLett.73.1923.

[17] W. Tittel et al. "Violation of Bell Inequalities by Photons More Than 10 km Apart." In: *Physical Review Letters* 81.17 (1998), pp. 3563–3566. DOI: 10.1103/PhysRevLett.81.3563. arXiv: 9806043 [quant-ph].

[18] M. Giustina et al. "Significant-Loophole-Free Test of Bell's Theorem with Entangled Photons." In: *Physical Review Letters* 115.25 (2015), pp. 1–7. DOI: 10.1103/PhysRevLett.115.250401. arXiv: 1511.03190.

[19] J. I. Cirac and P. Zoller. "Quantum computations with cold trapped ions." In: *Physical Review Letters* 74.20 (1995), pp. 4091–4094. DOI: 10.1103/PhysRevLett.74.4091. arXiv: 0305129 [quant-ph].

[20] M. H. Anderson et al. "Observation of Bose-Einstein Condensation in a Dilute Atomic Vapor." In: *Science* 269.5221 (1995), pp. 198–201. DOI: 10.1126/science.269.5221.198. arXiv: arXiv:1011.1669v3.

[21] E Knill, R Laflamme, and G. Milburn. "A scheme for efficient quantum computation with linear optics." In: *nature* 409.January (2001).

[22] J Silverstone et al. "Silicon Quantum Photonics." In: *IEEE JOURNAL OF SELECTED TOPICS IN QUANTUM ELECTRONICS* 22.6 (2004), pp. 41–82. DOI: 10.1002/9780470994535.

[23] P. Lodahl et al. "Controlling the dynamics of spontaneous emission from quantum dots by photonic crystals." In: *Nature* 430.7000 (2004), pp. 654–657. DOI: 10.1038/nature02772.

[24] K Hennessy et al. "Quantum nature of a strongly-coupled single quantum dot-cavity system." In: *Nature* 445.February (2007), p. 896. DOI: 10.1038/nature05586. arXiv: 0610034 [quant-ph].

[25] S. Noda, M. Fujita, and T. Asano. "Spontaneous-emission control by photonic crystals and nanocavities." In: *Nature Photonics* 1.8 (2007), pp. 449–458. DOI: 10.1038/nphoton.2007.141.

[26] M. Pelton. "Modified spontaneous emission in nanophotonic structures." In: *Nature Photonics* 9.7 (2015), pp. 427–435. DOI: 10.1038/nphoton.2015.103.

[27] K. A. Willets and R. P. Van Duyne. "Localized surface plasmon resonance spectroscopy and sensing." In: *Annual review of physical chemistry* 58 (2007), pp. 267–297. DOI: 10.1146/annurev.physchem.58.032806.104607.

[28] S. a. Maier. *Plasmonics: Fundamentals and Applications*. Springer, 2007, p. 223.

[29] R. H. Ritchie and H. B. Eldridge. "Optical emission from irradiated foils. II." In: *Physical Review* 126.6 (1962), pp. 1947–1952. DOI: 10.1103/PhysRev.126.1947.

[30] A Otto. "Theory of Plasmon Excitation in Thin Films by Electrons of Non-Normal Incidence." In: *Phys. Stat. Sol.* 22 (1967), pp. 401–406.

[31] A. Otto. "Excitation of nonradiative surface plasma waves in silver by the method of frustrated total reflection." In: *Zeitschrift fur Physik* 216.4 (1968), pp. 398–410. DOI: 10.1007/BF01391532.

[32] D. Pines. *Elementary Excitations in Solids*. W. A. Benjamin, Inc., 1964, p. 299.

[33] J. S. Fakonas et al. "Two-plasmon quantum interference." In: *Nature Photonics* 8.4 (2014), pp. 317–320. DOI: 10.1038/nphoton.2014.40.

[34] Y.-J. Cai et al. "High-Visibility On-Chip Quantum Interference of Single Surface Plasmons." In: *Physical Review Applied* 2.1 (2014), p. 014004. DOI: 10.1103/PhysRevApplied.2.014004.

[35] G. Fujii, D. Fukuda, and S. Inoue. "Direct observation of bosonic quantum interference of surface plasmon polaritons using photon-number-resolving detectors." In: *Physical Review B* 085430 (2014), pp. 1–5. DOI: 10.1103/PhysRevB.90.085430.

[36] R. W. Heeres, L. P. Kouwenhoven, and V. Zwiller. "Quantum interference in plasmonic circuits." In: *Nature Nanotechnology* 8.10 (2013), pp. 719–722. DOI: 10.1038/nnano.2013.150. arXiv: 1309.6942.

[37] C. K. Hong, Z. Y. Ou, and L. Mandel. "Measurement of subpicosecond time intervals between two photons by interference." In: *Physical Review Letters* 59 (1987), pp. 2044–2046. DOI: 10.1103/PhysRevLett.59.2044.

[38] R. Loudon. "Fermion and boson beam-splitter statistics." In: *Physical Review A* 58.6 (1998), pp. 4904–4909. DOI: 10.1103/PhysRevA.58.4904.

[39] E Altewischer, M. P. V. Exter, and J. P. Woerdman. "Plasmon-assisted transmission of entangled photons." In: *Nature* 418.July (2002), pp. 304 –306.

[40] G. Di Martino. "Quantum Plasmonics: From Quantum Statistics to Quantum Interferences." PhD thesis. Imperial College London, 2014, p. 128.

[41] L. Novotny and B. Hecht. *Principles of Nano-optics*. 2012, p. 564.

[42] M. A. Ordal et al. "Optical properties of fourteen metals in the infrared and far infrared: Al, Co, Cu, Au, Fe, Pb, Mo, Ni, Pd, Pt, Ag, Ti, V, and W." In: *Applied Optics* 24.24 (1985), pp. 4493–4499. DOI: 10.1364/AO.24.004493.

[43] K. M. McPeak et al. "Plasmonic films can easily be better: Rules and recipes." In: *ACS Photonics* 2.3 (2015), pp. 326–333. DOI: 10.1021/ph5004237. arXiv: 1603.02132.

[44] C. Haffner et al. "All-plasmonic Mach–Zehnder modulator enabling optical high-speed communication at the microscale." In: *Nature Photonics* 9.8 (2015), pp. 525–528. DOI: 10.1038/nphoton.2015.127.

[45] J. J. Burke, G. I. Stegeman, and T. Tamir. "Surface-polariton-like waves guided by thin, lossy metal films." In: *Physical Review B* 33.8 (1986), pp. 5186–5201. DOI: 10.1103/PhysRevB.33.5186. arXiv: arXiv:1011.1669v3.

[46] B. Prade, J. Y. Vinet, and A Mysyrowicz. "Guiden optical waves in planar heterostructures with negative dielectric constant." In: *Physical Reivvew B* 44.24 (1991).

[47] R. N. C. Pfeifer et al. "Colloquium: Momentum of an electromagnetic wave in dielectric media." In: *Reviews of Modern Physics* 79.4 (2007), pp. 1197–1216. DOI: 10.1103/RevModPhys.79.1197. arXiv: 0710.0461v2.

[48] J. Hu. *UD MSEG 667 "Nanophotonics: Materials and devices"*.

[49] W. L. Barnes et al. "Physical origin of photonic energy gaps in the propagation of surface plasmons on gratings." In: 54.9 (1996), pp. 6227–6244.

[50] W. L. Barnes et al. "Photonic gaps in the dispersion of surface plasmons on gratings." In: *Physical Review B* 51.16 (1995), pp. 11164–11167. DOI: 10.1103/PhysRevB.51.11164.

[51] H. Ditlbacher et al. "Efficiency of local light-plasmon coupling." In: *Applied Physics Letters* 83.18 (2003), pp. 3665–3667. DOI: 10.1063/1.1625107.

[52] I. Radko et al. "Efficiency of local surface plasmon polariton excitation on ridges." In: *Physical Review B* 78.11 (2008), p. 115115. DOI: 10.1103/PhysRevB.78.115115.

[53] J. D. Jackson. *Classical Electrodynamics*. 3rd. John Wiley & Sons, Inc., 1999, p. 834.

[54] G. Leveque and O. J. F. Martin. "Optimization of finite diffraction gratings for the excitation of surface plasmons." In: *Journal of Applied Physics* 100.12 (2006), p. 124301. DOI: 10.1063/1.2401025.

[55] P. Lalanne et al. "A microscopic view of the electromagnetic properties of sub-?? metallic surfaces." In: *Surface Science Reports* 64.10 (2009), pp. 453–469. DOI: 10.1016/j.surfrep.2009.07.003.

[56] H. Liu and P. Lalanne. "Light scattering by metallic surfaces with subwavelength patterns." In: *Physical Review B - Condensed Matter and Materials Physics* 82.11 (2010), pp. 1–9. DOI: 10.1103/PhysRevB.82.115418.

[57] G. Li et al. "Theory of the scattering of light and surface plasmon polaritons by finite-size subwavelength metallic defects via field decomposition." In: *New Journal of Physics* 13 (2011). DOI: 10.1088/1367-2630/13/7/073045.

[58] A. Baron et al. "Compact antenna for efficient and unidirectional launching and decoupling of surface plasmons." In: *Nano Letters* 11.10 (2011), pp. 4207–4212. DOI: 10.1021/nl202135w. arXiv: 1109.2032.

[59] Z. Lei and T. Yang. "Gap plasmon resonator arrays for unidirectional launching and shaping of surface plasmon polaritons." In: *Applied Physics Letters* 108.16 (2016). DOI: 10.1063/1.4947431.

[60] J. Lin et al. "Polarization-Controlled Tunable Directional Coupling of Surface Plasmon Polaritons." In: *Science* 340 (2013), pp. 331–334. DOI: 10.1126/science.1233746. arXiv: arXiv:1011.1669v3.

[61] A. Pors et al. "Efficient unidirectional polarization-controlled excitation of surface plasmon polaritons." In: *Light: Science & Applications* 3.8 (2014), p. 6. DOI: 10.1038/lsa.2014.78.

[62] D. Chang et al. "Quantum Optics with Surface Plasmons." In: *Physical Review Letters* 97.5 (2006), p. 053002. DOI: 10.1103/PhysRevLett.97.053002.

[63] C. L. C. Smith et al. "Gap and channeled plasmons in tapered grooves: a review." In: *Nanoscale* 7.21 (2015), pp. 9355–86. DOI: 10.1039/c5nr01282a. arXiv: 1503.00554.

[64] L. Chen, J. Shakya, and M. Lipson. "Metal slot waveguide with silicon for deep subwavelength confinement and on-chip integration." In: *Conference on Lasers and Electro-Optics and 2006 Quantum Electronics and Laser Science Conference, CLEO/QELS*

2006 31.14 (2006), pp. 2133–2135. DOI: 10.1109/CLEO.2006.4628937.

[65] R. M. Briggs et al. "Efficient coupling between dielectric-loaded plasmonic and silicon photonic waveguides." In: *Nano Letters* 10.12 (2010), pp. 4851–4857. DOI: 10.1021/nl1024529.

[66] J. Tian et al. "Broadband high-efficiency surface-plasmon-polariton coupler with silicon-metal interface." In: *Applied Physics Letters* 95.1 (2009), pp. 1–4. DOI: 10.1063/1.3168653.

[67] M. Ono et al. "Deep-subwavelength plasmonic mode converter with large size reduction for Si-wire waveguide." In: *Optica* 3.9 (2016), p. 999. DOI: 10.1364/OPTICA.3.000999.

[68] S. P. Burgos et al. "Synthesis and characterization of plasmonic resonant guided wave networks." In: *Nano Letters* 14.6 (2014), pp. 3284–3292. DOI: 10.1021/nl500694c.

[69] R. W. Wood. "On a remarkable case of unseen distribution of light in a diffraction grating spectrum." In: *Phylosophical Magazine Series* 269 (1902). DOI: 10.1080/14786440209462857.

[70] D. Pines. "Collective energy losses in solids." In: *Reviews of Modern Physics* 28.3 (1956), pp. 184–198. DOI: 10.1103/RevModPhys.28.184.

[71] S. L. Cunningham, A. A. Maradudin, and R. F. Wallis. "Effect of a charge layer on the surface-plasmon polariton disperion curve." In: *Physical Review B* 10.8 (1974).

[72] M. L. Brongersma. "Introductory lecture: nanoplasmonics." In: *Faraday Discuss.* 178 (2015), pp. 9–36. DOI: 10.1039/C5FD90020D.

[73] M. Fleischmann, P. Hendra, and A. McQuillan. "Raman spectra of pyridine adsorbed at a silver electrode." In: *Chemical Physics Letters* 26.2 (1974), pp. 163–166. DOI: 10.1016/0009-2614(74)85388-1. arXiv: arXiv:1011.1669v3.

[74] M. Moskovits. "Surface roughness and the enhanced intensity of Raman scattering by molecules adsorbed on metals." In: *The Journal of Chemical Physics* 69.9 (1978), p. 4159. DOI: 10.1063/1.437095.

[75] K Kneipp et al. "Single molecule detection using surface-enhanced Raman scattering (SERS)." In: *Physical review ...* 78.9 (1997), pp. 1667–1670. DOI: 10.1103/PhysRevLett.78.1667.

[76] J. Homola, S. S. Yee, and G. Gauglitz. "Surface plasmon resonance sensors: review." In: *Sensors and Actuators B* 54 (1999), pp. 3–15. DOI: 10.1016/S0925-4005(98)00321-9.

[77] B. Liedberg, C. Nylander, and I. Lunström. "Surface plasmon resonance for gas detection and biosensing." In: *Sensors and Actuators* 4.C (1983), pp. 299–304. DOI: 10.1016/0250-6874(83)85036-7.

[78] J Takahara et al. "Guiding of a one-dimensional optical beam with nanometer diameter." In: *Optics letters* 22.7 (1997), pp. 475–477. DOI: 10.1364/OL.22.000475.

[79] K. Nerkararyan. "Superfocusing of a surface polariton in a wedge-like structure." In: *Physics Letters A* 237.1-2 (1997), pp. 103–105. DOI: 10.1016/S0375-9601(97)00722-6.

[80] J.-c. Weeber et al. "Near-field observation of surface plasmon polariton propagation on thin metal stripes." In: *Physical Review B* 64.4 (2001), p. 045411. DOI: 10.1103/PhysRevB.64.045411.

[81] S. A. Maier et al. "Local detection of electromagnetic energy transport below the diffraction limit in metal nanoparticle plasmon waveguides." In: *Nature Materials* 2.4 (2003), pp. 229–232. DOI: 10.1038/nmat852. arXiv: 0403600v1 [arXiv:cond-mat].

[82] S. I. Bozhevolnyi et al. *Photonic bandgap structures for long-range surface plasmon polaritons*. 2005. DOI: 10.1016/j.optcom.2005.02.027.

[83] S. I. Bozhevolnyi. "Effective-index modeling of channel plasmon polaritons." In: 14.20 (2006), pp. 9467–9476.

[84] D. F. P. Pile et al. "Theoretical and experimental investigation of strongly localized plasmons on triangular metal wedges for subwavelength waveguiding." In: *Applied Physics Letters* 87.6 (2005), pp. 1–4. DOI: 10.1063/1.1991990.

[85] C. L. C. Smith et al. "Efficient excitation of channel plasmons in tailored, UV-lithography-defined V-grooves." In: *Nano Letters* 14 (2014), pp. 1659–1664.

[86] S. J. P. Kress et al. "Wedge Waveguides and Resonators for Quantum Plasmonics." In: *Nano Letters* 15.9 (2015), pp. 6267–6275. DOI: 10.1021/acs.nanolett.5b03051.

[87] R. F. Oulton et al. "Confinement and propagation characteristics of subwavelength plasmonic modes." In: *New Journal of Physics* 10 (2008). DOI: 10.1088/1367-2630/10/10/105018.

[88] G. Grynberg, A. Aspect, and C. Fabre. *Introduction to Quantum Optics: From the Semi-classical Approach to Quantized Light*. Cambridge University Press, 2010, p. 696.

[89] D. F. Walls and G. Milburn. *Quantum Optics*. Springer, 2008, p. 425.

[90] a. C. Judge et al. "Canonical quantization of macroscopic electrodynamics in a linear, inhomogeneous magnetoelectric medium." In: *Physical Review A* 87.3 (2013), p. 033824. DOI: 10.1103/PhysRevA.87.033824.

[91] A. Archambault et al. "Quantum theory of spontaneous and stimulated emission of surface plasmons." In: *Physical Review B - Condensed Matter and Materials Physics* 82.3 (2010), pp. 1–10. DOI: 10.1103/PhysRevB.82.035411. arXiv: 1004.0135.

[92] M. S. Tame et al. "Quantum plasmonics." In: *Nature Physics* 9.6 (2013), pp. 329–340. DOI: 10.1038/nphys2615. arXiv: 1312.6806.

[93] D. Ballester et al. "Long-range surface-plasmon-polariton excitation at the quantum level." In: *Physical Review A - Atomic, Molecular, and Optical Physics* 79.5 (2009), pp. 1–10. DOI: 10.1103/PhysRevA.79.053845. arXiv: arXiv:0901.3972v2.

[94] M. Lewenstein, A. Sanpera, and M. Pospiech. *Quantum optics: an introduction*. 2003, p. 86.

[95] R Glauber. "The Quantum Theory of Optical Coherence." In: *Physical Review* 130.6 (1963), pp. 2529–2539. DOI: 10.1103/PhysRev.130.2529.

[96] R. Hanbury Brown and R. Q. Twiss. "A Test of a New Type of Stellar Interferometer on Sirius." In: *Nature* 178.4541 (1956), pp. 1046–1048. DOI: 10.1038/1781046a0.

[97] R. Loudon. "Non-classical effects in the statistical properties of light." In: *Reports on progress in physics. Physical Society (Great Britain)* 43.7 (1980).

[98] L. Mandel and E. Wolf. *Optical Coherence and Quantum Optics*. Cambridge University Press, 1995, p. 1194.

[99] S. M. Barnett et al. "Quantum optics of lossy beam splitters." In: 57.3 (1998), pp. 2134–2145.

[100] Y. Shih et al. "Entangled biphoton source - property and preparation." In: *Reports on Progress in Physics* 66.6 (2003), pp. 1009–1044. DOI: 10.1088/0034-4885/66/6/203.

[101] R. Ghosh and L. Mandel. "Observation of nonclassical effects in the interference of two photons." In: *Physical Review Letters* 59 (1987), pp. 1903–1905. DOI: 10.1103/PhysRevLett.59.1903.

[102] J. G. Rarity, P. R. Tapster, and R Loudon. "Non-classical interference between independent sources." In: *J. Opt. B: Quantum Semiclass. Opt.* 7 (2005), p. 6. DOI: 10.1088/1464-4266/7/7/007. arXiv: 9702032 [quant-ph].

[103] Z. Y. Ou et al. "Fourth-order interference technique for determing the coherence time of a light beam." In: *J. Opt. Soc. Am. B* 6.1 (1989), pp. 100–103. DOI: 10.1364/JOSAB.6.000100.

[104] J. Bylander, I. Robert-Philip, and I. Abram. "Interference and correlation of two independent photons." In: *The European Physical Journal D* 22.2 (2003), pp. 295–301. DOI: 10.1140/epjd/e2002-00236-6.

[105] R. B. Patel et al. "Two-photon interference of the emission from electrically tunable remote quantum dots." In: *Nature Photonics* 4.9 (2010), pp. 632–635. DOI: 10.1038/nphoton.2010.161. arXiv: 0911.3997.

[106] C. Santori et al. "Indistinguishable photons from a single-photon device." In: *Nature* 419.6907 (2002), pp. 594–597. DOI: 10.1109/QELS.2003.1276041.

[107] T. Legero et al. "Quantum beat of two single photons." In: *Physical Review Letters* 93.7 (2004), pp. 1–4. DOI: 10.1103/PhysRevLett.93.070503. arXiv: 0406096 [quant-ph].

[108] R. Lettow et al. "Quantum interference of tunably indistinguishable photons from remote organic molecules." In: *Physical Review Letters* 104.12 (2010), pp. 26–29. DOI: 10.1103/PhysRevLett.104.123605. arXiv: 0911.3031.

[109] A. Sipahigil et al. "Quantum interference of single photons from remote nitrogen-vacancy centers in diamond." In: *Physical Review Letters* 108.14 (2012), pp. 1–5. DOI: 10.1103/PhysRevLett.108.143601. arXiv: 1112.3975.

[110] H. Bernien et al. "Two-photon quantum interference from separate nitrogen vacancy centers in diamond." In: *Physical review letters* 108.4 (2012), p. 043604. DOI: 10.1103/PhysRevLett.108.043604.

[111] A. Sipahigil et al. "Indistinguishable photons from separated silicon-vacancy centers in diamond." In: *Physical Review Letters* 113.11 (2014), pp. 1–5. DOI: 10.1103/PhysRevLett.113.113602. arXiv: 1406.4268.

[112] C. I. Osorio, N. Sangouard, and R. T. Thew. "On the purity and indistinguishability of down-converted photons." In: *Journal of Physics B: Atomic, Molecular and Optical Physics* 46.5 (2013), p. 055501. DOI: 10.1088/0953-4075/46/5/055501. arXiv: 1211.0120.

[113] U. Leonhardt. *Measuring the Quantum State of Light*. Cambridge University Press, 1997, p. 192.

[114] M. Nielsen and I. Chuang. *Quantum Computation and Qunatum Information*. Cambridge University Press, 2000, pp. 409–416.

[115] A. Aspect, J. Dalibard, and G. Roger. "Experimental test of Bell's inequalities using time- varying analyzers." In: *Physical Review Letters* 49.25 (1982), pp. 1804–1807. DOI: 10.1103/PhysRevLett.49.1804.

[116] P. W. Shor. "Polynomial-Time Algorithms for Prime Factorization and Discrete Logarithms on a Quantum Computer." In: *SIAM journal on computing* 26.5 (1997), pp. 1484–1509.

[117] P. Rebentrost, M. Mohseni, and S. Lloyd. "Quantum support vector machine for big data classification." In: *Physical Review Letters* 113.3 (2014), pp. 1–5. DOI: 10.1103/PhysRevLett.113.130503. arXiv: 1307.0471.

[118] V. Giovannetti, S. Lloyd, and L. Maccone. "Quantum Metrology." In: *Physical Review Letters* 96.1 (2006), p. 010401. DOI: 10.1103/PhysRevLett.96.010401.

[119] M. B. Plenio and S. Virmani. "An introduction to entanglement measures." In: *Quant. Inf. Comput.* 7.1,2 (2005), pp. 1–51. DOI: 10.1007/978-3-319-04063-9_8. arXiv: 0504163 [quant-ph].

[120] J. Audretsch. *Entangled Systems: New Directions in Quantum Physics*. Wiley, 2007, p. 357.

[121] S. Popescu and D. Rohrlich. "Thermodynamics and the measure of entanglement." In: *Physical Review A* 56.5 (1997), pp. 3319–3321. DOI: 10.1103/PhysRevA.56.R3319. arXiv: 9610044 [quant-ph].

[122] C. H. Bennett et al. "Mixed-state entanglement and quantum error correction." In: *Physical Review A (Atomic, Molecular, and Optical Physics)* 54.5 (1996), p. 3824. DOI: 10.1103/PhysRevA.54.3824. arXiv: 9604024 [quant-ph].

[123] W. K. Wootters. "Entanglement of Formation of an Arbitrary State of Two Qubits." In: *Physical Review Letters* 80.10 (1998), pp. 2245–2248. DOI: 10.1103/PhysRevLett.80.2245.

[124] R. C. Pooser and B. Lawrie. "Plasmonic Trace Sensing below the Photon Shot Noise Limit." In: *ACS Photonics* 3.1 (2016), pp. 8–13. DOI: 10.1021/acsphotonics.5b00501.

[125] F. Verstraete, M. M. Wolf, and J. I. Cirac. "Quantum computation, quantum state engineering, and quantum phase transitions driven by dissipation." In: *Nature Physics* 5.1 (2009), p. 7. DOI: 10.1038/nphys1342. arXiv: 0803.1447.

[126] D. Martín-Cano et al. "Dissipation-driven generation of two-qubit entanglement mediated by plasmonic waveguides." In: *Physical Review B - Condensed Matter and Materials Physics* 84.23 (2011), pp. 1–12. DOI: 10.1103/PhysRevB.84.235306. arXiv: 1112.0144.

[127] S. Fasel et al. "Energy-time entanglement preservation in plasmon-assisted light transmission." In: *Physical Review Letters* 94 (2005). DOI: 10.1103/PhysRevLett.94.110501. arXiv: 0410064 [quant-ph].

[128] S. Fasel et al. "Quantum superposition and entanglement of mesoscopic plasmons." In: *New Journal of Physics* 8 (2006). DOI: 10.1088/1367-2630/8/1/013. arXiv: 0512022 [quant-ph].

[129] G. Fujii et al. "Preservation of photon indistinguishability after transmission through surface-plasmon-polariton waveguide." In: *Optics ...* 37.9 (2012), pp. 1535–1537.

[130] G. Di Martino et al. "Quantum statistics of surface plasmon polaritons in metallic strip waveguides." In: *Nano Letters* 12 (2012), pp. 2504–2508.

[131] A. Huck et al. "Demonstration of quadrature-squeezed surface plasmons in a gold waveguide." In: *Physical Review Letters* 102.24 (2009), p. 246802. DOI: 10.1103/PhysRevLett.102.246802. arXiv: 0901.3969.

[132] B. J. Lawrie, P. G. Evans, and R. C. Pooser. "Extraordinary optical transmission of multimode quantum correlations via localized surface plasmons." In: *Physical Review Letters* 110 (2013). DOI: 10.1103/PhysRevLett.110.156802. arXiv: 1209.3754.

[133] W. Fan, B. J. Lawrie, and R. C. Pooser. "Quantum plasmonic sensing." In: *Physical Review A - Atomic, Molecular, and Optical Physics* 92.5 (2015), pp. 1–5. DOI: 10.1103/PhysRevA.92.053812.

[134] B. Vest et al. "Coalescence and anti-coalescence of surface plasmons on a lossy beamsplitter." In: *Arxiv* (2016), pp. 1–5. arXiv: 1610.07479.

[135] S. I. Bozhevolnyi and J. Khurgin. "Fundamental limitations in spontaneous emission rate of single-photon sources." In: *Optica* 3.12 (2016). DOI: 10.1364/OPTICA.3.001418.

[136] a. V. Akimov et al. "Generation of single optical plasmons in metallic nanowires coupled to quantum dots." In: *Nature* 450.7168 (2007), pp. 402–6. DOI: 10.1038/nature06230.

[137] N. P. de Leon et al. "Tailoring Light-Matter Interaction with a Nanoscale Plasmon Resonator." In: *Physical Review Letters* 108.22 (2012), p. 226803. DOI: 10.1103/PhysRevLett.108.226803.

[138] D. E. Chang et al. "A single-photon transistor using nanoscale surface plasmons." In: *Nature Physics* 3.11 (2007), pp. 807–812. DOI: 10.1038/nphys708.

[139] R. Chikkaraddy et al. "Single-molecule strong coupling at room temperature in plasmonic nanocavities." In: *Nature* 535.7610 (2016), pp. 127–130. DOI: 10.1038/nature17974. arXiv: NIHMS150003.

[140] T. Hümmer et al. "Weak and strong coupling regimes in plasmonic QED." In: *Physical Review B - Condensed Matter and Materials Physics* 87.11 (2013), pp. 1–16. DOI: 10.1103/PhysRevB.87.115419. arXiv: 1209.1724v2.

[141] G.-Y. Chen et al. "Surface plasmons in a metal nanowire coupled to colloidal quantum dots: Scattering properties and quantum entanglement." In: *Physical Review B* 84.4 (2011), p. 045310. DOI: 10.1103/PhysRevB.84.045310.

[142] G. M. Akselrod et al. "Probing the mechanisms of large Purcell enhancement in plasmonic nanoantennas." In: *Nature Photonics* 8.11 (2014), pp. 835–840. DOI: 10.1038/nphoton.2014.228.

[143] A. L. Falk et al. "Near-field electrical detection of optical plasmons and single-plasmon sources." In: *Nature Physics* 5.7 (2009), pp. 475–479. DOI: 10.1038/nphys1284.

[144] R. W. Heeres et al. "On-chip single plasmon detection." In: *Nano letters* 10.2 (2010), pp. 661–4. DOI: 10.1021/nl903761t.

[145] B. Calkins et al. "High quantum-efficiency photon-number-resolving detector for photonic on-chip information processing." In: *Optics Express* 21.19 (2013), pp. 22657–22670. DOI: 10.1364/OE.21.022657. arXiv: 1305.6627.

[146] J. N. Anker et al. "Biosensing with plasmonic nanosensors." In: *Nature materials* 7.6 (2008), pp. 442–453. DOI: 10.1038/nmat2162.

[147] V Giovannetti, S Lloyd, and L Maccone. "Advances in quantum metrology." In: *Nature Photonics* 5.4 (2011), pp. 222–229. DOI: 10.1038/nphoton.2011.35. arXiv: arXiv:1102.2318v1.

[148] K. C. Neuman et al. "Characterization of photodamage to Escherichia coli in optical traps." In: *Biophysical journal* 77.5 (1999), pp. 2856–63. DOI: 10.1016/S0006-3495(99)77117-1.

[149] M. Caldarola et al. "Non-plasmonic nanoantennas for surface enhanced spectroscopies with ultra-low heat conversion." In: *Nature communications* 6 (2015), p. 7915. DOI: 10.1038/ncomms8915.

[150] K. Banaszek, R. Demkowicz-Dobrzanski, and I. A. Walmsley. "Quantum states made to measure." In: *Nature Photonics* 3.12 (2009), pp. 673–676. DOI: 10.1038/nphoton.2009.223. arXiv: 0912.4092.

[151] S. Y. Wu et al. "Highly sensitive differential phase-sensitive surface plasmon resonance biosensor based on the Mach–Zehnder configuration." In: *Optics Letters* 29.20 (2004), p. 2378. DOI: 10.1364/OL.29.002378.

[152] M. Kashif et al. "Development of phase detection schemes based on surface plasmon resonance using interferometry." In: *Sensors (Basel, Switzerland)* 14.9 (2014), pp. 15914–38. DOI: 10.3390/s140915914.

[153] A. Crespi et al. "Measuring protein concentration with entangled photons." In: *Applied Physics Letters* 100 (2012), pp. 1–7. arXiv: arXiv:1109.3128v1.

[154] R. Demkowicz-Dobrzański, M. Jarzyna, and J. Kołodyński. "Quantum Limits in Optical Interferometry." In: *Progress in Optics* 60 (2015), pp. 345–435. DOI: 10.1016/bs.po.2015.02.003. arXiv: 1405.7703.

[155] K. J. Resch et al. "Time-reversal and super-resolving phase measurements." In: *Physical Review Letters* 98.22 (2007), pp. 2–5. DOI: 10.1103/PhysRevLett.98.223601. arXiv: 0511214 [quant-ph].

[156] O. Kwon, Y. S. Ra, and Y. H. Kim. "Observing photonic de Broglie waves without the maximally-path-entangled $|N,0\rangle+|0,N\rangle$ state." In: *Physical Review A - Atomic, Molecular, and Optical Physics* 81.6 (2010), pp. 1–8. DOI: 10.1103/PhysRevA.81.063801. arXiv: 0910.5797.

[157] X. Guo, Y. Ying, and L. Tong. "Photonic nanowires: From subwavelength waveguides to optical sensors." In: *Accounts of Chemical Research* 47.2 (2014), pp. 656–666. DOI: 10.1021/ar400232h.

[158] L. Tong and E. Mazur. "Single-mode guiding properties of subwavelength-diameter silica and silicon wire waveguides." In: *Optics Express* 12.6 (2004), pp. 2905–2912.

[159] M Sumetsky. "How thin can a microfiber be and still guide light?" In: *Optics letters* 31.7 (2006), pp. 870–872. DOI: 10.1364/OL.31.003577.

[160] A. D. Rakić et al. "Optical properties of metallic films for vertical-cavity optoelectronic devices." In: *Applied Optics Optics* 37.22 (1998), pp. 5271–5283. DOI: 10.1364/AO.37.005271.

[161] S. I. Bozhevolnyi. *Plasmonic nanoguides and circuits*. Pan Stanford Publishing, 2009, p. 441.

[162] D. F. P. Pile et al. "Theoretical and experimental investigation of strongly localized plasmons on triangular metal wedges for subwavelength waveguiding." In: *Applied Physics Letters* 87.6 (2005), pp. 1–4. DOI: 10.1063/1.1991990.

[163] M. W. Mitchell, J. S. Lundeen, and A. M. Steinberg. "Super-resolving phase measurements with a multiphoton entangled state." In: *Nature* 429.May (2004), p. 161. DOI: 10.1038/nature02493. arXiv: 0312186 [quant-ph].

[164] V. Giovannetti, S. Lloyd, and L. Maccone. "Quantum-enhanced measurements: beating the standard quantum limit." In: *Science* 306.5700 (2004), pp. 1330–6. DOI: 10.1126/science.1104149. arXiv: 0412078 [quant-ph].

[165] D. Girolami et al. "Quantum discord determines the interferometric power of quantum states." In: *Physical Review Letters* 112.21 (2014), pp. 1–5. DOI: 10.1103/PhysRevLett.112.210401. arXiv: 1309.1472.

[166] K. Jiang et al. "Strategies for choosing path-entangled number states for optimal robust quantum-optical metrology in the presence of loss." In: *Physical Review A* 86.1 (2012), p. 013826. DOI: 10.1103/PhysRevA.86.013826.

[167] S. D. Huver, C. F. Wildfeuer, and J. P. Dowling. "Entangled Fock states for robust quantum optical metrology, imaging, and sensing." In: *Physical Review A* 78.6 (2008), p. 063828. DOI: 10.1103/PhysRevA.78.063828.

[168] R. Demkowicz-Dobrzanski et al. "Quantum phase estimation with lossy interferometers." In: *Physical Review A - Atomic, Molecular, and Optical Physics* 80.1 (2009), pp. 1–10. DOI: 10.1103/PhysRevA.80.013825. arXiv: 0904.0456.

[169] U. Dorner et al. "Optimal quantum phase estimation." In: *Physical Review Letters* 102.4 (2009), pp. 1–4. DOI: 10.1103/PhysRevLett.102.040403. arXiv: 0807.3659.

[170] J. J. Cooper and J. A. Dunningham. "Towards improved interferometric sensitivities in the presence of loss." In: *New Journal of Physics* 13 (2011). DOI: 10.1088/1367-2630/13/11/115003.

[171] I. Afek, O. Ambar, and Y. Silberberg. "High-NOON states by mixing quantum and classical light." In: *Science (New York, N.Y.)* 328.5980 (2010), pp. 879–81. DOI: 10.1126/science.1188172.

[172] J. C. F. Matthews et al. "Heralding two-photon and four-photon path entanglement on a chip." In: *Physical Review Letters* 107.16 (2011), pp. 1–5. DOI: 10.1103/PhysRevLett.107.163602. arXiv: 1005.5119.

[173] J. L. O'Brien, A. Furusawa, and J. Vučković. "Photonic quantum technologies." In: *Nature Photonics* 3.12 (2010), pp. 687–695. DOI: 10.1038/nphoton.2009.229. arXiv: 1003.3928.

[174] M. Piliarik and J. í. Homola. "Surface plasmon resonance (SPR) sensors: approaching their limits?" In: *Opt. Express* 17.19 (2009), pp. 16505–16517. DOI: 10.1364/OE.17.016505.

[175] M. D. Lang and C. M. Caves. "Optimal quantum-enhanced interferometry using a laser power source." In: *Physical Review Letters* 111.17 (2013), pp. 1–5. DOI: 10.1103/PhysRevLett.111.173601. arXiv: 1306.2677.

[176] LIGO. "Enhancing the sensitivity of the LIGO gravitational wave detector by using squeezed states of light." In: *Nature Photonics* 7.8 (2013), pp. 613–619. DOI: 10.1038/nphoton.2013.177. arXiv: arXiv:1310.0383v1.

[177] T. Ono and H. F. Hofmann. "Effects of photon losses on phase estimation near the Heisenberg limit using coherent light and squeezed vacuum." In: *Physical Review A - Atomic, Molecular, and Optical Physics* 81.3 (2010), pp. 2–7. DOI: 10.1103/PhysRevA.81.033819. arXiv: 0910.3727.

[178] R. Demkowicz-Dobrzański, J. Kołodyński, and M. Guţă. "The elusive Heisenberg limit in quantum-enhanced metrology." In: *Nature Communications* 3.2006 (2012), p. 1063. DOI: 10.1038/ncomms2067. arXiv: 1201.3940.

[179] F. Dieleman. "Quantum Interferences of single Surface Plasmons." PhD thesis. Imperial College London, 2013, p. 70.

[180] T. G. Habteyes et al. "Plasmon Damping and Molecular Linker as a Nondamping Alternative." In: 6 (2012), pp. 5702–5709.

[181] R. Zia, M. D. Selker, and M. L. Brongersma. "Leaky and bound modes of surface plasmon waveguides." In: *Physical Review B - Condensed Matter and Materials Physics* 71.16 (2005), pp. 1–9. DOI: 10.1103/PhysRevB.71.165431.

[182] R. Zia, A. Chandran, and M. L. Brongersma. "Dielectric waveguide model for guided surface polaritons." In: *Optics letters* 30.12 (2005), pp. 1473–1475. DOI: 10.1364/OL.30.001473.

[183] R. L. Olmon et al. "Optical dielectric function of gold." In: *Physical Review B* 86.23 (2012), p. 235147. DOI: 10.1103/PhysRevB.86.235147.

[184] Y. Vlasov and S. McNab. "Losses in single-mode silicon-on-insulator strip waveguides and bends." In: *Optics express* 12.8 (2004), pp. 1622–1631. DOI: 10.1364/OPEX.12.001622.

[185] B. Lamprecht et al. "Surface plasmon propagation in microscale metal stripes." In: *Applied Physics Letters* 79.1 (2001), pp. 51–53. DOI: 10.1063/1.1380236.

[186] H. Raether. *Surface Plasmons*. 1986.

[187] H. Ditlbacher et al. "Two-dimensional optics with surface plasmon polaritons." In: *Applied Physics Letters* 81.10 (2002), pp. 1762–1764. DOI: 10.1063/1.1506018.

[188] A. Drezet et al. "Surface plasmon polariton Mach-Zehnder interferometer and oscillation fringes." In: *Plasmonics* 1.2-4 (2006), pp. 141–145. DOI: 10.1007/s11468-006-9016-5. arXiv: arXiv:1002.0746v1.

[189] A Drezet et al. "Plasmonic crystal demultiplexer and multiports." In: *Nano Letters* 7.6 (2007), pp. 1697–1700. DOI: 10.1021/nl070682p. arXiv: arXiv:1002.0766v1.

[190] J.-C. Weeber et al. "Near-field characterization of Bragg mirrors engraved in surface plasmon waveguides." In: *Physical Review B* 70.23 (2004), p. 235406. DOI: 10.1103/PhysRevB.70.235406.

[191] M. U. Gonzalez et al. "Design, near-field characterization, and modeling of 45 surface-plasmon Bragg mirrors." In: *Physical Review B - Condensed Matter and Materials Physics* 73.15 (2006), pp. 19–21. DOI: 10.1103/PhysRevB.73.155416.

[192] M. U. González et al. "Analysis of the angular acceptance of surface plasmon Bragg mirrors." In: 32.18 (2007), pp. 2704–2706.

[193] S. Jetté-Charbonneau et al. "Demonstration of Bragg gratings based on long-ranging surface plasmon polariton waveguides." In: *Optics express* 13.12 (2005), pp. 4674–4682. DOI: 10.1364/OPEX.13.004674.

[194] J. C. Weeber et al. "Surface plasmon routing along right angle bent metal strips." In: *Applied Physics Letters* 87.22 (2005), pp. 1–3. DOI: 10.1063/1.2130393.

[195] N. Spagnolo et al. "Three-photon bosonic coalescence in an integrated tritter." In: *Nature communications* 4 (2013), p. 1606. DOI: 10.1038/ncomms2616.

[196] R. Loudon. "Single-mode quantum optics." In: *The Quantum Theory of Light*. 2000, pp. 180–232.

[197] V. Coello, T. Søndergaard, and S. I. Bozhevolnyi. "Modeling of a surface plasmon polariton interferometer." In: *Optics Communications* 240.4-6 (2004), pp. 345–350. DOI: 10.1016/j.optcom.2004.06.042.

[198] C. K. Hong and L. Mandel. "Experimental realization of a localized one-photon state." In: *Physical Review Letters* 56.1 (1986), pp. 58–60. DOI: 10.1103/PhysRevLett.56.58.

[199] Y. Jeronimo-Moreno and R. Jauregui. "Type I parametric down conversion of highly focused Gaussian beams in finite length crystals." In: *Journal of Optics* 16 (2014), p. 9. DOI: 10.1088/2040-8978/16/6/065201.

[200] *BiBO Crystals*.

[201] B. Saleh and M. C. Teich. *Fundamentals of Photonics*. Ed. by Wiley-Blackwell. 2nd. 2007, p. 1200.

[202] *Reflective Collimators, Protected Silver Coating*.

[203] T. Goulette, C. Howard, and M. Davidson. *Infinity Optical Systems*.

[204] D. Sivia and J. Skilling. *Data Analysis: A Bayesian Tutorial*. 2nd. Oxford University Press, 2006, p. 272.

[205] Z. Mazzotta et al. "High-order dispersion effects in two-photon interference." In: *arXiv* 063842.November (2016), pp. 1–6. DOI: 10.1103/PhysRevA.94.063842. arXiv: 1607.05854.

[206] M. Dheur et al. "Single-Plasmon Interferences." In: *Science Advances (New York, N.Y.)* Accepted.March (2016), To be published. DOI: 10.1126/sciadv.1501574.

[207] T. Roger et al. "Coherent perfect absorption in deeply subwavelength films in the single-photon regime." In: *Nature Communications* 6.May (2015), p. 7031. DOI: 10.1038/ncomms8031. arXiv: 1601.02821.

[208] S. Zanotto and A. Melloni. "Design of a hybrid silicon-plasmonic co-propagating coupler operating close to coherent perfect absorption." In: *Journal of Applied Physics* 119.16 (2016). DOI: 10.1063/1.4947279.

[209] M. R. Ray and S. J. Van Enk. "Verifying entanglement in the Hong-Ou-Mandel dip." In: *Physical Review A - Atomic, Molecular, and Optical Physics* 83.4 (2011), pp. 1–5. DOI: 10.1103/PhysRevA.83.042318. arXiv: 1101.0846.

[210] R. Simon and N. Mukunda. "Universal SU(2) gadget for polarization optics." In: *Physics Letters A* 138.9 (1989), pp. 474–480. DOI: 10.1016/0375-9601(89)90748-2.

[211] U. Schilling, J. Von Zanthier, and G. S. Agarwal. "Measuring arbitrary-order coherences: Tomography of single-mode multiphoton polarization-entangled states." In: *Physical Review A - Atomic, Molecular, and Optical Physics* 81.1 (2010), pp. 1–5. DOI: 10.1103/PhysRevA.81.013826. arXiv: 0908.1662.

[212] G. S. Agarwal and S Chaturvedi. "Scheme to measure quantum Stokes parameters and their fluctuations and correlations." In: *Journal of Modern Optics* 50.5 (2003), pp. 711–716. DOI: Doi10.1080/09500340210150497. arXiv: 0203050 [quant-ph].

[213] B. Schaefer et al. "Measuring the Stokes polarization parameters." In: *American Journal of Physics* 75.2 (2007), p. 163. DOI: 10.1119/1.2386162.

[214] O. Kwon, Y.-S. Ra, and Y.-H. Kim. "Coherence properties of spontaneous parametric down-conversion pumped by a multimode cw diode laser." In: *Optics express* 17.15 (2009), pp. 13059–13069. DOI: 10.1364/OE.17.013059.

[215] O. Kwon et al. "Time-bin entangled photon pairs from spontaneous parametric down-conversion pumped by a cw multimode diode laser." In: *Optics express* 21.21 (2013), pp. 25492–500. DOI: 10.1364/OE.21.025492.

[216] K. Edamatsu, R. Shimizu, and T. Itoh. "Measurement of the photonic de broglie wavelength of entangled photon pairs generated by spontaneous parametric down-conversion." In: *Physical review letters* 89.21 (2002), p. 213601. DOI: 10.1103/PhysRevLett.89.213601. arXiv: 0109005 [quant-ph].

[217] R. B. A. Adamson et al. "Multiparticle state tomography: Hidden differences." In: *Physical Review Letters* 98.4 (2007), pp. 1–4. DOI: 10.1103/PhysRevLett.98.043601. arXiv: 0601134 [quant-ph].

[218] R. B. A. Adamson et al. "Detecting hidden differences via permutation symmetries." In: *Physical Review A - Atomic, Molecular, and Optical Physics* 78.3 (2008), pp. 1–10. DOI: 10.1103/PhysRevA.78.033832. arXiv: 0612081 [quant-ph].



Thank you for your order!

Dear Mr. Frederik Dieleman,

Thank you for placing your order through Copyright Clearance Center's RightsLink® service.

Order Summary

Order Date:	Mar 2, 2017
Order Number:	4060920263161
Publication:	Surface Science Reports
Title:	A microscopic view of the electromagnetic properties of sub λ metallic surfaces
Type of Use:	reuse in a thesis/dissertation
Order Total:	0.00 GBP

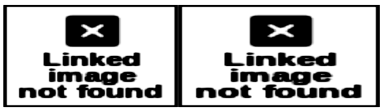
View or print complete of your order and the publisher's terms and conditions.

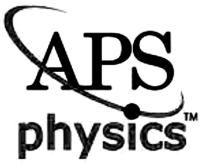
Sincerely,

Copyright Clearance Center

How was your experience? Fill out this to let us know.

Tel: +1 855 239 3415 / +1 978 646 2777
customercare@copyright.com
https://myaccount.copyright.com





Thank you for your order!

Dear Mr. Frederik Dieleman,

Thank you for placing your order through Copyright Clearance Center's RightsLink® service.

Order Summary

Order Date:	Mar 2, 2017
Order Number:	4060920012694
Publication:	Physical Review B
Title:	Physical origin of photonic energy gaps in the propagation of surface plasmons on gratings
Type of Use:	Thesis/Dissertation
Order Total:	0.00 GBP

View or print complete of your order and the publisher's terms and conditions.

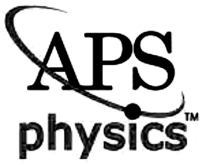
Sincerely,

Copyright Clearance Center

How was your experience? Fill out this to let us know.

Tel: +1 855 239 3415 / +1 978 646 2777
customercare@copyright.com
https://myaccount.copyright.com





Thank you for your order!

Dear Mr. Frederik Dieleman,

Thank you for placing your order through Copyright Clearance Center's RightsLink® service.

Order Summary

Order Date:	Mar 2, 2017
Order Number:	4060920452166
Publication:	Physical Review B
Title:	Near field observation of surface plasmon polariton propagation on thin metal stripes
Type of Use:	Thesis/Dissertation
Order Total:	0.00 GBP

View or print complete of your order and the publisher's terms and conditions.

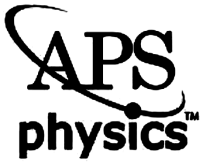
Sincerely,

Copyright Clearance Center

How was your experience? Fill out this to let us know.

Tel: +1 855 239 3415 / +1 978 646 2777
customercare@copyright.com
https://myaccount.copyright.com





Thank you for your order!

Dear Mr. Frederik Dieleman,

Thank you for placing your order through Copyright Clearance Center's RightsLink® service.

Order Summary

Order Date:	Mar 2, 2017
Order Number:	4060920347589
Publication:	Physical Review B
Title:	Efficiency of local surface plasmon polariton excitation on ridges
Type of Use:	Thesis/Dissertation
Order Total:	0.00 GBP

View or print complete of your order and the publisher's terms and conditions.

Sincerely,

Copyright Clearance Center

How was your experience? Fill out this to let us know.

Tel: +1 855 239 3415 / +1 978 646 2777
customercare@copyright.com
https://myaccount.copyright.com





Thank you for your order!

Dear Mr. Frederik Dieleman,

Thank you for placing your order through Copyright Clearance Center's RightsLink® service.

Order Summary

Order Date:	Mar 1, 2017
Order Number:	4060430144765
Publication:	Nature Physics
Title:	A single photon transistor using nanoscale surface plasmons
Type of Use:	reuse in a dissertation / thesis
Order Total:	0.00 GBP

View or print complete of your order and the publisher's terms and conditions.

Sincerely,

Copyright Clearance Center

How was your experience? Fill out this to let us know.

Tel: +1 855 239 3415 / +1 978 646 2777
customercare@copyright.com
https://myaccount.copyright.com



nature publishing group

Thank you for your order!

Dear Mr. Frederik Dieleman,

Thank you for placing your order through Copyright Clearance Center's RightsLink® service.

Order Summary

Order Date:	Mar 1, 2017
Order Number:	4060430712451
Publication:	Nature Materials
Title:	Local detection of electromagnetic energy transport below the diffraction limit in metal nanoparticle plasmon waveguides
Type of Use:	reuse in a dissertation / thesis
Order Total:	0.00 USD

View or print complete of your order and the publisher's terms and conditions.

Sincerely,

Copyright Clearance Center

How was your experience? Fill out this to let us know.

Tel: +1 855 239 3415 / +1 978 646 2777
customercare@copyright.com
https://myaccount.copyright.com

Copyright Clearance Center RightsLink

nature publishing group

Thank you for your order!

Dear Mr. Frederik Dieleman,

Thank you for placing your order through Copyright Clearance Center's RightsLink® service.

Order Summary

Order Date:	Mar 1, 2017
Order Number:	4060430812034
Publication:	Nature
Title:	Channel plasmon subwavelength waveguide components including interferometers and ring resonators
Type of Use:	reuse in a dissertation / thesis
Order Total:	0.00 GBP

View or print complete of your order and the publisher's terms and conditions.

Sincerely,

Copyright Clearance Center

How was your experience? Fill out this to let us know.

Tel: +1 855 239 3415 / +1 978 646 2777
customercare@copyright.com
https://myaccount.copyright.com

Copyright Clearance Center RightsLink



Thank you for your order!

Dear Mr. Frederik Dieleman,

Thank you for placing your order through Copyright Clearance Center's RightsLink® service.

Order Summary

Order Date:	Mar 1, 2017
Order Number:	4060430998167
Publication:	Nature Physics
Title:	Near field electrical detection of optical plasmons and single plasmon sources
Type of Use:	reuse in a dissertation / thesis
Order Total:	0.00 GBP

View or print complete of your order and the publisher's terms and conditions.

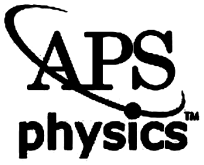
Sincerely,

Copyright Clearance Center

How was your experience? Fill out this to let us know.

Tel: +1 855 239 3415 / +1 978 646 2777
customercare@copyright.com
https://myaccount.copyright.com





Thank you for your order!

Dear Mr. Frederik Dieleman,

Thank you for placing your order through Copyright Clearance Center's RightsLink® service.

Order Summary

Order Date:	Mar 1, 2017
Order Number:	4060431438698
Publication:	Physical Review Applied
Title:	Observation of Quantum Interference in the Plasmonic Hong Ou Mandel Effect
Type of Use:	Thesis/Dissertation
Order Total:	0.00 GBP

View or print complete details of your order and the publisher's terms and conditions.

Sincerely,

Copyright Clearance Center

How was your experience? Fill out this to let us know.

Tel: +1 855 239 3415 / +1 978 646 2777
customercare@copyright.com
https://myaccount.copyright.com





Thank you for your order!

Dear Mr. Frederik Dieleman,

Thank you for placing your order through Copyright Clearance Center's RightsLink® service.

Order Summary

Order Date:	Mar 1, 2017
Order Number:	4060430498933
Publication:	Nature
Title:	Single molecule strong coupling at room temperature in plasmonic nanocavities
Type of Use:	reuse in a dissertation / thesis
Order Total:	0.00 USD

View or print complete details of your order and the publisher's terms and conditions.

Sincerely,

Copyright Clearance Center

How was your experience? Fill out this to let us know.

Tel: +1 855 239 3415 / +1 978 646 2777
customercare@copyright.com
https://myaccount.copyright.com

